NATIONAL TECHNICAL UNIVERSITY OF ATHENS

SCHOOL OF NAVAL ARCHITECTURE AND MARINE ENGINEERING

LABORATORY OF SHIP AND MARINE HYDRODYNAMICS

Numerical Analysis of the effects of Free Surface on a Fully Passive Energy Harvesting Flapping Foil device.

Diploma Thesis submitted by:

Nikolaos Petikidis

Thesis Supervisor: Assistant Professor G. Papadakis

Committee Member: Professor K. Belibassakis

Committee Member: Assistant Professor K. Anyfantis

February 28, 2023

This page is intentionally left blank.

Abstract

The aim of this thesis is to investigate the effects of the free surface on a fully passive flapping foil device. The in-house Computational Fluid Dynamics RANS solver MaPFlow is used, strongly coupled with a Rigid Body Dynamics solver. The problem is modeled in two dimensions, and the incompressible Navier-Stokes are solved, while the Volume of Fluid method is used to simulate the two phases, water and air. The structural parameters selected are held constant for all the cases. The influence a calm free surface is mainly examined, but initial research of the influence of waves also takes place.

Firstly, the influence of varying the Submergence depth on the performance of the flapping foil for an initially calm free surface is examined. It is seen that for very low Submergence depths performance decreases greatly. However for intermediate depths performance is very good, even greater than the case where the flapping foil operates in infinite fluid. Increasing the submergence depth further, performance drops again slightly, and for very large depths, the case of infinite fluid is approached. These tests are also repeated for multiple Froude numbers. Although the Froude number affects the performance of the fully passive flapping foil, the same pattern takes place irrespective of it. Thus, there exists an optimal submergence depth where the flapping foil's operation is aided by the free surface. Finally, a few cases where regular waves propagate on the free surface are examined. It is seen that waves with frequency close to that of the flapping foil can aid its performance while high frequency waves do not.

Acknowledgements

The completion of this thesis marks the end of my studies in the School of Naval Architecture and Marine Engineering and this challenging thesis was a priceless dive into the field of Fluid Dynamics and an introduction to research work in general.

First and foremost, I would like to thank my supervisor, Professor Mr. George Papadakis, who gave me an interesting research topic and the opportunity to work on it close to his office. Him, and PhD candidate Dimitris Ntouras provided invaluable assistance and contributed greatly to the realization of this dissertation. Their door was always open for questions as they imparted invaluable knowledge to me, always in a friendly manner.

I would also like to like to thank all my friends and especially Christoforos and Dimitris who study Mechanical Engineering, and with whom we had many profound conversations on topics on our fields. I am also grateful for my friendship with Vaso, whom I met in this school, as we worked together countless hours through all the courses, imparting knowledge on one another and pushing each other through to the end. Finally, I would like to deeply thank my family for all their generous support, their advice and their understanding during all these years.

Contents

1. Introduction to Flapping Foils

The transition to sustainable forms of energy requires the utilization of a wide range of available energy sources. For the transition to happen fast and smoothly, these devices have to be low-cost, simple to build and deliver large amounts of power with efficiency, consistency and predictability. The widely implemented wind and solar energy harvesting devices have managed to reduce their cost significantly. However, they face a major drawback, as their power production is largely unpredictable. Hydroelectric stations on the other hand, don't face this problem, but the cost of building dams is large, and the disruption to the local environment is significant.

It has been proven by recent research that harvesting marine current energy with tidal turbines has great potential as a regular, predictable and clean energy source for power generation, with fewer harmful influences on the environment as opposed to other ways [1] [2]. The available power generation that is exploitable from tidal currents is estimated to be around 75 GW worldwide, 11 GW in Europe and 6 GW in the UK alone [3]. Especially in comparison with wind turbines, tidal turbines require negligible infrastructural investment, have diminished natural effects and sound issues. On the downside, their environment is a lot harsher which potentially means higher operational expenditure, due to corrosion and higher loads that blades are subjected to in the water, compared to air.

The most prominent and well-studied devices designed to captured tidal energy are horizontal axis turbines, vertical axis turbines and oscillating hydrofoils (Figure 1.1). The former two of these, horizontal and vertical axis turbines, are efficient mainly at their design point, where the flow is attached. Oscillating hydrofoils however, which mimic the swimming pattern of fish, utilize the flow separation, and use it in their advantage. The phenomenon of dynamic stalls occurs and makes them achieve large amounts of lift, despite the very large angles of attack, that can be quite larger than those produced for stationary wings in attached flow [4]. This also means that oscillating hydrofoils can harvest energy from a wider range of current velocities [5]. The device is also more robust, as centrifugal stresses are absent, and more environmentally friendly, as blade tip velocities are lower. It's rectangular sweeping makes it a good match for shallow and wide flows.

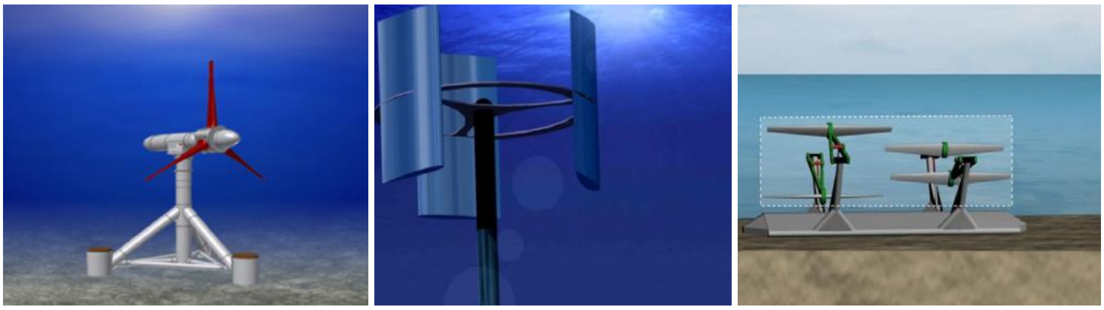

Figure 1.1 Types of Tidal Turbines a) horizontal axis turbine, b) vertical axis turbine, c) oscillating hydrofoils.

The technology for oscillating hydrofoils was inspired by fish locomotion. Evolution through hundreds of millions of years has enabled fishes to develop highly efficient mechanical systems. Fish transfer momentum to their surrounding water and vice versa through mechanisms such as drag, lift and acceleration reaction forces. Most fish generate thrust by creating a backward-moving propulsive wave through their body's movement, called undulatory movement, or by oscillating their body on its base without exhibiting a wave formation, called oscillatory movement [6]. An inverted von Karman wake is generated by the fish, having a jet-like structure, making apparent the momentum transfer from the fish to the water (Figure 1.2). The same motion, but with sufficiently high pitching amplitude can be used to capture energy from an incoming fluid flow. If the pitching amplitude is higher than a threshold value, for a given frequency and heave amplitude, called the feathering limit (Figure 1.3), the foil switches from the thrust production mode to the energy harvesting mode.

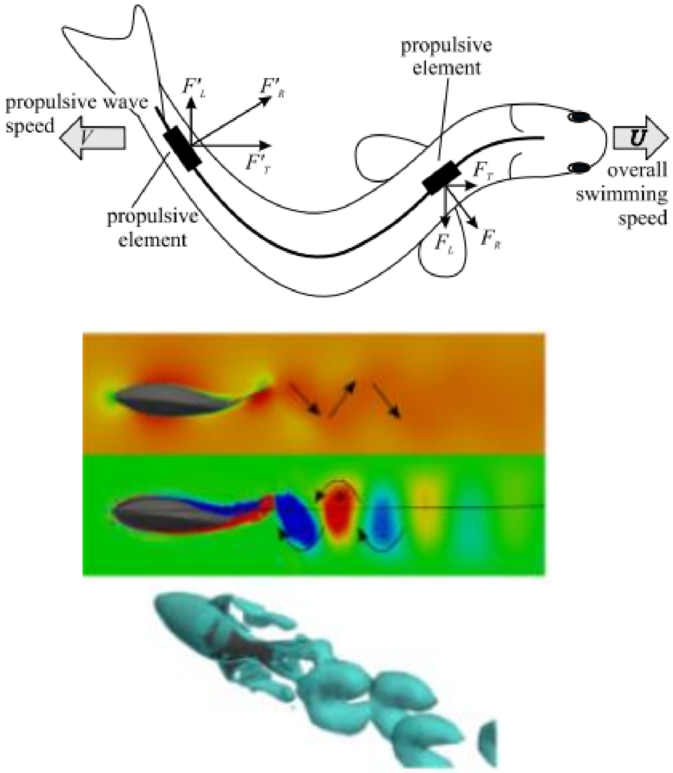

Figure 1.2 Visualization of a fish performing undulatory movement

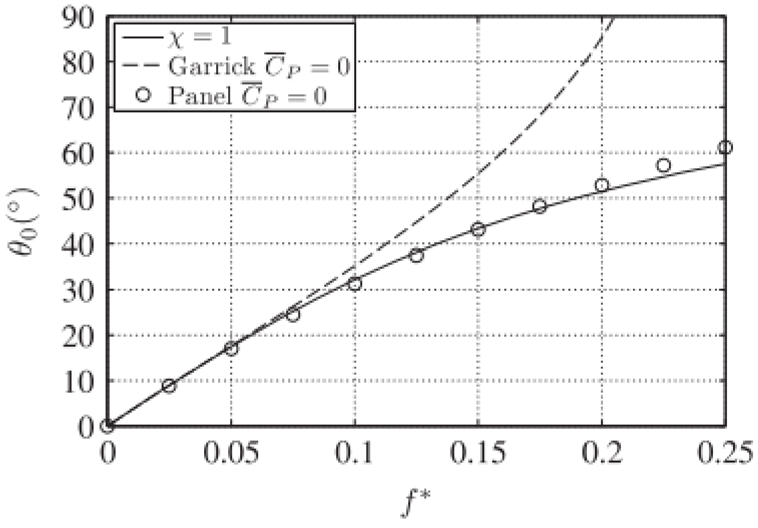

Figure 1.3 Estimations of pitch amplitude threshold (feathering limit) for energy harvest, for heave amplitude h = 1. Above the curve, energy is harvested, while below thrust is produced.*

It has been shown that oscillating hydrofoils, also called flapping foils, can either be used successfully for production of thrust or energy harvest. Many studies have been done, either experimental [7] [8] or numerical (a collection can be found here: [5]), showing the applicability of these devices and highlighting their advantages and disadvantages over conventional devices. Energy harvesting foils were first proposed by McKinney and DeLaurier in 1981 [9]. Their foil performed a sinusoidal motion in both the pitch and heave degrees of freedom, meaning that the motion was fully prescribed and enforced externally. The oscillatory motion of energy harvesting flapping foil is shown in Figure 1.6. This device can be simplified (Zhu et al [10]) by attaching the heave DOF to a spring and damper, and imposing the motion of the pitch DOF, creating the semi-passive flapping foil. The pitching motion creates a variable lift force that makes the foil oscillate in its heave DOF. Finally, both pitching and heaving DOF can be attached to springs and dampers, creating the fully passive flapping foil, which begins to oscillate without external forcing when it faces fluid flow.

This thesis is concerned only with the fully passive flapping foil operating in water under a free surface. Peng and Zhu [11] explored the modes that are achievable by different choices of the structural parameters. The main parameters that affect the mode are the pitching axis location (b) and the stiffness of the rotational spring (k_a). By different choice of these parameters (Figure 1.4) four different modes can be observed in Figure 1.5. The one that is suitable for energy harvest, as its oscillatory movement is periodic and with large amplitudes, is the second one (ii). Mode (i) is not useful as no motion means no energy production. Mode (iii) is erratic and characterized by low efficiency and power output. Finally in mode (iv) the foil is inverted, and the motion is completely erratic. The movement of a fully passive flapping foil, operating in mode (ii), per one tenth of a period is depicted in Figure 1.6.

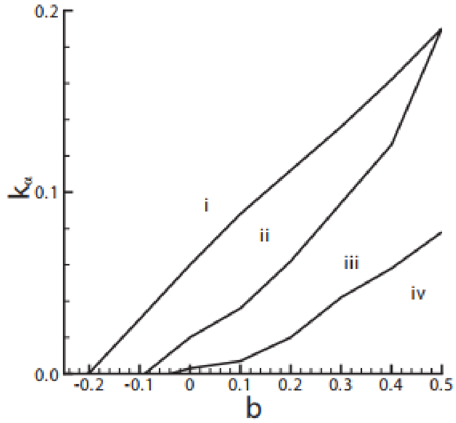

Figure 1.4 Mode types achieved by varying Pitch axis location (b) and rotational spring stiffness (k_α).

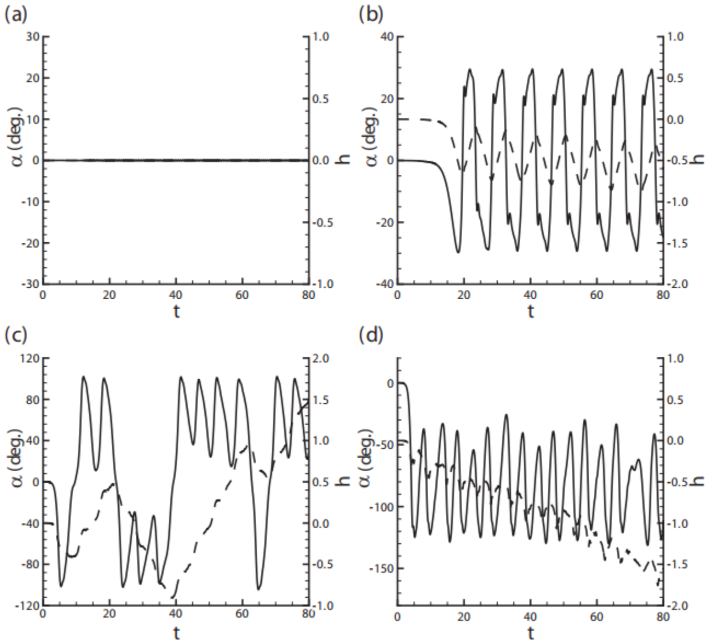

Figure 1.5 Heave position and pitch angel timeseries for the different modes.

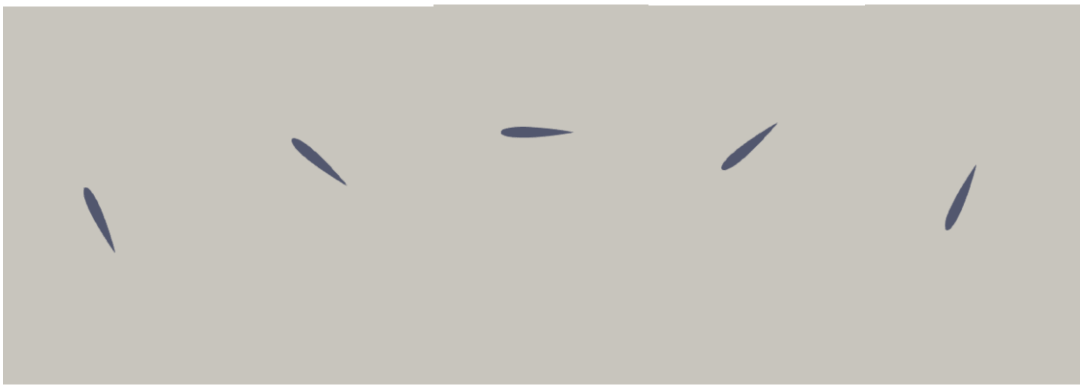

Figure 1.6 Motion Example of a fully passive energy harvesting flapping foil.

These fully passive flapping-foils are a viable alternative to the fully or semi constrained (active) flapping foils that require intricate mechanisms to enforce the movement. These extra mechanisms raise the risk of failure, the construction cost, and the cost of maintenance. They also have additional power losses. Most research in the past has shown that the fully passive foil exhibits a lower efficiency (around 30%) compared to the active ones (45%). Numerical experiments though, by Dumas et al. [12], aiming to optimize the device by exploring the available domain of the structural parameters showed that the passive foil can reach up to 53.8% efficiency while maintaining sufficient power output. This showed that passive foil can be as efficient as their active counterparts, while being much simpler. In addition, it was shown that good performance can be maintained for a wide range of parameters, which is necessary for a practical application.

While a plethora of research has been conducted for active energy harvesting flapping foils in general, not so much has been conducted for passive foils. The effects of proximity to the free surface, for instance, or the effects of waves, have not yet been explored. The application of these foils will probably be in shallow water, either in rivers or relatively close to shores as a tidal energy capturing device. This means that the submergence depth will be low, and the free surface will significantly affect their performance.

Effects of the calm free surface on active energy harvesting flapping foils has been evaluated by numerical tests for different Submergence depths and Froude numbers by [13] and [14]. In both of those papers, it was found that, in general, the effect of free surface is negative to the efficiency and power output of the device for most water depths, but there exists a submergence depth where performance is equal or even higher than that of the infinite flowfield case. As for fully passive foils, [15] did a numerical simulation for the free surface effect for a specific submergence depth, where it was found that for this particular depth the effect was negative.

With regards to the influence of a wavey free surface on flapping foils, [16] was the first to propose that a flapping foil on the bow of a ship could convert wave power into propulsive power and proved this case. The effect of regular waves on thrust producing flapping foils, both rigid and flexible, has also been studied by [17], where it was found that power output is significantly increased, especially when the frequency of the waves matches that of the foil and the phase difference is suitable. Efficiency was higher when a flexible foil was used, but was not affected that greatly, in general. [18] also studied thrust producing flapping foils in waves, for constant depth and wave heights using a boundary element method (BEM). It was found that increase in wave frequency, increased the power output but decreased the efficiency. It is distinctive that the amplitudes of the motion fluctuated periodically when the frequencies of the foil and waves did not match. When the frequencies did match there were no fluctuations, as the relative position of foil and wave remained constant throughout the periods, but the phase difference played a significant role.

As for energy harvesting flapping foils [19], a semi-active flapping foil operating in waves and currents, in a shear flow with variable bathymetry (simulating nearshore conditions) was studied using BEM analysis. For a specific moderate wave frequency, significant efficiency can be achieved both when the foil and wave frequency match or don’t, by operating at appropriate pitch angles. Peak efficiency was achieved, however, even for small pitching angles, when the foil matched the frequency of the waves or was double that, and the phase difference was suitable for each case.

This thesis is structured as follows: In chapter 2 the in-house Computational Fluid Dynamics solver MaPFlow, which was used here, is outlined briefly. In chapter 3, the Rigid Body Dynamics solver is explained along with the strong coupling method with the CFD solver. In chapter 4, the physical mechanism and dynamics equations of the energy harvesting, fully passive flapping foil is provided along with definition of efficiency and power and force coefficients used to evaluate its performance. Then, the meshing strategy of the numerical wave tank is described. In order to determine a numerical setup which gives quality results, but is not too computationally expensive, a mesh dependency and timestep dependency study takes place. Finally, to verify the numerical setup, an infinite flowfield case (no free surface effects) is contrasted to experimental results with the same structural parameters used. In chapter 5 the effects of the calm free surface on the performance of the flapping foil, for various Submergence Depths and Froude numbers are examined. In chapter 6, as a first step, the effects of regular waves of different frequencies and wavelengths are examined for a selected Submergence Depth and Froude number. The height of the wave remains fixed, and the frequency and wavelength parameters are explored. The potential impact of phase difference between waves and the foil’s motion is also explored.

2. MaPFlow

2.1 Governing Equations

In this section, the fundamental equations of conservation for an incompressible, isothermal viscous fluid are presented, along with their special formulation for capturing the free surface effects. These equations construct the core of the CFD, finite volume, solver MaPFlow, which is used for the simulations in the following chapter.

The conservation of mass equation in an incompressible fluid is:

$$\nabla \cdot \vec{u} = 0 \tag{2.1}$$

The conservation of momentum equation for an incompressible fluid is

$$\frac{\partial u}{\partial t} + \vec{u} \cdot \nabla\vec{u} = -\frac{\nabla p}{\rho} + \nabla\bar{\sigma} + \overrightarrow{F_B} \tag{2.2}$$

, where p is the pressure, $\bar{\sigma}$ is the stress tensor and $\overrightarrow{F_B}$ are the source terms and body forces. The conservation of energy is omitted in our approach since it is redundant in the incompressible isothermal fluid case.

In order to model the effects of the free surface and track down its locus, MaPFlow uses the Volume of Fluid method. An indicator function, the volume fraction, is defined for each cell as $a_l = (\rho_m - \rho_\alpha)/(\rho_w - \rho_\alpha)$, and used to distinguish between the two different fluids, air and water. ρ_α is the density of the air and ρ_w the density of the water. The properties of the mixture fluid ρ_m and μ_m, are described by the blending functions (2.3).

$$\begin{aligned} \rho_m &= a_l\rho_w + (1 - a_l)\rho_\alpha \\ \mu_m &= \mu_l\rho_w + (1 - a_l)\mu_\alpha \end{aligned} \tag{2.3}$$

The volume fraction is equal to 0 in areas occupied only by air and 1 in areas occupied only by water. Values in between 0 and 1 are given when both air and water is present in the area. The interface of the two fluids is located in regions of rapid change of the fraction. The free surface is considered to be a material surface, thus the material derivative of the volume fraction must be zero.

$$\frac{\partial a_l}{\partial t} + \vec{u} \cdot \nabla a_l = 0 \tag{2.4}$$

where $\vec{u} = (u, v, w)$ is the three-dimensional velocity vector, ∇= $(\partial_x, \partial_y, \partial_z)$ is the divergence operator and t is the real time variable.

A set of 4 equations has, consequently, arisen, the continuity equation, two momentum equations, and the volume of fluid equation to capture the free surface. The system is not yet closed, as the Reynolds stresses added from the RANS approach to model the effects of viscosity has added extra variables. The closure of the system is completed in section 2.5, with the selection of a suitable turbulence model.

For the solution of the system of the incompressible equations, in a way that also respects the physical reality, a challenge arises due to the decoupling of the mass and momentum equations, as the pressure is absent in the former. Techniques to circumvent this problem, by linking the two equations are the well-known algorithms SIMPLE, PIMPLE, PISO, and others. However, the novelty of MaPFlow lies in its use of the Artificial Compressibility (AC) method to achieve the physical coupling of the two equations.

2.2 Artificial compressibility

The coupling of the continuity equation with the momentum equations is achieved using the artificial compressibility method by adding a pseudo-time derivative of pressure (p), as is shown in equation (5). The artificial compressibility factor β regulates the influence of the pseudo-time derivative.

$$\frac{1}{\beta}\frac{\partial p}{\partial \tau} + \nabla \cdot \vec{u} = 0 \qquad (2.5)$$

, where τ denotes the pseudo-time.

As an iterative numerical procedure takes place in pseudo-time, to arrive at a solution for the current real time step, equation (2.5) must not be different from (2.1), thus the pseudo-time derivative should be equal to 0 when convergence is achieved.

In essence, the AC method assumes a relation between pressure and density during convergence. This relation resembles the compressible definition of sound speed, with the difference in this case that the parameter β is a numerical parameter that regulates convergence.

$$\frac{\partial \rho}{\partial p}\,|_{\tau} = \frac{1}{\beta} \qquad (2.6)$$

The process to obtain the final continuity equation is as follows:

$$\frac{\partial \rho}{\partial t} + \frac{\partial \rho}{\partial \tau} + \nabla \cdot (\rho\, \vec{u}) = 0$$

Expanding the terms and omitting the zero terms due to incompressibility:

$$\frac{\partial \rho}{\partial t} + \frac{\partial \rho}{\partial \tau} + \rho \nabla \cdot\, \vec{u} + \,\vec{u}\, \cdot \nabla \rho = 0 \rightarrow$$

$$\frac{\partial \rho}{\partial \tau} + \rho\, \nabla \cdot\, \vec{u} = 0$$

Applying the chain rule to the pseudo-time derivative we get:

$$\frac{\partial \rho}{\partial p}|_{\tau}\frac{\partial p}{\partial \tau}+\rho\nabla\cdot\ \vec{u}=0$$

Substituting the pressure to density pseudo-derivative we end up with the final form of the coupled continuity equation:

$$\frac{1}{\rho\beta}\frac{\partial p}{\partial \tau}+\nabla\cdot\vec{v}=0 \tag{2.7}$$

The convergence in pseudo-time is achieved when $\frac{\partial p}{\partial \tau}=0$.

Similarly, a fictitious time derivative is also added to the conservative form of the conservation of momentum equation:

$$\frac{\partial(\rho\vec{v})}{\partial t}+\frac{\partial(\rho\vec{v})}{\partial \tau}+\nabla(\rho\vec{v}\cdot\vec{v})=-\nabla p+\nabla\bar{\sigma}+\vec{F}_B \tag{2.8}$$

Temporal terms are expanded, as shown below. Note that density is not constant in time here, because of the mixture fluid properties which change in time close to the free surface.

$$\frac{\partial(\rho\vec{v})}{\partial t}=\rho\frac{\partial\vec{v}}{\partial t}+\vec{v}\frac{\partial\rho}{\partial t}\rightarrow$$

$$\frac{\partial(\rho\vec{v})}{\partial t}=\rho\frac{\partial\vec{v}}{\partial t}+\vec{v}\frac{\partial}{\partial t}(a_l\Delta\rho+\rho_a)\rightarrow$$

$$\frac{\partial(\rho\vec{v})}{\partial t}=\rho\frac{\partial\vec{v}}{\partial t}+\vec{v}\Delta\rho\frac{\partial a_l}{\partial t} \tag{2.9}$$

VOF's transport equation, finally, is treated similarly:

$$\frac{\partial\alpha_l}{\partial t}+\frac{\partial\alpha}{\partial\tau}+\frac{\alpha_l}{\rho_m\beta}\frac{\partial p}{\partial\tau}+\nabla\cdot(\vec{v}\alpha_l)=0 \tag{2.10}$$

The set of equations above (2.7), (2.8), and (2.10), constitute a fully coupled system of equations that are capable of describing two-phase flows. The introduction of the AC method makes the system hyperbolic in pseudo-time, and thus numerical techniques used for such solvers can be used. The initial set of equations has to be satisfied when the system converges in pseudo-time, by eliminating pseudo-time derivatives.

Nevertheless, several difficulties have to be resolved when solving this system of equations. The density, which appears in the eigenvalues of the system, yields it stiff for high density ratios and, secondly, the system cannot be written in conservative form. The Kunz preconditioner [20] is employed to mitigate these difficulties.

Time accurate computations can be made using the AC method, treating every unsteady timestep as a steady state problem solved in pseudo-time. In order to express the governing equations as a coupled system of equations, the time derivatives are expressed as a sum of time derivatives for velocity and density. The governing equations can be written in the following integrated form.

$$\Gamma \int_{\Omega} \frac{\partial \vec{Q}}{\partial \tau} \mathrm{d}\Omega + \Gamma_e \int_{\Omega} \frac{\partial \vec{Q}}{\partial t} \mathrm{d}\Omega + \int_{\partial\Omega} \left(\vec{F_c} - \vec{F_v}\right) \mathrm{d}S = \int_{\Omega} \vec{S_q} \mathrm{d}\Omega \tag{2.11}$$

This system of equations (2.7), (2.8) and (2.10), is a fully coupled system of equations. These equations express the governing equations with respect to the primitive variables $\vec{Q}$. To cast the system in conservative form, the transformation matrix Γ_e is used. The conservative variables are given by the vector $\vec{U}$. The three-dimension vector of velocity is denoted with $\vec{v}$, while *p* is the pressure.

$$\vec{Q} = [p \quad \vec{v} \quad \alpha_l]^T \ , \qquad \Gamma_e = \begin{bmatrix} 0 & 0 & 0 \\ 0 & \rho_m I_{3\times3} & \vec{v}\Delta\rho \\ 0 & 0 & 1 \end{bmatrix} \tag{2.12}$$

Γ_e is the Jacobian matrix and Γ the Kunz precondition matrix given below, where $\Delta\rho$ is the density difference between the heavier and the lighter, and fluid I_{3x3} is the 3x3 identity matrix.

$$\vec{U} = [0 \quad \rho\vec{v} \quad \alpha_l]^T \qquad \frac{\partial \vec{U}}{\partial t} = \Gamma_e \frac{\partial \vec{Q}}{\partial t}$$

$$\Gamma_e = \begin{bmatrix} 0 & 0 & 0 \\ 0 & \rho_m I & \vec{v}\Delta\rho \\ 0 & 0 & 1 \end{bmatrix} \tag{2.13}$$

Finally, the convective and viscous fluxes can be summarized as:

$$\vec{F_c} = \begin{bmatrix} V_n \\ \rho_m u \Delta V + p n_x \\ \rho_m v \Delta V + p n_y \\ \rho_m w \Delta V + p n_z \\ \alpha_l \Delta V \end{bmatrix} \ , \qquad \vec{F_v} = \begin{bmatrix} 0 \\ \tau_{xx} n_x + \tau_{xy} n_y + \tau_{xz} n_z \\ \tau_{yx} n_x + \tau_{yy} n_y + \tau_{yz} n_z \\ \tau_{zx} n_x + \tau_{zy} n_y + \tau_{zz} n_z \\ 0 \end{bmatrix} \tag{2.14}$$

Where $V_n = \vec{u} \cdot \vec{n}$, $V_g = \overrightarrow{u_{vol}} \cdot \vec{n}$, $\Delta V = V_n - V_g$, while $\overrightarrow{u_{vol}}$ is the velocity of the control volume and $\vec{n}$ is the surface normal of the control volume. The viscous stresses t_{ij} are computed as

$$t_{ij} = (\mu_m + \mu_t)\left(\frac{\partial u_i}{\partial x_j} + \frac{\partial u_j}{\partial x_i}\right) - \frac{2}{3}\rho \delta_{ij} k \tag{2.15}$$

where μ_t is the turbulent dynamic viscosity, k is the turbulent kinetic energy and δ_{ij} is the Kronecker delta.

2.3 Spatial Discretization

2.3.1 Finite Volume Method

The finite volume method is used by MaPFlow to discretize the above system of equations. Space is discretized in using a mesh consisting of cells, where for each cell a cell center and a number of faces are defined. The center of the cell is defined as the geometrical center and the faces are the boundaries of the cell. The unknown primitive variables are expressed in an integrated form over the volume of the cell, D_i :

$$\overrightarrow{\overline{Q}} = \frac{1}{D_i}\int_{D_i} \vec{Q}(\vec{x};t)dD \tag{2.16}$$

The surface terms are constant throughout the area (or length for 2D) of each face, thus the surface integrals degenerate into a sum of the flux terms computed at the midpoint of each face. Similarly, the volume terms are considered constant throughout the volume of the cell. The final discretized form of the spatial terms of equations is expressed as:

$$\overrightarrow{R_{D_\imath}} \simeq \sum_{f}^{N_f} \left(\overrightarrow{F_c} - \overrightarrow{F_v}\right)_f \Delta S_f - D_i \overrightarrow{S_q} \tag{2.17}$$

, where $\overrightarrow{R_{D_\imath}}$ is the spatial residual of Equation (2.11).

The following problem emerges when calculating the inviscid terms at a given face. The value of the primitive variables, $\vec{Q}$, is extrapolated from the center of the cell to the face, as thoroughly explained in the following section named “Reconstruction Schemes”. However, the values extrapolated from the Right and the Left cell, namely $\overrightarrow{Q_R}$ and $\overrightarrow{Q_L}$ respectively, are different. A discontinuity is therefore apparent and needs to be dealt with. These kinds of problems are called Riemann Problems and refer to hyperbolic differential equations with discontinuous initial conditions. It is worth noticing that the hyperbolic nature of Equation (2.11) is solely due to the pseudo-time embedded in the equations. Once the pseudo-time terms are eliminated the equation loses its hyperbolic character and the original governing equations are recovered. In MaPFlow the approximate Riemann solver of Roe [21] is implemented to solve the Riemann problem.

A Jacobian matrix for the inviscid (or equivalently called convective) fluxes is created so to express the problem in terms of the primitive variables:

$$A_C = \frac{\partial \overrightarrow{F_c}}{\partial \vec{Q}} \tag{2.18}$$

However, the eigenvalues of the Jacobian matrix A_c depend on the density field which is unwanted as mentioned earlier. For this reason, the preconditioning matrix Γ_e is used in the following way:

$$A_c = \frac{\partial \overrightarrow{F_c}}{\partial \vec{Q}} = \Gamma \Gamma^{-1} A_c = \Gamma\, \underline{\underline{\mathrm{A_c}}} \tag{2.19}$$

The preconditioner Jacobian matrix $\underline{\underline{A_c}}$ takes the following form:

$$\underline{\underline{A_c}} = \begin{bmatrix} 0 & n_x & n_y & n_z & 0 \\ n_x & \rho_m(n_x u + \Delta V) & \rho_m n_y u & \rho_m n_z u & u\Delta V \Delta\rho \\ n_y & \rho_m n_x v & \rho_m\left(n_y v + \Delta V\right) & \rho_m n_z v & v\Delta V\Delta\rho \\ n_z & \rho_m n_x w & \rho_m n_y w & \rho_m(n_z w + \Delta V) & w\Delta V\Delta\rho \\ 0 & \alpha_l n_x & \alpha_l n_y & \alpha_l n_z & \Delta V \end{bmatrix} \tag{2.20}$$

Finally the convective fluxes are calculated at a face, f, by using the Roe approximate Riemann solver [21] in the following way:

$$\vec{F}_{c,f} = \frac{1}{2}\left(\vec{F}_c(\vec{Q}_R) + \vec{F}_c(\vec{Q}_L)\right) - \frac{1}{2}\Gamma \, \left| \overline{\underline{\underline{A_c}}} \right|_f (\vec{Q}_R - \vec{Q}_L) \tag{2.21}$$

The Jacobian $\left|\underline{\underline{\mathrm{A_c}}}\right|$ is not to be confused with the determinant or the absolute value of $\underline{\underline{\mathrm{A_c}}}$. It is derived by using the absolute values of matrix $\underline{\underline{\Lambda}}$ which is a diagonal matrix consisting of the eigenvalues of $\underline{\underline{\mathrm{A_c}}}$. $\left|\underline{\underline{\mathrm{A_c}}}\right|$ is therefore expressed as:

$$\left|\underline{\underline{\mathrm{A_c}}}\right| = \underline{\underline{R^{-1}}} \left|\underline{\underline{\Lambda}}\right| \underline{\underline{R}} \tag{2.22}$$

,where $\underline{\underline{R^{-1}}}$ is constructed by arranging the left eigenvectors of $\underline{\underline{\mathrm{A_c}}}$ in a column wise order and $\underline{\underline{\mathrm{R}}}$ by arranging the right eigenvectors in a row wise order.

The values of $\vec{u}$ and ρ used in the calculation of (2.22) at a face are Roe averaged quantities defined as:

$$\bar{\bar{\vec{u}}} = \frac{\sqrt{\rho_R}\,\overrightarrow{u_R} + \sqrt{\rho_L}\,\overrightarrow{u_L}}{\sqrt{\rho_R} + \sqrt{\rho_L}} \;, \bar{\rho} = \sqrt{\rho_\alpha \rho_l} \tag{2.23}$$

The eigenvalues of the Jacobian $\underline{\underline{\mathrm{A_c}}}$ are similarly calculated as in the case of a compressible fluid and are shown below. It is worth repeating that the hyperbolic character of the equations vanishes when convergence is achieved. Thus, the equations are hyperbolic only in pseudo time.

$$\begin{gathered} \lambda_{1,2,5} = V_n - V_g \\ \lambda_3 = V_n - c - \frac{V_g}{2} \\ \lambda_4 = V_n + c - \frac{V_g}{2} \end{gathered} \tag{2.24}$$

, where V_n is the velocity of the flow field projected on the normal vector of each face and V_g being the velocity of the control volumes boundary projected also on the normal vector of each face. The speed of sound is defined in two-phase flow simulations as:

$$c = \sqrt{\beta + \left(V_n - \frac{V_g}{2}\right)^2} \tag{2.25}$$

The eigenvectors $\underline{\underline{R}}$ and $\underline{\underline{R^{-1}}}$ are therefore given by the equations:

$$\underline{\underline{R}} = \begin{bmatrix} 0 & 0 & -\rho_m c_m & \rho_m c_p & 0 \\ x_1 & x_2 & n_x + \dfrac{u\lambda_3}{\beta} & n_x + \dfrac{u\lambda_4}{\beta} & 0 \\ y_1 & y_2 & n_y + \dfrac{v\lambda_3}{\beta} & n_y + \dfrac{v\lambda_4}{\beta} & 0 \\ z_1 & z_2 & n_z + \dfrac{w\lambda_3}{\beta} & n_z + \dfrac{w\lambda_4}{\beta} & 0 \\ 0 & 0 & 0 & 0 & 1 \end{bmatrix} \tag{2.26}$$

and,

$$\underline{\underline{R}}^{-1} = \begin{bmatrix} \begin{array}{r} [h]\dfrac{1}{\rho_m c_g}\left[n_x\left(wy_2 - vz_2\right) + \right. \\ n_y\left(uz_2 - wx_2\right) + \\ \left. n_z\left(vx_2 - uy_2\right)\right] \end{array} & \begin{array}{r} [h]\dfrac{1}{c_g}\left[\beta\left(n_z y_2 - n_y z_2\right) + \right. \\ \left. \Delta V\left(wy_2 - vz_2\right)\right] \end{array} & \begin{array}{r} [h]\dfrac{1}{c_g}\left[\beta\left(n_x z_2 - n_z x_2\right) + \right. \\ \left. \Delta V\left(uz_2 - wx_2\right)\right] \end{array} & \begin{array}{r} [h]\dfrac{1}{c_g}\left[\beta\left(n_y x_2 - n_x y_2\right) + \right. \\ \left. \Delta V\left(vx_2 - uy_2\right)\right] \end{array} & 0 \\ \begin{array}{r} [h]\dfrac{1}{\rho_m c_g}\left[n_x\left(vz_1 - wy_1\right) + \right. \\ n_y\left(wx_1 - uz_1\right) + \\ \left. n_z\left(uy_1 - vx_1\right)\right] \end{array} & \begin{array}{r} [h]\dfrac{1}{c_g}\left[\beta\left(n_y z_1 - n_z y_1\right) + \right. \\ \left. \Delta V\left(wy_1 - vz_1\right)\right] \end{array} & \begin{array}{r} [h]\dfrac{1}{c_g}\left[\beta\left(n_z x_1 - n_x z_1\right) + \right. \\ \left. \Delta V\left(wx_1 - uz_1\right)\right] \end{array} & \begin{array}{r} [h]\dfrac{1}{c_g}\left[\beta\left(n_x y_1 - n_y x_1\right) + \right. \\ \left. \Delta V\left(vx_1 - uy_1\right)\right] \end{array} & 0 \\ -\dfrac{1}{\rho_m\, 2c\, c_g}\left(\beta + \lambda_4 V_n\right) & \dfrac{1}{2c\, c_g}\beta c_p n_x & \dfrac{1}{2c\, c_g}\beta c_p n_y & \dfrac{1}{2c\, c_g}\beta c_p n_z & 0 \\ \dfrac{1}{\rho_m\, 2c\, c_g}\left(\beta + \lambda_3 V_n\right) & \dfrac{1}{2c\, c_g}\beta c_m n_x & \dfrac{1}{2c\, c_g}\beta c_m n_y & \dfrac{1}{2c\, c_g}\beta c_m n_z & 0 \\ 0 & 0 & 0 & 0 & 1 \end{bmatrix}$$

In the above equations c_m, c_p and c_g are expressed as:

$$c_m = c - \frac{V_g}{2}, c_p = c + \frac{V_g}{2}, c_g = \beta + V_n \Delta V \tag{2.27}$$

2.3.2 Reconstruction Schemes

MaPFlow is a cell centered code. This means that values of primitive and conservative variables are known on the center of each finite cell. However, in order to calculate the flux terms of equation (2.14), the information of those variables should be transferred to the faces of the cell. This extrapolation procedure is called reconstruction of the flow field and various methods can be utilized. Due to the different nature of each equation of (2.14) an appropriate reconstruction scheme is chosen for each of them. In Figure 2.1 a schematic representation of the reconstruction is shown, where information is transferred from the center of the adjacent cells, D_i, and D_j, to the common face.

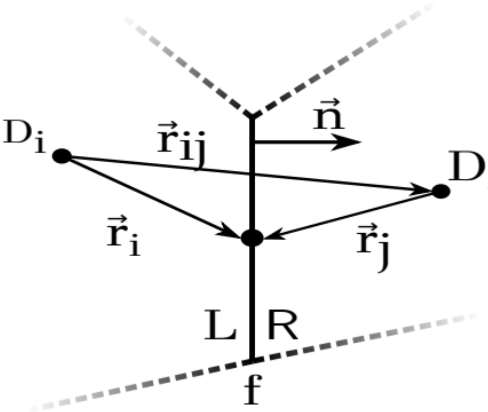

Figure 2.1 Reconstruction of variables on face f

Velocity Field Reconstruction

For the velocity field, the PLR (Piecewise Linear Interpolation) reconstruction scheme is implemented, as is stated in equation (2.28). This scheme is reminiscent of a Taylor expansion series of the 2nd degree. The velocity field is continuous everywhere, including the free surface since surface tension is neglected. Thus, a simple scheme is sufficient and no limiter are necessary.

$$\begin{aligned} \vec{u}_L &= \vec{u}_i + \nabla \vec{u}_i \, \vec{r}_i \\ \vec{u}_R &= \vec{u}_j + \nabla \vec{u}_j \, \vec{r}_j \end{aligned} \tag{2.28}$$

Pressure Filed Reconstruction

In cases of single-phase simulation, where no pressure jump takes place and continuity is maintained across the whole domain, the PLR scheme can be used. In two phase flows, however, a jump in the pressure gradient takes place in the free surface, due to the difference in densities of the fluids and the discontinuous transition between them. In those cases, MaPFlow uses the PLR scheme away from the free surface. Near the free surface the following condition must be satisfied:

$$\begin{gathered} \left.\frac{\nabla p}{\rho}\right|_R - \left.\frac{\nabla p}{\rho}\right|_L = 0 \Rightarrow \\ \left[\frac{\nabla p}{\rho}\right] = 0 \end{gathered} \tag{2.29}$$

To overcome this challenge and satisfy the above condition MaPFlow adopts a density-based interpolation scheme. Many solutions have been proposed, but the solution in [22] is chosen by MaPFlow for the pressure field reconstruction near the free surface.

Volume Fraction Reconstruction

The reconstruction of the Volume fraction is of high importance, since the locus and resolution of the free surface is affected significantly. Errors might be added by numerical diffusion which has to be mitigated. For this reason, a compressive scheme has to be adopted, meaning that values of the volume fraction between 0 and 1 should be driven to their closest bound.

The scheme adopted also needs to satisfy boundedness and be highly accurate even in high CFL numbers. Many sophisticated free surface capturing schemes have been introduced, most based on Leonard's Normalized Variable Diagram (NVD) [23], namely CISCAM [24], HRIC [25], BICS [26], STACS [27] and MGDS. MaPFlow offers a variety of those schemes to the user for VOF reconstruction. The BICS scheme is used in this thesis, as it gives quite accurate results with very low numerical diffusion.

2.4 Temporal Discretization

The system of equations can be written in the following implicit formulation to allow us to implement the time discretization:

$$\Gamma \frac{\partial(\vec{Q}^* D_i)}{\partial \tau} + \vec{R}^* = 0 \tag{2.30}$$

, where $\vec{Q}^*$ is the unknown primitive variables. The integral is incorporated in $\vec{Q}^*$ due to the spatial discretization as it is explained in the previous section.

$\vec{R}^*$ is the unsteady residual consisting of the spatial terms examined before denoted as $\vec{R}^*_{D_i}(\overrightarrow{Q^*})$ and the unsteady real-time term:

$$\overrightarrow{R^*} = \overrightarrow{R_{D_i}}(\overrightarrow{Q^*}) + \frac{\Gamma_e \partial(\vec{Q}^* D_i)}{\partial t} \tag{2.31}$$

There exist two time indexes, n refers to the real time and denotes the index of the known time solution while k is pseudo-time index or better phrased is the internal iterator of the steady problem. As the real time step marches, the steady state problem begins with k = 0 and the vector of the unknown primitive values is initialized based on the previously known time solution as $\vec{Q}^* = \vec{Q}^n$. While iterating in the steady state problem, $\vec{Q}^*$ does not satisfy the original unsteady problem, until convergence is achieved and the pseudo-time derivative is eliminated, $\frac{\partial(\vec{Q}^* D_i)}{\partial \tau} = 0$. Convergence is satisfied through the condition $\vec{R}^* \rightarrow 0$ and the primitive variables are updated, $\vec{Q}^* \rightarrow \vec{Q}^{n+1}$.

A BDF scheme is implemented for the unsteady term discretization resulting in a series expansion of successive levels backwards in time:

$$\frac{\partial(\vec{Q} D_i)}{\partial t} = \frac{1}{\Delta t}\left[\varphi_{n+1}(D_i\vec{Q})^{n+1} + \varphi_n(D_i\vec{Q})^{n} + \varphi_{n-1}(D_i\vec{Q})^{n-1} + \varphi_{n-2}(D_i\vec{Q})^{n-2} + \cdots\right] \tag{2.32}$$

Possible changes in the control volume should be accounted for by satisfying the *Geometric Conservation Law (GCL):*

$$\frac{d}{dt}\int_{D_i(t)} \mathrm{d}D = \oint_{\partial D_i(t)} \vec{u}_{\mathrm{vol}} \cdot \vec{n}\mathrm{d}S \tag{2.33}$$

Using a similar discretization approach as with the unsteady term, the GCL takes the following form:

$$\frac{1}{\Delta t}\left[\left(\varphi_{n+1}D_i^{n+1}+\varphi_n D_i^{n}+\varphi_{n-1}D_i^{n-1}+\varphi_{n-2}D_i^{n-2}\right)+\cdots\right]=\vec{R}_{GCL}^{n+1} \tag{2.34}$$

, where the residual $\vec{R}_{GCL}^{n+1}$ is defined as:

$$\overrightarrow{R_{GCL}^{n+1}}=\sum_{f}^{N_f}\left(V_g \Delta S\right)_f^{n+1} \tag{2.35}$$

The GCL is then embedded in the unsteady term discretization to ensure its satisfaction yielding a second order accurate scheme in time:

$$\begin{gathered}\frac{\partial\left(\vec{Q}D_i\right)}{\partial t}=\vec{Q}^{n}\vec{R}_{GCL}^{n+1}+\\ \frac{1}{\Delta t}\left[\varphi_{n+1}\left(\vec{Q}^{n+1}-\vec{Q}^{n}\right)D_i^{n+1}+\varphi_{n-1}\left(\vec{Q}^{n-1}-\vec{Q}^{n}\right)D_i^{n-1}+\varphi_{n-2}\left(\vec{Q}^{n-2}-\vec{Q}^{n}\right)D_i^{n-2}+\cdots\right]\end{gathered} \tag{2.36}$$

For the fictitious time derivative a first order backwards difference scheme is employed:

$$\frac{\partial\left(\vec{Q}^{*}D_i\right)}{\partial \tau}=D_i^{n+1}\frac{\vec{Q}^{*,k+1}-\vec{Q}^{*,k}}{\Delta\tau}=D_i^{n+1}\frac{\Delta\vec{Q}^{*,k}}{\Delta\tau} \tag{2.37}$$

During pseudo-time iterations a local time stepping technique is used, allowing for different time steps between cells thus improving convergence:

$$\Delta\tau = CFL\frac{D_i}{\hat{\Lambda}_{c,i}} \tag{2.38}$$

, where $\hat{\Lambda}_{c,i}$ is the convective spectral radii defined by:

$$\hat{\Lambda}_{c,i}=\sum_{j=1}^{N\_f}\left(\left|\overrightarrow{V_n}+c-\frac{V_g}{2}\right|\right)_{ij}\Delta S_{ij}$$

2.5 Turbulence Modeling

MaPFlow is a RANS solver using turbulence models to calculate turbulence viscosity μ_t and from that the required Reynolds Stresses using the Boussinesq hypothesis. The k-omega SST model is chosen as the turbulence model. Free surface flows in RANS solvers, however, face a drawback, as the shear layer created in the interface between the fluids results in overproduction of turbulent viscosity μ_t and thus leads to artificial damping of the propagated waves.

This effect can be mitigated using a buoyancy term to the kinetic energy, proposed by Devolder et al. [28], to counteract the transfer of energy into turbulence:

$$G_b = \frac{v_t}{\sigma_t} \frac{\partial \rho}{\partial x_j} g_j \tag{2.39}$$

This term is sufficient for non-complex flows, which is enough for this particular case where the body is fully submerged at all times. Surface piercing geometries, for example, would require further treatment.

3. Fluid Structure Interaction Strong Coupling Solver

The movement of the flapping foil, due to its passive nature, is defined by its interaction with its surrounding fluid, but also the state of the fluid around it is defined by its movement. It is obvious that there must exist a coupling between the equations of the fluid, with those that define the body's motion. These kinds of problems can be solved by Fluid Structure Interaction solvers that add to the process a solution of Newton's second law and work in collaboration with the CFD solver, for every timestep.

Fluid Structure interaction solvers are necessary in many different kinds of engineering applications involving fluids, such as flattering in aircraft wings or oscillations in underwater pipelines. The structures are by nature deformable and if the deformations are significant, additional equations have to be included, as energy is transferred to the body's elastic deformations. Nonetheless, the deformations of the flapping foil's body are not significant as forces are not that large, thus the body is taken to be completely rigid, simplifying the process.

An appropriate communication between the two physical problems of rigid body and fluid dynamics, must be implemented. The flow field variables are pressure, velocities and Volume Fraction for the two-phase case. The variables that define the body's movement in the 2D plane are its accelerations that are produced by the loads that the fluid applies to the body and any external loads, including for example springs or dampers.

$$\begin{pmatrix} p \\ u \\ v \\ \mathrm{a}_l \end{pmatrix} \Leftrightarrow \begin{pmatrix} \ddot{x} \\ \ddot{y} \\ \ddot{\theta} \end{pmatrix} \tag{3.1}$$

The loads are easily calculated from the flow field by integrating the pressure and shear force on the surface of the body. Forces and torques with respect to the pitching axis are then calculated. The solver is capable of solving a coupled system of ODEs formed from Newton's Second Law by time integration using an appropriate scheme.

$$P \Rightarrow \int_{\partial B} (P + \mu \nabla u) \cdot \vec{n} dS \; F_x, F_y, M_z \Rightarrow \begin{pmatrix} m_x \ddot{x} + c_x \dot{x} + k_x x = F_x \\ m_y \ddot{y} + c_y \dot{y} + k_y y = F_y \\ I_z \ddot{\theta} + c_\theta \dot{\theta} + k_\theta \theta = M_z \end{pmatrix} \Rightarrow \begin{matrix} \ddot{x} & \dot{x} & x \\ \ddot{y} & \dot{y} & y \\ \ddot{\theta} & \dot{\theta} & \theta \end{matrix} \tag{3.2}$$

, where ∂B is the boundary surface of the rigid body.

Figure 3.1 shows the logical sequence of processes used for coupling the CFD solver with the Rigid Body Dynamics solver:

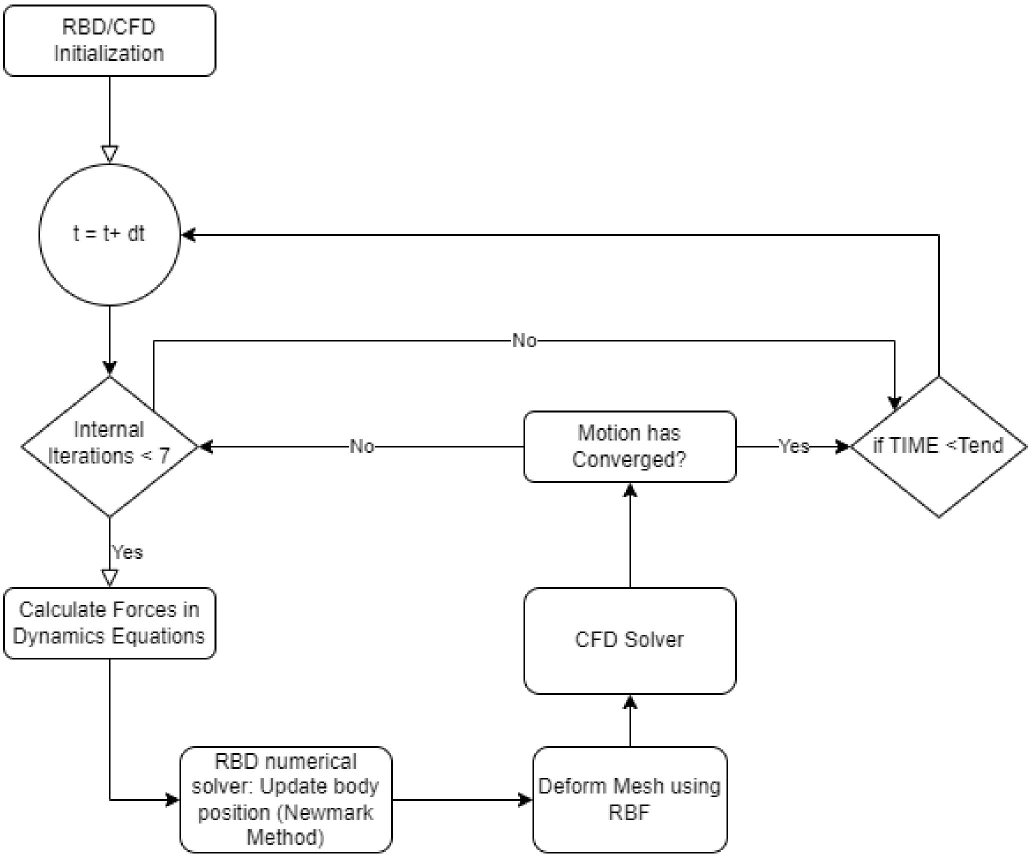

Figure 3.1 Flow Chart of the strong coupling between CFD and RBD solver

The process is also explained below more thoroughly:

1) The rigid body's parameters are initialized: its degrees of freedom, initial conditions, mass, damping and stiffness matrices. If the external loads are coupled with each other, the coupling terms also have to be included inside the matrices of the parameters.
2) Time step marches
3) The Navier-Stokes equations are solved and the pressure field around the body is acquired.

-Rigid Body Solver Inner Loop begins-

4) If the internal loop iterations are less than a specified number (here 7), through integration of the fluid variables on the body, the loads applied to it are calculated. This is achieved by integration of the pressure and shear force on every face on the surface of the body.

5) These loads are assigned to the right-hand side of the equations of motion. Additional external forces, for example from spring or dampers, are calculated at this stage.

6) The system of ODEs, listed above, is solved numerically, by integration, using the Newmark method. The unknown variables are exactly equal to the number of equations. Kinematic values of the previous time step are used in the calculation as initial conditions.

7) Translation of the body is obtained. The body is transferred to its new position and the mesh is deformed accordingly with the RBF method.

8) The Navier-Stokes equations are solved, with the displacements and velocities calculated from step 6. The mesh is also moved according to the displacements, using the Radial Basis Functions method.

9) If the displacements have sufficiently converged to a value, meaning that displacements differ from the previous steps per some user defined value, the inner loop exits, else, the algorithm restarts from step 4, using the calculated kinematics of step 7.

To check for convergence the infinity norm is applied as per below:

$$eps = \|B\|_{\infty}$$

, where $B = u - u_{new}$ and eps is defined by the user.

- Rigid Body Inner Loop is exited -

10) The final displacements, velocities and accelerations are saved to be used as initial conditions to the following timestep. Then, unless the specified end of the simulation has been reached, time step marches.

The presence of the inner loop synchronizes the two solvers, giving a final solution that accurately satisfies both the fluid equations and the rigid body equations. This technique is called the strong coupling solver, as opposed to the weak coupling solver described below.

A simple, yet quite effective approach would be to use the weak coupling solver, meaning that at first, the flow field is calculated, then solve for the rigid body motion equations and then recalculate the flow field before moving on to the next time step. This approach is quite accurate and much less computationally expensive, but the well-known added mass instability problem arises, due to the explicit solution [29]. This instability usually occurs in problems with large deformations and lightweight structures.

The strongly coupled solver, implicit by nature, bypasses the added mass instability problem, for any case. However, multiple solutions of the flow field equations per timestep (as mavy as 7) require a lot of computational time. The strongly coupled solver is used in this study so that there is no restriction in our choice of parameters for the moving rigid body.

4. Fully passive foil setup and numerical framework

This section, initially describes the fully passive flapping foil device, outlines the dynamics equations that describe the device, which is immersed in water, facing an incoming horizontal, uniform flow. The definitions for power and efficiency are also given. Then, the numerical setup of the code, and the mesh's general structure are presented. Afterwards, mesh independence and timestep independence studies take place in order to determine the necessary refinement of the grid and the maximum timestep that gives quality results. Finally, to validate the setup, it is compared with experimental results.

4.1 Physical model description

The flapping foil device is studied here in two dimensions. The foil's shape is constant along its span, and the span itself can be very large with end plates attached at the tips to partly avoid the negative effect of tip vortices. Three dimensional effects of active flapping foils were studied by [30] for a foil with finite aspect ratio (AR) and no end plates. It was shown that the three-dimensional effects are very significant and cannot be ignored, unless the AR is extremely large. Even for a large AR = 8, the efficiency drop compared to the 2D case was 6.4%, while for smaller ARs the drop was much higher. In this thesis, however the 2D problem is solved as a first step, and as the AR can possibly be very large without structural problems. Also, keeping the computational cost low is necessary in order to examine numerous cases and perform a wide parametric study.

The fully passive flapping foil device is completely described Figure 4.1. In the two-dimensional problem, three degrees of freedom exist, namely surge, heave and pitch as shown in the bottom right side of the figure. The device is comprised of a foil that is attached to linear springs and dampers in the heave and pitch degrees of freedom, and its movement along the x axis is constricted. Fluid flow has the direction of the x axis, rightwards, as shown in the figure, while gravity acts on the y axis, downwards. The corresponding stiffnesses for the springs are k_y and k_θ and the damping are c_y and c_θ.

The pitching axis is located on the point P, as shown in the figure, which lies on the chord line of the foil, in a distance l_θ from the leading edge. We also denote the distance λ_G from the point P to the center of gravity G of the device's moving parts. A positive value of λ_G means that the center of gravity is located downstream of the pitching axis.

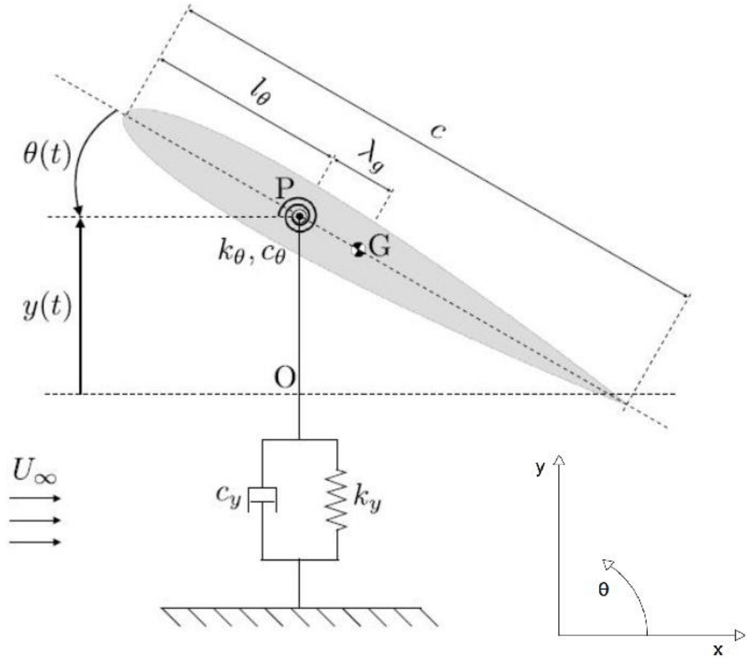

Figure 4.1 Mechanical description of the fully passive foil device.

The foil can start moving from complete rest when fluid starts to flow on the horizontal axis, thus no initial disturbance is necessary, giving rise to a periodical flapping motion, that is close to a sine wave. In order to be able to predict the motion of the foil when the hydrodynamic and linkage loads start acting upon it, we must devise the equations of motion from Newton's second law. Thus, two nonlinear coupled differential equations arise (4.1), one for each of the two degrees of freedom.

$$\begin{gathered} m_y\ddot{y} + c_y\dot{y} + k_y y + \Lambda\left(\dot{\theta}^2 sin\theta - \ddot{\theta} cos\theta\right) = F_y \\ I_\theta\ddot{\theta} + c_\theta\dot{\theta} + k_\theta\theta - m_\theta\lambda_G(\ddot{y}cos\theta) = M_\theta \end{gathered} \tag{4.1}$$

, where m_y is the heaving mass and I_θ the moment of inertia of the foil with respect to the pitching axis P. The distinction for heaving mass is necessary because that might differ from the pitching mass, as some mechanical moving parts may not participate in motions for both degrees of freedom. Finally, F_y is the force exerted by the fluid on the foil in the heave degree of freedom, and M_θ is the torque exerted by the fluid on the foil in the pitch degree of freedom with respect to P.

The fact that the pitching axis location differs from the center of gravity, and the above equations are written with regards to P, gives rise to the well-known Static Imbalance Λ, which couples the two equations. Λ is defined as:

$$\Lambda = \lambda_G m_\theta \tag{4.2}$$

The position of the pitching axis is a significant parameter for this device, which greatly affects its motion and thus its energy output. Energy is transferred from the heaving motion to the pitching motion and vice versa. Results have shown that it does affect the device to the as it regulates energy transfer from the heaving to the pitching motion and vice versa. So, omitting it, although it would lead to a much simpler dynamics problem, would be an oversimplification.

Structural parameters, kinematics variables and Force definitions, are given in non-dimensional form throughout the thesis. The parameters and variables used are presented in Table 1. Stars (*) might be omitted but the author always refers to the non-dimensional form.

Table 1 Structural and kinematics parameters and variables, together with their non-dimensional form.

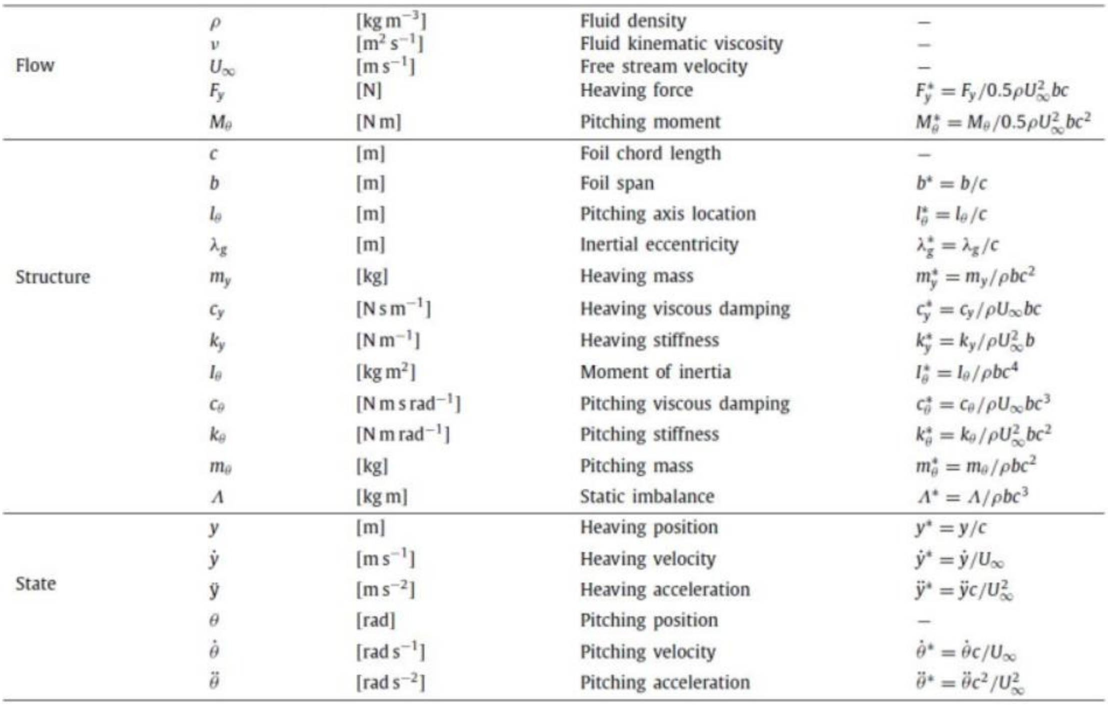

Flow	ρ	[kg m^{-3}]	Fluid density	–
	ν	[m^2 s^{-1}]	Fluid kinematic viscosity	–
	U_∞	[m s^{-1}]	Free stream velocity	–
	F_y	[N]	Heaving force	$F_y^* = F_y/0.5\rho U_\infty^2 bc$
	M_θ	[N m]	Pitching moment	$M_\theta^* = M_\theta/0.5\rho U_\infty^2 bc^2$
Structure	c	[m]	Foil chord length	–
	b	[m]	Foil span	$b^* = b/c$
	l_θ	[m]	Pitching axis location	$l_\theta^* = l_\theta/c$
	λ_g	[m]	Inertial eccentricity	$\lambda_g^* = \lambda_g/c$
	m_y	[kg]	Heaving mass	$m_y^* = m_y/\rho bc^2$
	c_y	[N s m^{-1}]	Heaving viscous damping	$c_y^* = c_y/\rho U_\infty bc$
	k_y	[N m^{-1}]	Heaving stiffness	$k_y^* = k_y/\rho U_\infty^2 b$
	I_θ	[kg m^2]	Moment of inertia	$I_\theta^* = I_\theta/\rho bc^4$
	c_θ	[N m s rad^{-1}]	Pitching viscous damping	$c_\theta^* = c_\theta/\rho U_\infty bc^3$
	k_θ	[N m rad^{-1}]	Pitching stiffness	$k_\theta^* = k_\theta/\rho U_\infty^2 bc^2$
	m_θ	[kg]	Pitching mass	$m_\theta^* = m_\theta/\rho bc^2$
	Λ	[kg m]	Static imbalance	$\Lambda^* = \Lambda/\rho bc^3$
State	y	[m]	Heaving position	$y^* = y/c$
	$\dot{y}$	[m s^{-1}]	Heaving velocity	$\dot{y}^* = \dot{y}/U_\infty$
	$\ddot{y}$	[m s^{-2}]	Heaving acceleration	$\ddot{y}^* = \ddot{y}c/U_\infty^2$
	θ	[rad]	Pitching position	–
	$\dot{\theta}$	[rad s^{-1}]	Pitching velocity	$\dot{\theta}^* = \dot{\theta}c/U_\infty$
	$\ddot{\theta}$	[rad s^{-2}]	Pitching acceleration	$\ddot{\theta}^* = \ddot{\theta}c^2/U_\infty^2$

The energy harvesting done by the electric generator can be modelled as damping in the heave and pitch degrees of freedom. Consequently, the dampers attached to the device emulate the dynamic effect a generator would have on the foil, which is very similar to linear dampers with parameters c_y and c_θ that can be chosen for the desired response.

In order to assess the efficiency of the device, the ratio of the energy harvested divided by the available energy in the incoming flow, in the area swept by the foil is used. This is called the hydraulic efficiency, and is widely used to assess the efficiency of hydraulic turbines. Its definition is given by (4.3):

$$\eta = \frac{1}{N \cdot T}\int_{t_0}^{t_0+N\cdot T} \frac{c_y\dot{y}^2 + c_\theta\dot{\theta}^2}{\frac{1}{2}\rho U_\infty^3 S}\,dt \tag{4.3}$$

, where S is the maximum area perpendicular to the fluid flow that is swept by the foil, being the product of the foils span b, and the maximum vertical distance swept d. For this 2D case b = 1. N is the number of periods T averaged to get the efficiency.

An equally useful metric for the assessment of the device is the average power coefficient, which resembles the definition of η, but the area in the denominator is equal to the chord length times the span of the foil. It defined as:

$$\overline{C_p} = \frac{1}{N \cdot T}\int_{t_0}^{t_0+N\cdot T} \frac{c_y\dot{y}^2 + c_\theta\dot{\theta}^2}{\frac{1}{2}\rho U_\infty^3 bc}\,dt \tag{4.4}$$

Dimensionless force and power coefficients for forces are also defined in order to aid in the analysis of the results:

$$C_L = \frac{F_{y(t)}}{\frac{1}{2}\rho U_\infty^2 bc} \qquad C_M = \frac{M_\theta(t)}{\frac{1}{2}\rho U_\infty^2 bc^2}$$

$$C_{P_y} = \frac{P_{F_y}(t)}{\frac{1}{2}\rho U_\infty^3 bc} \qquad C_{P_\theta} = \frac{P_{M_\theta}(t)}{\frac{1}{2}\rho U_\infty^3 bc} \tag{4.5}$$

4.2 Numerical Setup

Structural and fluid flow parameters

The structural parameters used throughout this thesis for the fully passive flapping foil device, are held constant, and are the same as in [31], where the particular device was constructed and experiments were carried out in a tank test, at conditions where the free surface has no effect. The parameters, along with the Reynold's number and the fluid freestream that are used in the numerical simulations are presented in Table 2 below. A comparison is also made in section 4.5 between Duarte's experimental results and numerical results.

Table 2 Structural Parameters of the fully passive foil device used here.

Parameter	Value	Parameter	Value
c	0.1	Foil Type	NACA0015
Re	$6 \cdot 10^4$	U_∞	1
m^*	0.92	Λ	0.0065
k_θ^*	0.071	c_θ^*	0.052
k_y^*	0.72	c_y^*	0.93
I_θ^*	0.0563	l_θ^*	0.33

Mesh Structure

The general structure of the mesh is presented in Figure 4.2. The final configuration happens in section 4.3 where mesh sensitivity analysis is used to define the density of the grid. The mesh attempts to replicate a towing tank, where the foil is submerged under a free surface, which is visible in Figure 4.3 marked with a red line and surrounded by a horizontal structured refinement zone to capture the sharp transition between the fluids. The width of the zone is 0.4c. The mesh is rectangular with a size of 98x158 chord lengths c. The lower rectangular zone, where water is present, has a depth of 18c and the upper where air is present has a height of 80 c. The foil is submerged at depth S_d which is variable. Quad type cells are used.

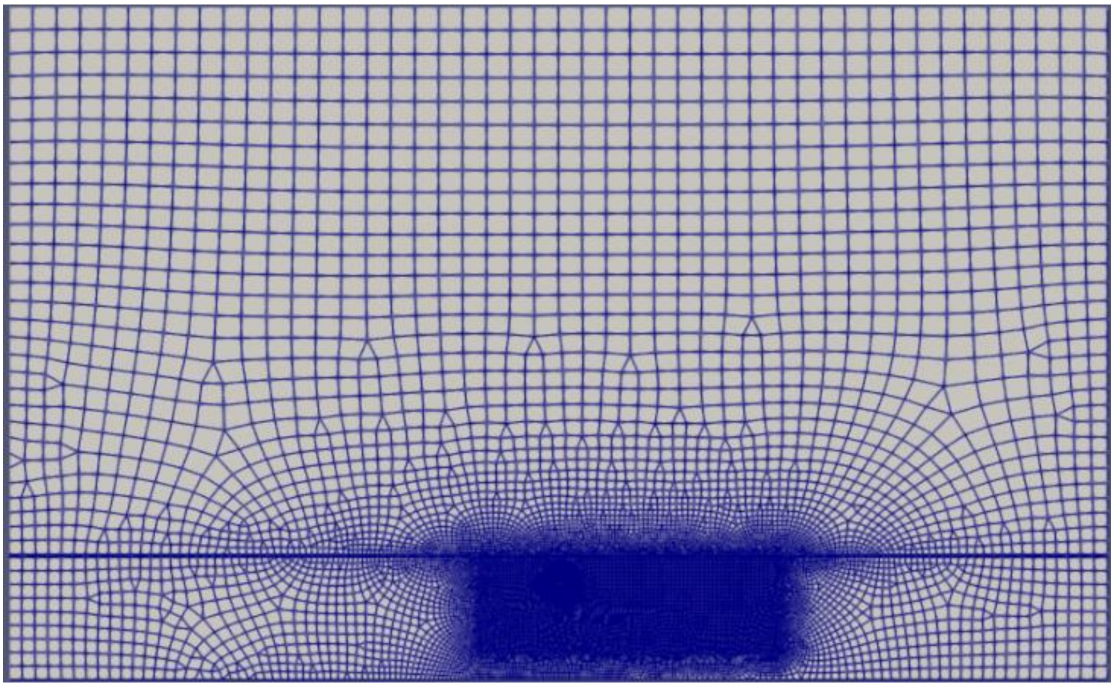

Figure 4.2 The complete computational grid used

.

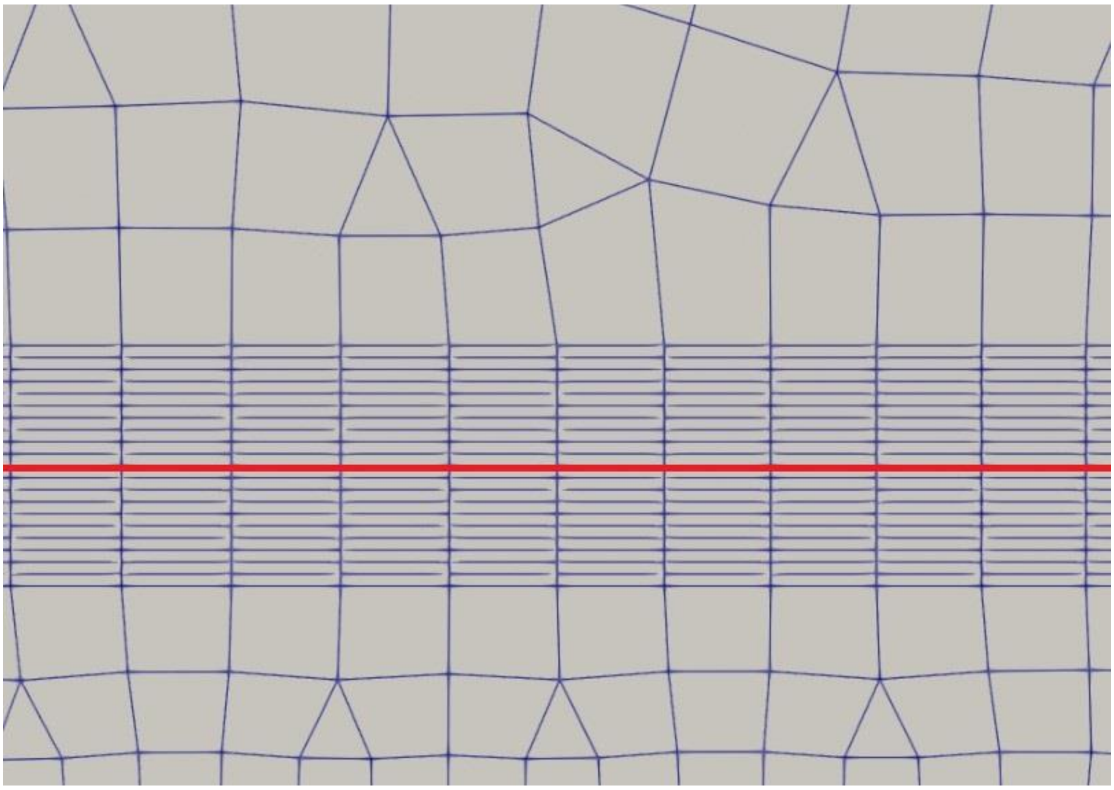

Figure 4.3 Locus and refinement around the free surface

Two refinement zones are also used. The first is mainly used to capture the wake (Figure 4.4), which is expected to reveal a vortex street-like pattern. It begins 12c upstream of the foil and ends 33c downstream. It also begins at 0.5c under the free surface. The height of the box varies based on the foil's depth. This refinement zone has a target size of 0.12c. The second refinement zone, Figure 4.5, is used to accurately capture the complex hydrodynamic phenomenon around the hydrofoil, so that it is adequately resolved. This is a circular one with radius of 3c. It's target size is determined in the mesh dependency study in section 4.3, as it heavily affects the results.

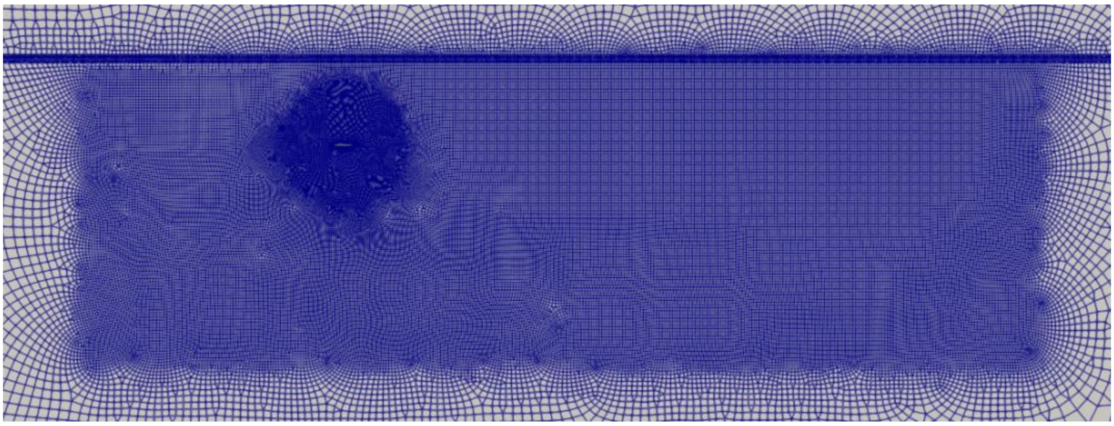

Figure 4.4 Orthogonal refinement zone to capture the rich wake.

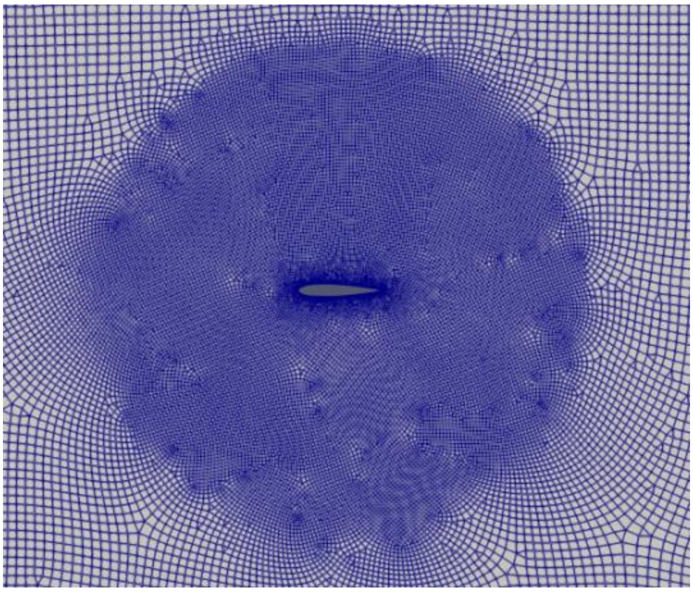

Figure 4.5 Circular refinement zone to capture the complex flowfield around the hydrofoil.

y^+

In order to simulate the effect of the boundary layer as accurately as possible in this high velocity gradient region, so that the results have high accuracy, a $y^+ < 1$ is chosen. The mesh near the foil's boundary is constructed with a structured mesh so that cell heights are suitable to capture the velocity gradients in the boundary layer Figure 4.6.

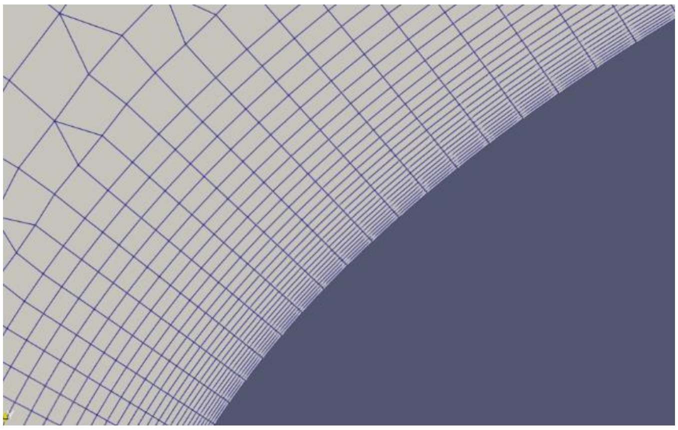

Figure 4.6 Structured mesh on the hydrofoil's surface to capture the boundary layer.

Wave generation and absorption

The finite nature of wave tanks, either numerical or physical, make wave generation and absorption a non-trivial case, as waves can be reflected off of boundaries and affect the solution. Specifically for this case, wave absorption needs to be implemented in the left and right-side boundaries. A possible solution would be to coarsen the computational grid near the boundaries, but this technique does not guarantee zero reflection. A more effective technique which MaPFlow implements is the use of damping zones where the farfield conditions are imposed.

In zones close to the boundaries, that extend for a few wavelengths, appropriate source terms are applied in the momentum equations as explained in [32]. These source terms drive the solution to dampen the waves, by imposing the solution of a calm free surface. Similarly, to generate waves, local velocities are driven appropriately to their desired values to create the specified wave. Their influence is increased as the boundary is approached through a function which increases their strength so that waves are absorbed or generated gradually. Appropriate values for this function are obtained from [32].

Radial Basis Function interpolation scheme for dynamic mesh motion

The rigid body's movement needs to happen along with a suitable movement of the grid around it that maintains the grid quality, meaning that refinements of the grid remain where are needed and cells are not significantly skewed as quality of the solution might be affected.

Radial Basis Functions (RBF) method is used to deform the grid. This method interpolates the displacements of the inner mesh nodes based on the wall nodes of the rigid body. Cells inside a circular region close to the body are only rotated along with the body and not deformed, so that the grid remains attached to the body. Outside this region, cells are deformed, and the rotation of the cells slowly diminishes inside a given larger region so that other structures of the mesh like the bottom are unaffected. The RBF solver uses the displacements obtained by the RBD solver to handle the transformation of the grid around the hydrofoil.

4.3 Mesh Sensitivity analysis under free surface

The results from a mesh dependency study, whose goal is to determine the necessary and adequate density of the grid, are presented here. The consistency of the results with regards to the mesh is also evaluated. As mentioned in section 4.2, the target size of the large rectangular region is 0.12c and its main goal is to capture the rich wake of the foil.

In this particular study, the depth of the foil is held constant at a submergence depth S_d = 9c. What varies is the target size of the circular refinement region, which captures the complex hydrodynamic phenomenon, and is expected to affect the results to a large degree.

Three different refinements were tested: a maximum target length of 2%, 4% and 8% of chord length c for the cell in this area, which are referred to as Cyl2, Cyl4 and Cyl8 respectively. The different meshes can be viewed in Figure 4.7 below.

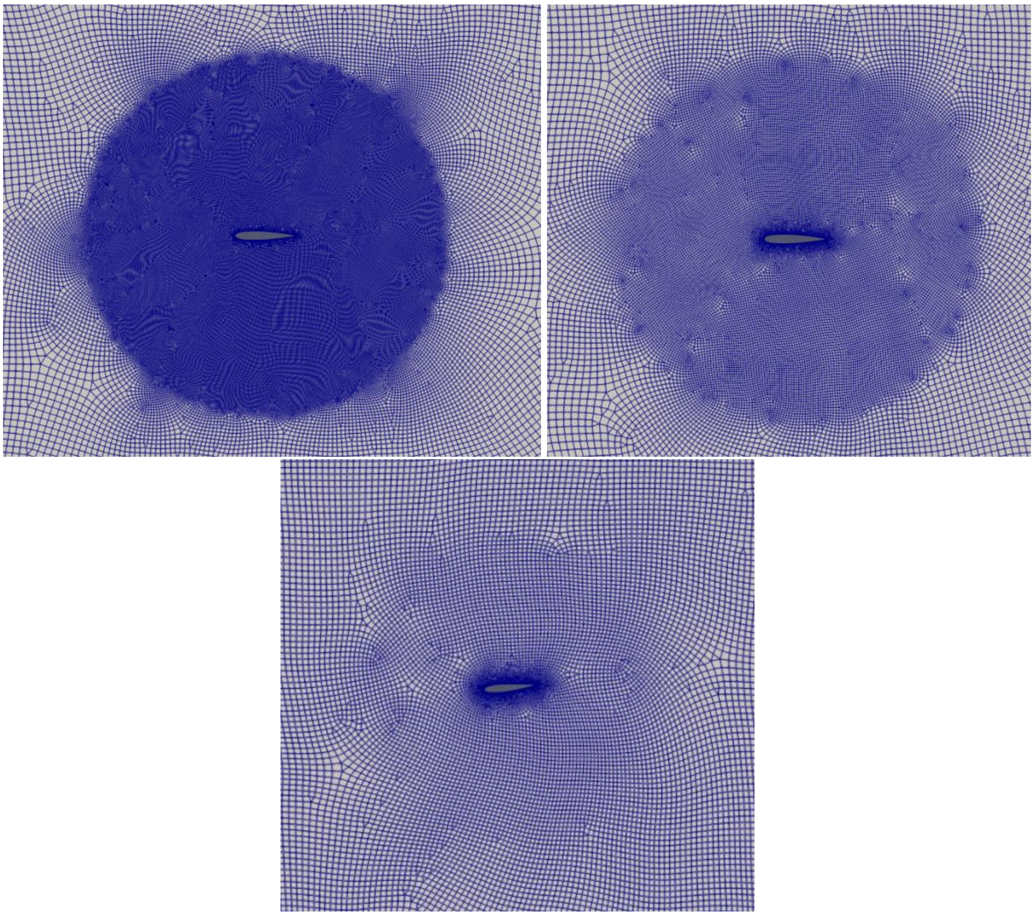

Figure 4.7 Mesh Refinements used: a) Cyl2, b) Cyl4, c) Cyl8

The kinematics results are compared initially. A single time period for the heave and pitch motion is presented in Figure 4.8, where values are non-dimensional. The power coefficients

Cp_y and Cp_θ are also presented in Figure 4.9. The densest case of Cyl2 is used as the reference case. It can be seen that the Cyl4 case is really close to the reference at both kinematics and Power coefficients, and almost matches it. The Cyl8 case though has a larger relative error and is discernible from the other two.

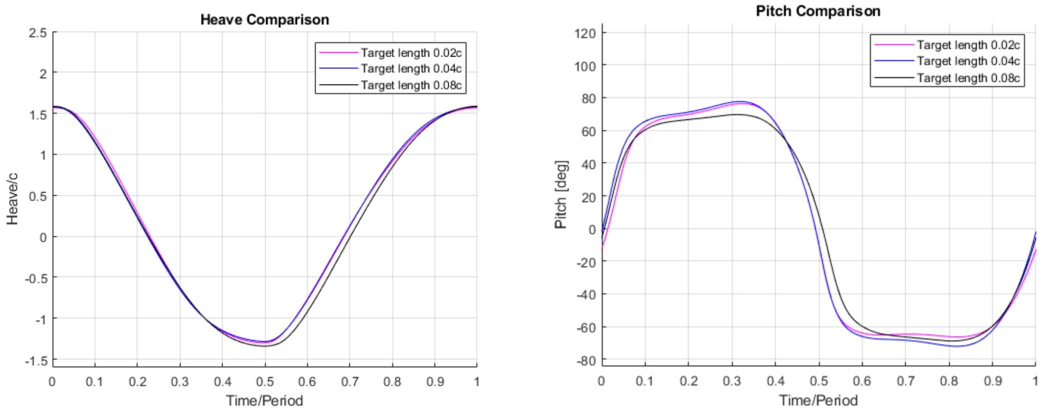

Figure 4.8 Comparison of non-dimensional Heave and Pitch results for a single Period

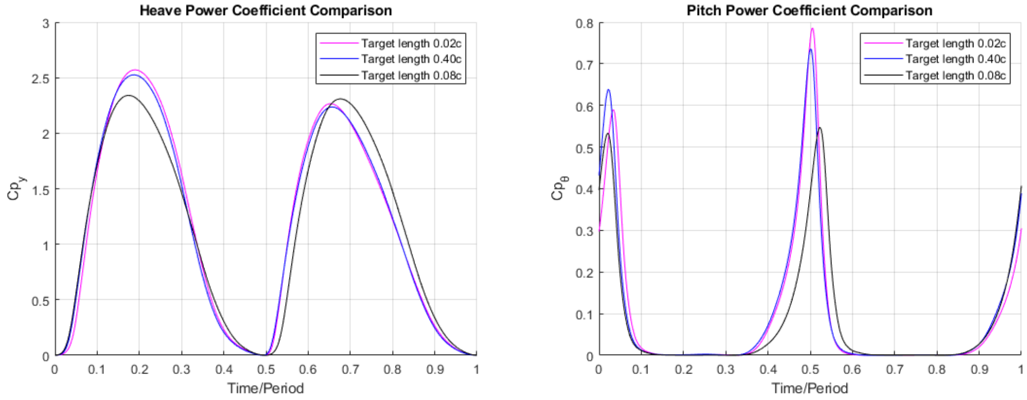

Figure 4.9 a) C_{P_y} and b) C_{P_ϑ} Power Coefficients for a single period

The most important results are the metrics, laid out in Table 3. Using the cyl2 case as the reference, upon which the relative error of the other two can be calculated, it is seen that the relative errors of the other cases are low. The Cyl4 case however, predicts the average power coefficient $\overline{C_p}$, which for this application is, along with the efficiency, the most important metric, much better than Cyl8.

Table 3 Metrics for each case and relative error to the reference case (Cyl2).

Metrics	Cyl2	Cyl4	Cyl4 error	Cyl8	Cyl8 error
h*	1.44	1.41	1.9%	1.46	1.9%
θ*[deg]	71.38	73.35	2.8%	69.26	3.0%
η	34.10%	34.70%	1.8%	33.39%	2.1%
T[s]	0.83	0.81	1.9%	0.85	2.2%
$\overline{C_p}$	1.25	1.25	0.2%	1.22	2.6%

, where h* and θ* are heaving and pitching amplitudes non-dimensionalized by chord length c, η is the efficiency, T is period in seconds.

Results for the Cyl4 and Cyl8 cases are very close to the Cyl2 case, with Cyl4 giving better results especially for $\overline{C_p}$. In order to obtain high quality results and not have needlessly high computational cost, the refinement of Cyl4 is used in the rest of this thesis, which means that the target length of the cells in the circular refinement zone around the foil will be 4% of c.

4.4 Timestep Sensitivity analysis under free surface

Using the grid configuration determined in 4.3, a timestep independence analysis takes place here, to determine a suitable timestep that gives accurate enough results and is not too computationally expensive. Convective time is a suitable measure of time discretization defined as:

$$t_{adv} = \frac{c}{U_\infty}$$

The finest timestep used was $\frac{t_{adv}}{\Delta t} = 1000$ which is used as the reference upon which the relative errors of the other timesteps are compared. Timesteps that were tested are $\frac{t_{adv}}{\Delta t} = 200, 250, 500$. Kinematic results as well as efficiencies and power outputs are compared below.

In Figure 4.10 the kinematic results for heaving and pitching are compared. Zooming in (Figure 4.10 c and d), it becomes clear that the relative error for $\frac{t_{adv}}{\Delta t}$ = 500 almost matches the result of the finest timestep reference case $\frac{t_{adv}}{\Delta t}$ = 1000 thus has the solution has sufficiently converged, while the other two, 200 and 250, have a higher relative error.

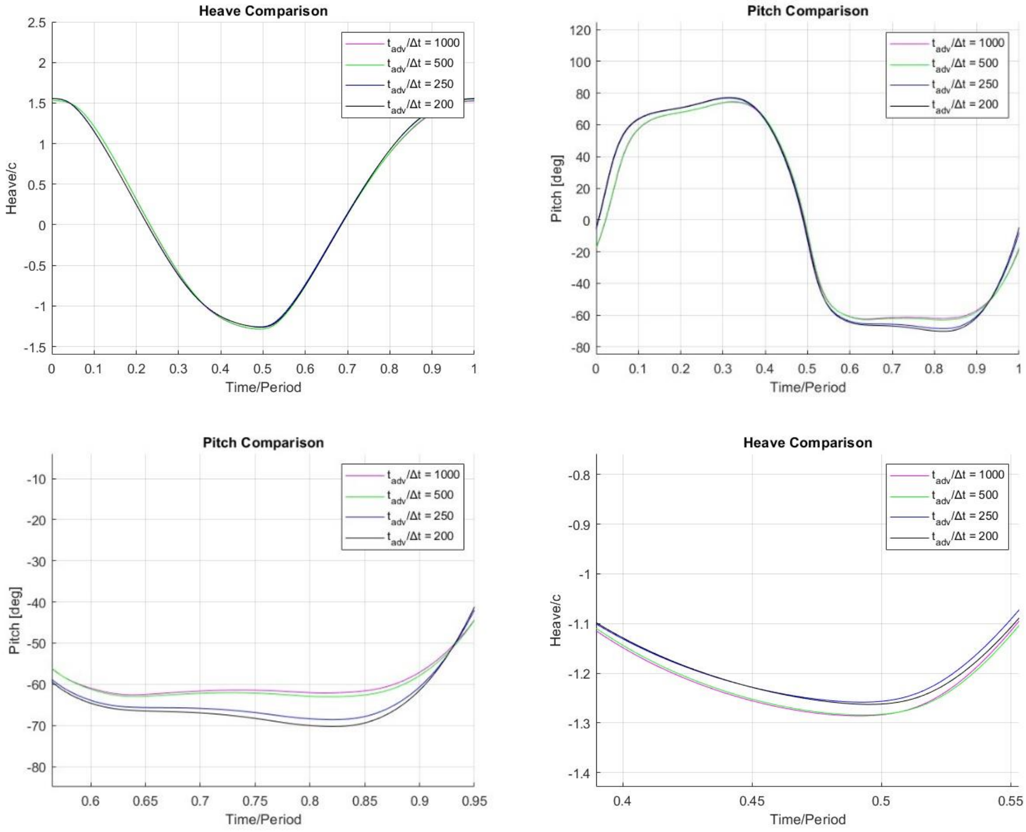

Figure 4.10 a) Heave Motion b) Pitch Motion, c) Heave zoomed in, d) Pitch zoomed in – Comparison between different timesteps.

The power coefficients C_{Py} and $C_{P\theta}$ are also presented. Again, the $\frac{t_{adv}}{\Delta t} = 500$ case is the closest, by a wide margin, to the reference results.

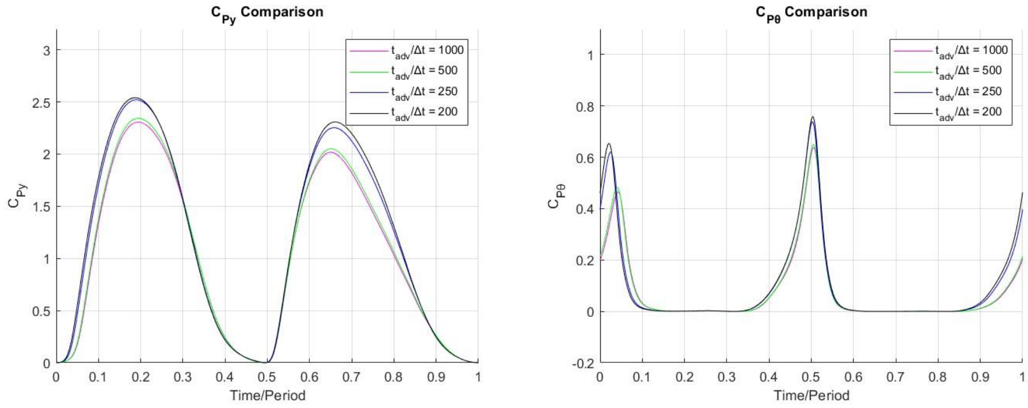

The better quality of $\frac{t_{adv}}{\Delta t}$ = 500 relative to the two lower ones, and its proximity to the reference case, becomes apparent when also considering the motion amplitudes and the harvesting metrics in Table 4. The relative errors for the cases 200 and 250 are quite high, while in the case of 500 very close. This metrics are averaged out across a number of periods, as small difference might alter the results, due to interaction with the wake and the free surface.

Table 4 Metrics for the different timestep cases and relative errors to the reference case.

metrics	1000	500	500 error	250	250 error	200	200 error
heave/c	1.41	1.41	0.0%	1.41	0.1%	1.41	0.1%
pitch[deg]	68.26	68.85	0.9%	72.76	6.6%	73.75	8.1%
efficiency	31.20	31.66	1.5%	34.61	10.9%	35.20	12.8%
period [s]	0.86	0.86	0.5%	0.82	5.7%	0.81	6.6%
$\overline{C_p}$	1.10	1.12	1.6%	1.25	13.3%	1.28	15.8%
Timesteps/period	8,600	4,300		2,150		1,720	

A timestep of $\Delta t = t_{adv}/\ 500$ = 0.0002s is chosen for the rest of the tests in this thesis as it gives good results and is not as computationally expensive as the reference case.

4.5 Verification with experimental results

In order to verify the validity of the simulations for the fully passive foil, results were compared with Duarte's experimental tank test results [31]. The experimental device is presented in Figure 4.11. A NACA0015 foil was designed and tested in a confined channel at a Reynolds number of 60,000. The foil's pitching dynamic parameters k_θ and c_θ could be tuned and thus a parametric space was explored. These tests were also conducted for three different pitching axis locations. The best performance was achieved when the pitching axis was located at 1/3 of the chord, giving a hydraulic efficiency of 31.9%.

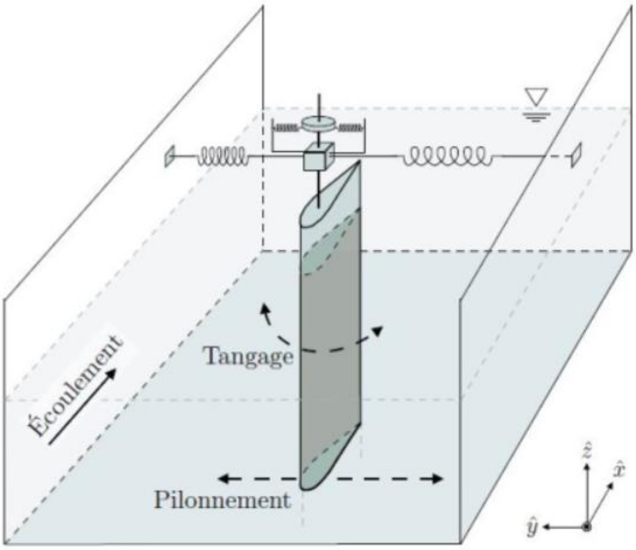

Figure 4.11 Duarte et al - Experimental device inside the towing tank.

The foil was fully passive, and when subjected to uniform flow it performed the desired oscillations, extracting power almost exclusively from its heaving motion. The pitching parameters act more as an aid to position the foil appropriately, so that it can work optimally, thus altering them can largely affect the efficiency and the average power coefficient. The parametric space for the pitching dynamic parameters was explored and was found that the optimal non-dimensional spring stiffness and damping coefficient were $k_\theta^* = 0.071$ and $c_\theta^* = 0.052$. The parameters in their non-dimensional form that are used in this thesis were lifted from Duarte's paper: [31] and are given in Table 2, in section 4.2.

In Duarte's experiment the foil was submerged vertically, so that the free surface does not affect the results. Thus, the problem is solved as a one-phase infinite fluid case, using the grid designed for the two-phase problem but with the air part replaced with water. The foil's refinement zone is the one selected in the Mesh Dependency study in section 4.3. Accordingly, the timestep is the selected one from section 4.4.

Refinement of circular region	4% of c
Time step	$t_{adv}/\Delta t = 500$

First the kinematics results and the power coefficients are compared. In Figure 4.12 the heaving and pitching motion for a single period is compared for the two cases. Table 5 presents a comparison of the average heaving and pitching amplitudes, the efficiency, the average power coefficients and the periods. Finally, Figure 4.13 compares the heaving and pitching power coefficients.

As can be seen, there is sufficient similarity between the numerical results and the experimental ones, which is reassuring and validates the current numerical setup. Table 5 shows that the two significant metrics, efficiency η and average power coefficient $\overline{C_p}$, which are averaged across many periods, are very close to the experimental results. There is also quite good similarity in the kinematics in Figure 4.12. A large difference can be seen in the Pitching Power Coefficient $C_{P\theta}$ in Figure 4.13 but the harvested energy from the pitching motion is much less than that of the heaving motion, thus it plays a small role in the performance of the device.

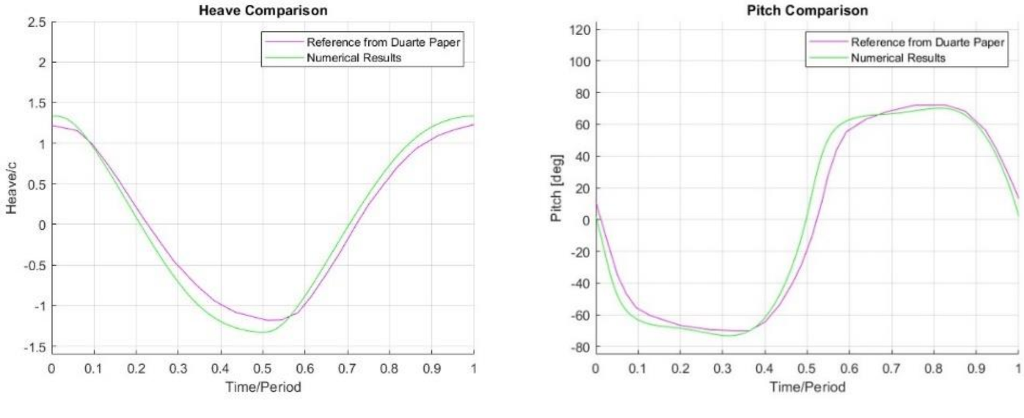

Figure 4.12 Heave and Pitch Motion comparison for a single period.

Table 5 Comparison of Important metrics and relative error.

metrics	Duarte	MaPFlow	error
Ay*	1.36	1.33	2.10%
Aθ*	76.0	71.7	5.98%
$\overline{C_p}$	1.11	1.10	0.81%
η%	31.9	32.0	0.31%
T*	7.63	8.20	6.94%

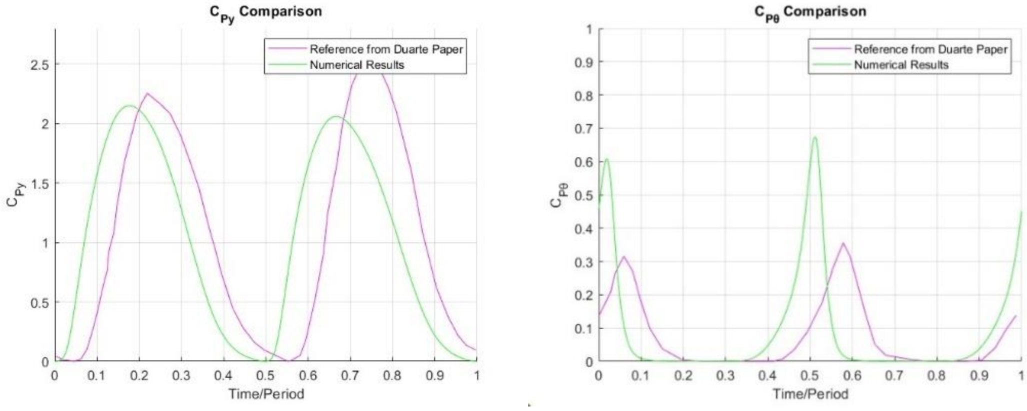

Figure 4.13 Heave (C_{Py}) and Pitch ($C_{P\vartheta}$) Power Coefficient for a single period.

5. Effects of Calm Free Surface

As the application of the device is most likely to be in shallow waters or, in general not submerged deeply below the free surface, its effect on the device's performance needs to be considered. Main predicted practical applications are as a tidal current generator, probably in shallow water, or in a river as a generator, thus definitely in shallow water. This device might also not be grounded on the seabed but suspended from a floating structure, where again it will operate close to the free surface. Thus, it is necessary to study the effect on the performance it will have compared with the unbounded (infinite flow field) case.

When the foil is near the free surface, large amounts of energy are expended from the foil for the surface waves to be created. But the effect is not always negative, as found by [13] and [14], who studied active foils, performing a prescribed sinusoidal motion. A secondary effect that resembles the Bernoulli effect has a positive impact on the performance. As the foil moves upwards, a constriction is created between the foil and the free surface which partly acts as a deformable solid boundary. This results in a velocity increase above the foil and consequently a pressure-drop on its upper boundary, increasing lift. This effect gets more prevalent as the foils approaches the free surface. To sum up, we have at least two conflicting phenomena which complicate the problem and make giving a general answer, in advance, difficult.

[13] and [14] found that performance is decreased for active foils for most cases, but there exists an optimal submergence depth, depending on the Froude number, where the negative effects of the calm free surface are non-existent, or even, the presence of the free surface has a slight positive effect. In this chapter we investigate whether the same applies for fully passive foils.

A parametric study was conducted to explore the effects the free surface has on the performance of the foil. The independent parameters that affect the problem are the structural parameters, the Reynolds number, the Froude number, and the submergence depth of the foil.

The structural parameters for the device are held constant for all the simulations. Their non-dimensional form was given in section 4.2: Table 2 and are used from an optimized device by Leandro Duarte et al. [31] for which experiments were carried out in one phase fluid. This device experiences deep dynamic stall and a large Leading-Edge Vortex (LEV) is formed on its tip assisting its pitching movement.

Reynold's number is also held constant and is the same as in [31]'s experiments: Re = $6 \cdot 10^4$ which is close to that in practical applications.

The main topic of this thesis is to study the effects the submergence depth has on the performance of the fully passive flapping foil device. The submergence depth is defined as the distance between the foil's pitching axis location at equilibrium and the free surface. Multiple submergence depths are examined: S_d = 2, 4, 5, 7 times the chord length. The additional Sd = 3 and 9 were added for the Fr = 1 case. An infinite flowfield case was also implemented for comparison.

Froude number is also varied. The Froude number is defined as the ratio of inertial to gravitational forces, thus the disturbance of the free surface varies based on the Froude number, which, in effect, changes its influence on the flapping foil. When the Froude number is low, the free surface is disturbed less. Each submergence depth was tested on Fr = 0.8, 1, 1.25 and 1.5.

5.1 Effects of Submergence Depth for various Froude Numbers.

The effects of varying the submergence depth for a series of Froude Numbers is examined in this section. The performance of the foil for each test is assessed using two metrics, efficiency η and average power coefficient $\overline{C_p}$. In Figure 5.1 and Figure 5.2 the results for all the cases examined are presented. η-S_d and $\overline{C_p} - S_d$ curves for constant Froude numbers are presented. The horizontal red line represents the unbounded case, as a comparison to the other cases. As a general trend, we notice that for low submergence depths, below Sd = 3, performance drops rapidly as the foil is very close to the free surface. For intermediate depths, a peak appears for all the Froude numbers, where η and $\overline{C_p}$ are as high or even higher than the unbounded case. Increasing depth further, performance drops again, and then it approaches the unbounded case for very high depths, as the effect of the free surface diminishes.

These results show that there exists an optimal submergence depth, where the calm free surface does not decrease performance relative to the infinite flowfield, or it even increases it slightly. This depth however seems to depend on the Fr number, as for Fr = 0.8 the peak happens for lower S_d. Froude number, in general seems to affect performance, but the same general trends appear for every Fr: performance drop for low depth, a peak forms at intermediate depths and the performance approaches the unbounded case for high depths. In order to study the effect of Submergence depth we can thus isolate the cases for a selected Fr.

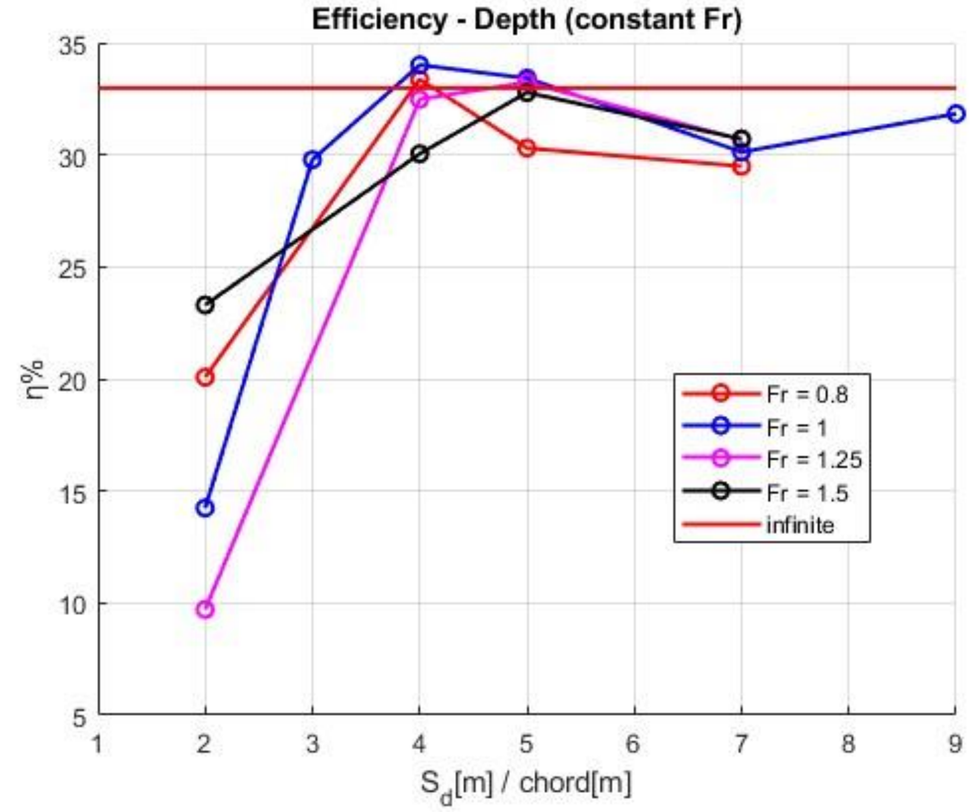

Figure 5.1 Efficiency curves for various Submergence Depths, for constant Fr numbers = 0.8, 1, 1.25, 1.5 (compared to the infinite flowfield case: red horizontal line)

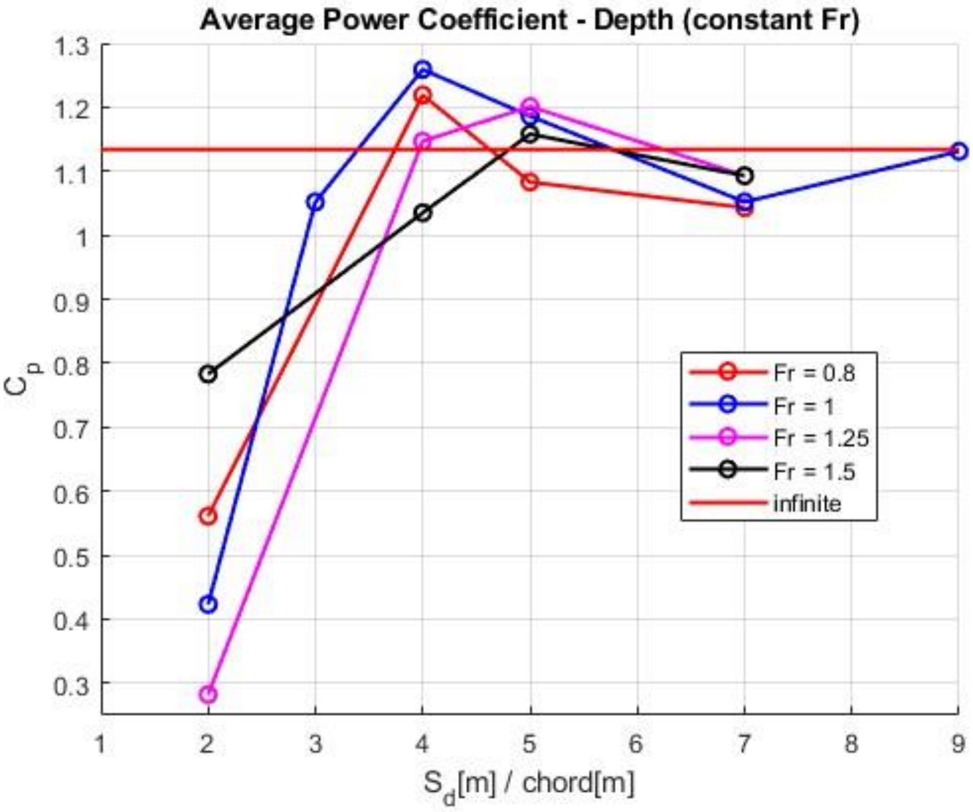

Figure 5.2 Average Power Coefficient curves for various Submergence Depths, for constant Fr numbers = 0.8, 1, 1.25, 1.5 (compared to the infinite flowfield case: red horizontal line)

5.2 Effects of Submergence Depth for Fr = 1

To better understand the results and the underlying fluid mechanics phenomena that cause them, the results for Fr = 1 are examined in detail. This Froude number was examined for many submergence depths, so the general trends are more obvious. In Figure 5.3 the efficiency-depth and in Figure 5.4 $\overline{C_p}$-depth plots are presented. The horizontal line represents the results for the unbounded case. The depths examined for the specific Froude are S_d = 2,3,4,5,7 and 9 chord lengths.

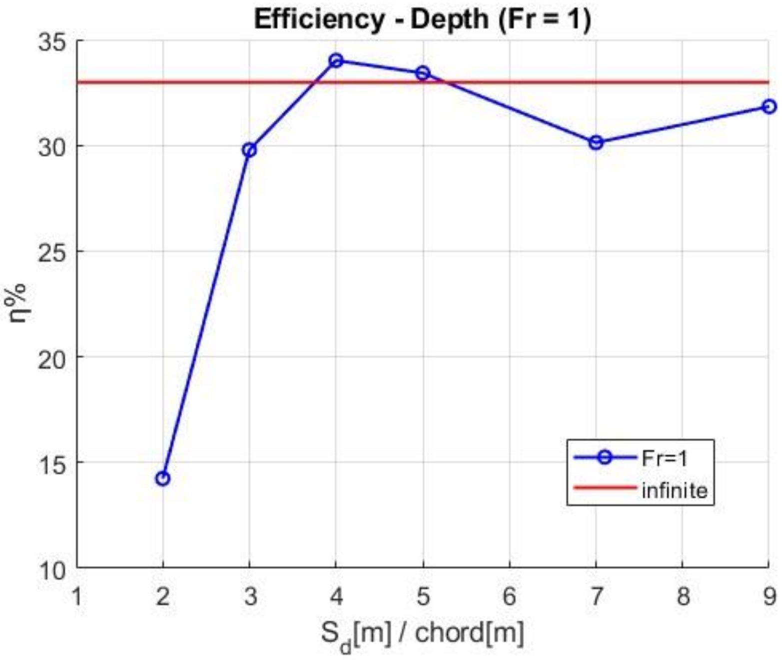

Figure 5.3 Fr = 1: Efficiency for various Submergence depths

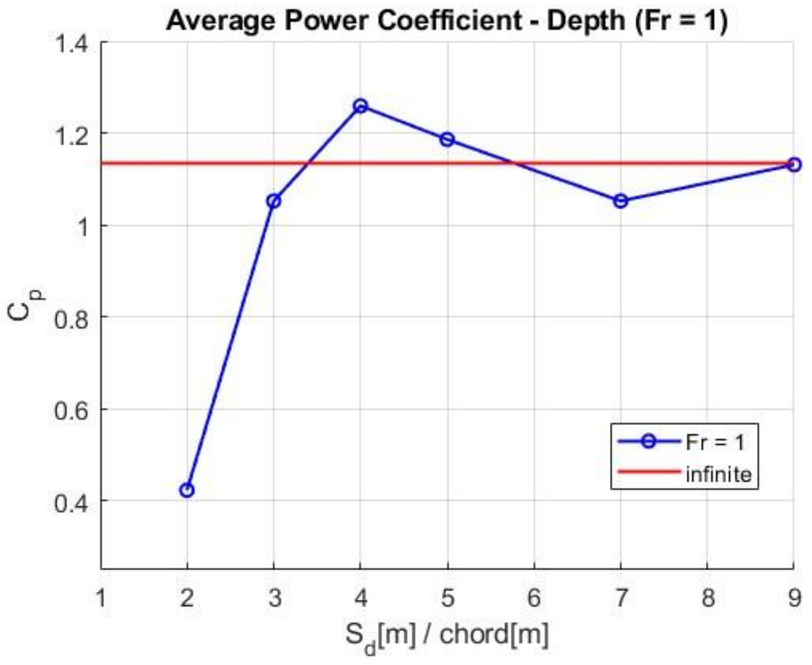

Figure 5.4 Fr = 1: Average Power Coefficient for various Submergence Depths

The results are averaged across many periods. Periodicity of the movement is very good for large submergence depths but not so much for low ones, as position of the waves formed in the free surface from previous periods affects the motion. Consequently, the foil is affected differently from the free surface during each period. This is seen in Figure 5.5 where the non-dimensional heave position is compared for two different cases, S_d = 2 chord lengths and unbounded. The horizontal blue line aids in seeing the difference in amplitudes for each period.

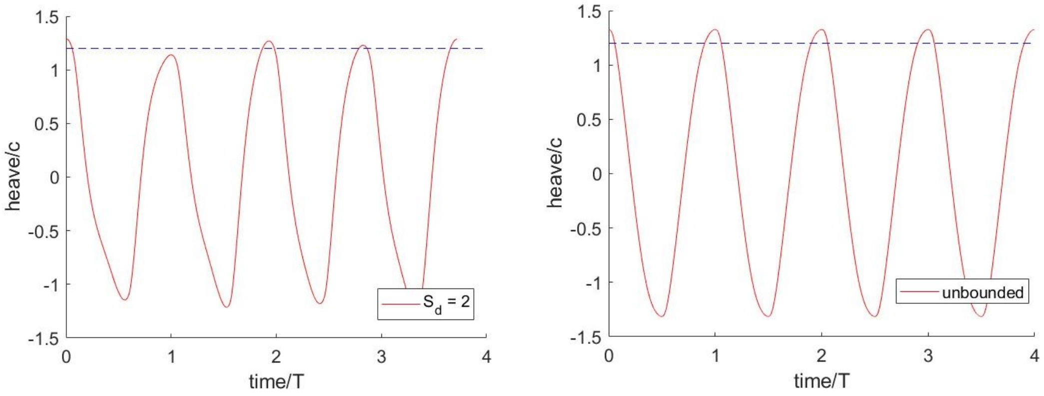

Figure 5.5 Variance of Heave Amplitude per period for low depth versus infinite case.

The main metrics for each submergence depth, for Fr = 1 are presented in Table 6, , where h* and θ* are heaving and pitching amplitudes (heave is non-dimensionalized by chord length c and θ* is in degrees), η is the efficiency, T* is non dimensional period and $\overline{C_p}$ is the average power coefficient of the device.

Table 6 Fr = 1: Main Metrics for Various Submergence Depths.

metrics\Sd	2	3	4	5	7	9	infinite
h*	1.26	1.45	1.44	1.40	1.40	1.41	1.32
θ*(°)	47.7	66.3	71.8	70.7	65.7	67.9	72.2
η	14.3%	29.7%	34.0%	33.4%	30.1%	31.8%	33.0%
T*	12.6	9.0	8.3	8.4	8.9	8.6	8.1
$\overline{C_p}$	0.423	1.063	1.260	1.186	1.052	1.131	1.134

As can be seen from the results presented thus far, the influence of the free surface is not straightforward. Efficiency and Power Coefficient have similar trends through the submergence depths. For high depths, such as S_d = 7 and 9 the presence of the free surface slightly reduces the performance of the device. The influence is small as for high depths the infinite flowfield case is approached, as expected. For very low depths close to S_d = 2 the performance reduces rapidly. The foil is very close to the free surface and thus large amounts of energy are expended for the formation of these waves. Other reasons, relating to the creation of a Leading-Edge vortex affect the performance, and are discussed later in this section.

In Figure 5.6 and Figure 5.7 the heaving and pitching motions, for a single period, for indicative cases are presented. The heaving amplitude is not significantly affected when the foil is at low depths. The pitching amplitude, in contrast, is significantly decreased. This is explained from the behavior of the LEV presented later in this section. In Figure 5.8 the non-dimensional period T*-S_d curve for Fr = 1 is presented. Period is increased by a lot for the low depth case. This explains the large drop in performance, as this means that despite the heaving amplitude being the same as in the good performance cases, period increases, which means that the foil velocity is decreased, thus the energy the generator harvests, which is proportional to the square of the velocity, is decreased. For intermediate depths, such as S_d = 4 and 5, a peak forms, and performance is either very close or even higher than the reference unbounded case. This is rather interesting, and the reasons will also be thoroughly explained in this chapter.

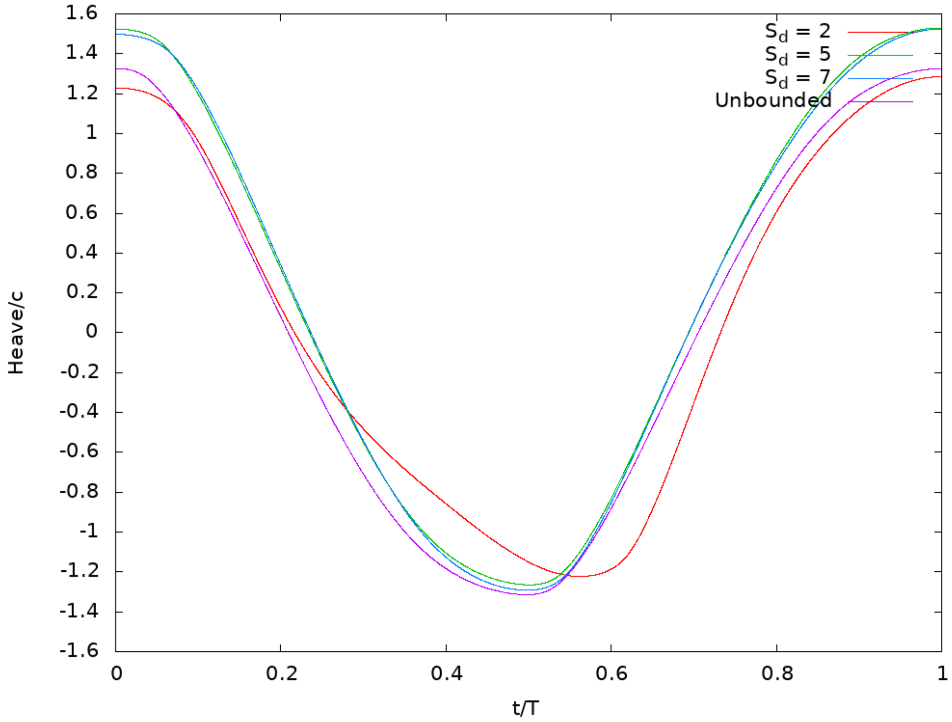

Figure 5.6 h for a single period for different S_ds*

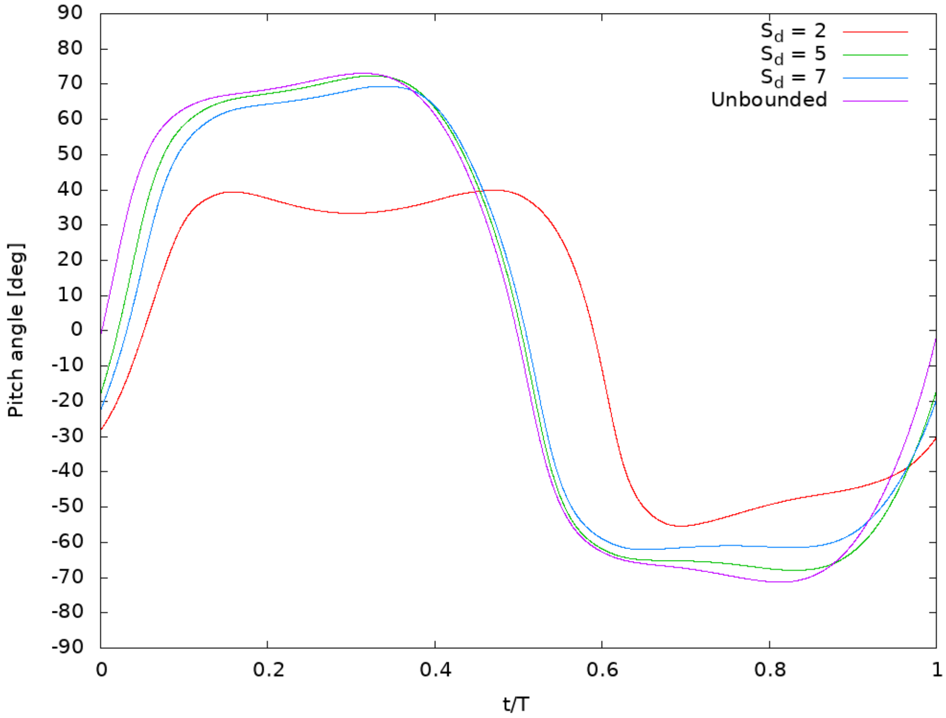

Figure 5.7 ϑ for a single period for different S_ds*

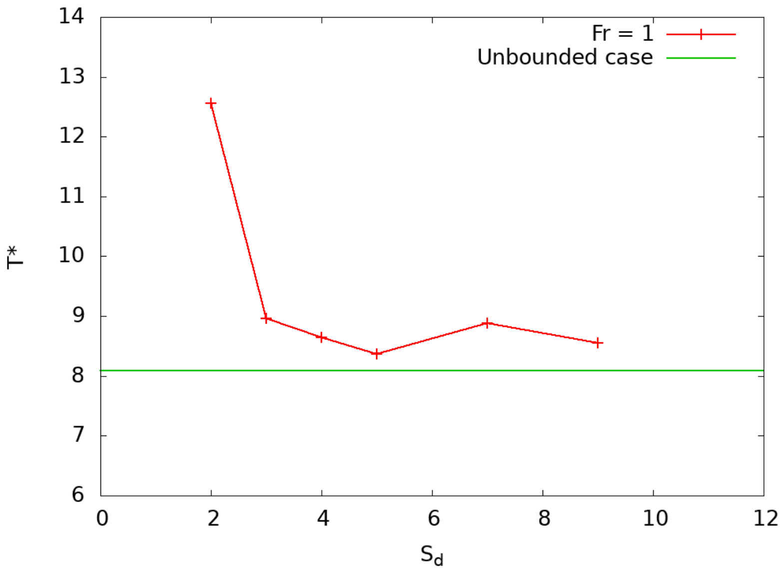

Figure 5.8 T for different S_d relative to the infinite case.*

Depletion of energy in waves

One way the free surface affects the performance of the flapping foil is energy transfer from the foil that goes into the creation of gravity waves. This effect is negative for the performance of the foil. As the foil approaches the surface, bigger and bigger disturbances to the free surface occur, which means that more energy get transferred. In essence, the pressure differences that the foil creates lend part of their energy to the creation of waves and aren't applied as loads on the foil. Figure 5.9 shows the locus of the free surface for various depths, when the foil is at its uppermost position, for a length that begins -8c from the L.E. (upstream) to 8c (downstream). As expected, the disturbances are quite larger for low depths, reaching wave amplitudes up to 0.2c, which requires larger amounts of energy. The disturbance, however, is also very significant when $S_d = 4$, but performance at these depths is close to the unbounded case. This signifies that disturbance is not the only factor affecting performance. Free surface disturbance is also visualized by the density plot in Figure 5.10, comparing $S_d = 2$ with $S_d = 5$ when the foil is at its uppermost position, where the disturbance in the low depth case is particularly high, especially for the $S_d = 2$ case.

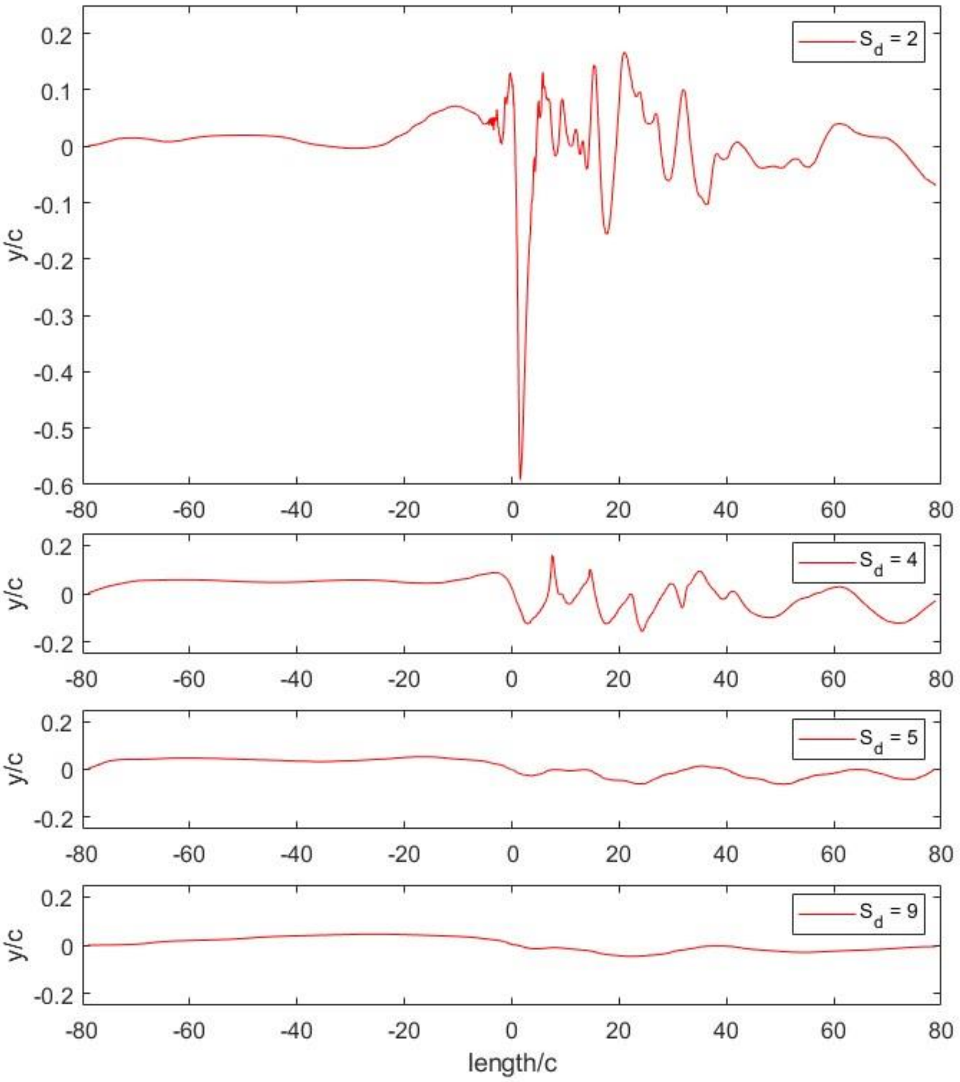

Figure 5.9 The locus of the free surface from -80c to 80c (foil L.E. is at 0), for different S_d*s*

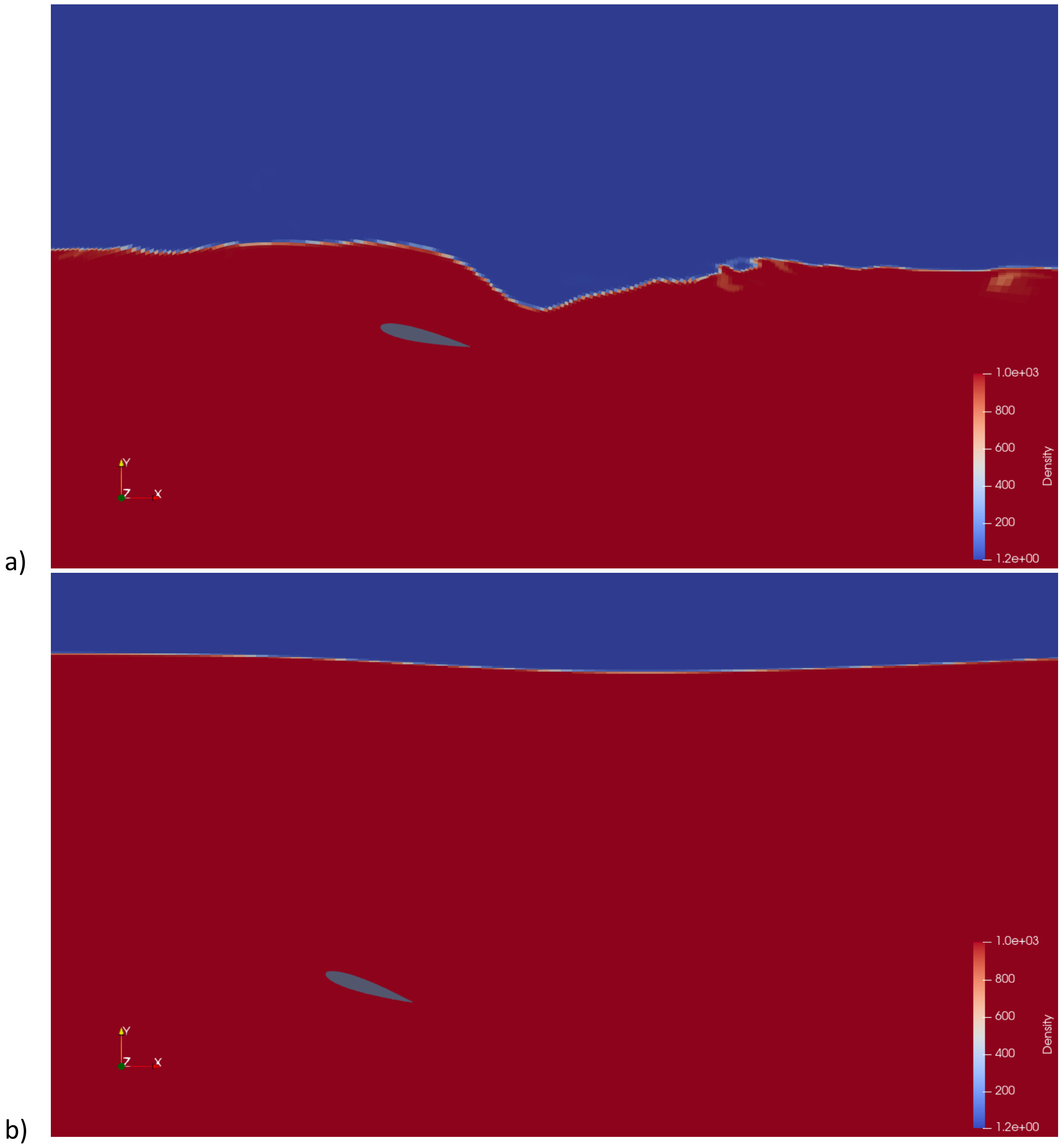

Figure 5.10 Free surface visualization for a) S_d = 2 and b) S_d = 4.

Bernoulli Effect

The second significant effect is caused due the constriction between the foil and the free surface. The free surface acts as a deformable boundary, as gravity restricts its deformation. Its influence is not as major as that of a rigid surface, but flow is indeed partly constricted. The magnitude of the deformations for each S_d is also affected by the Fr number, as for lower Fr numbers, the ratio of gravity forces to inertial forces becomes more significant and this makes the free-surface less deformable. For constant Froude number, the effect is amplified as the S_d lowers, because the flow on the upper part of the foil gets more constricted. As a result, flow velocities rise more in these cases. Due to the well-known Bernoulli effect, the increased velocities in the streamlines on the upper part of the foil result in a pressure drop. This velocity increase is depicted in Figure 5.12 below, where the velocity distribution along a vertical line above the foil (Figure 5.11), for the unbounded and S_d = 5 case, show an increase when the free surface is present.

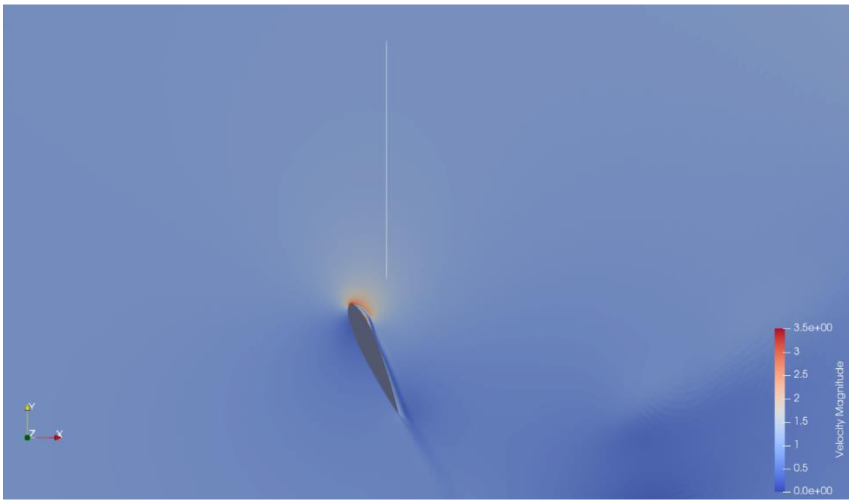

Figure 5.11 Line upon which velocities were measured, at this position of the foil.

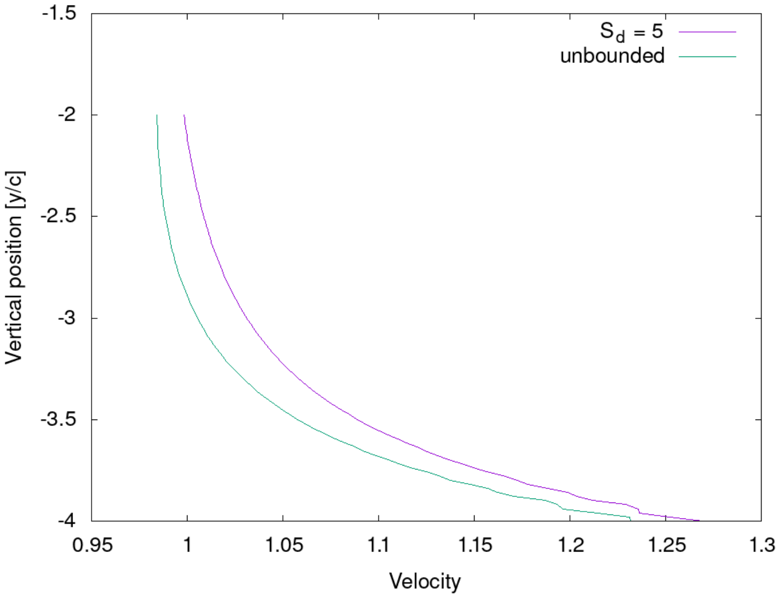

Figure 5.12 Velocity distribution along a vertical line above the foil.

This Bernoulli effect is beneficial for energy extraction. As the foil heaves upwards, pressure is decreased on its upper side compared to the unbounded case, causing the lift force to increase. This means that more energy is harvested from the device. However, when the foil moves downwards, this effect is reversed, as lift is decreased compared to the unbounded case. This is illustrated in Figure 5.13 for a single period, where the unbounded case Lift Coefficient is contrasted to that of the S_d = 5 case. In the first half-period, the magnitude of lift is less but in the second half it is greater. However, the increase in the absolute value of the Lift on the second half of the period (upstroke) is greater than the decrease on the first half (downstroke), which explains why it has a net positive effect on the foil's performance.

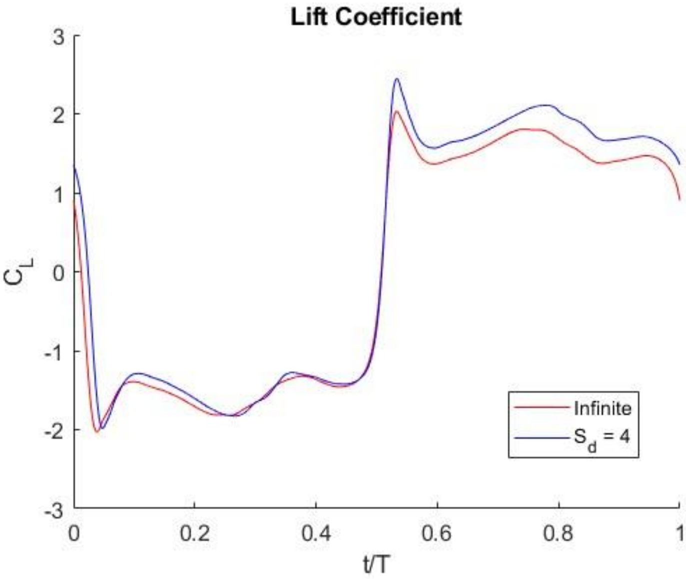

Figure 5.13 Lift Coefficient (C_L) comparison for a single period.

Energy harvesting, however, is not only increased in the upstroke, where Lift is increased, but on the downstroke also. The harvester, being an electrical generator, which behaves like a damper, extracts power equal to $c_Y\dot{y}^2$. The increased Lift during the upstroke, increases the amplitude of the heaving motion, as depicted in Figure 5.14 (while it is slightly lower on the downstroke). Consequently, the foil's speed is increased during the downstroke, increasing power extraction, despite having a lower lift force. Figure 5.15 depicts the heaving power coefficient, where it is evident that power extraction is increased for S_d = 5, mostly during the downstroke (first half of the period), but also during the upstroke (second half).

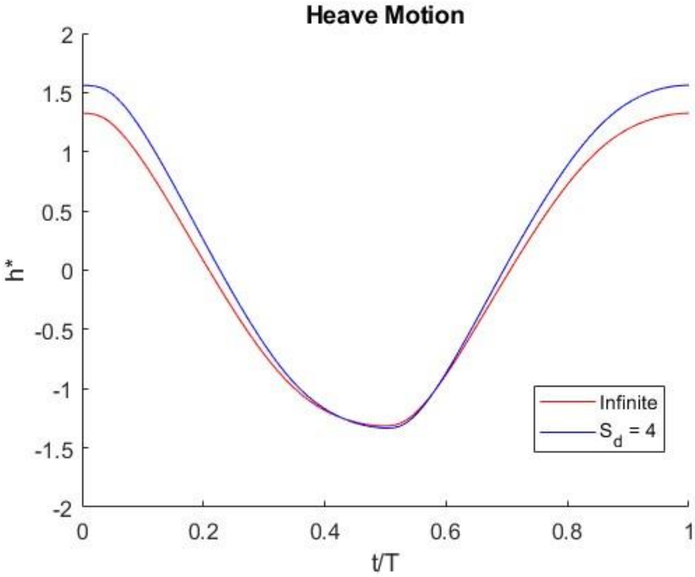

Figure 5.14 h(t*) comparison for S_d = 5 and infinite case.*

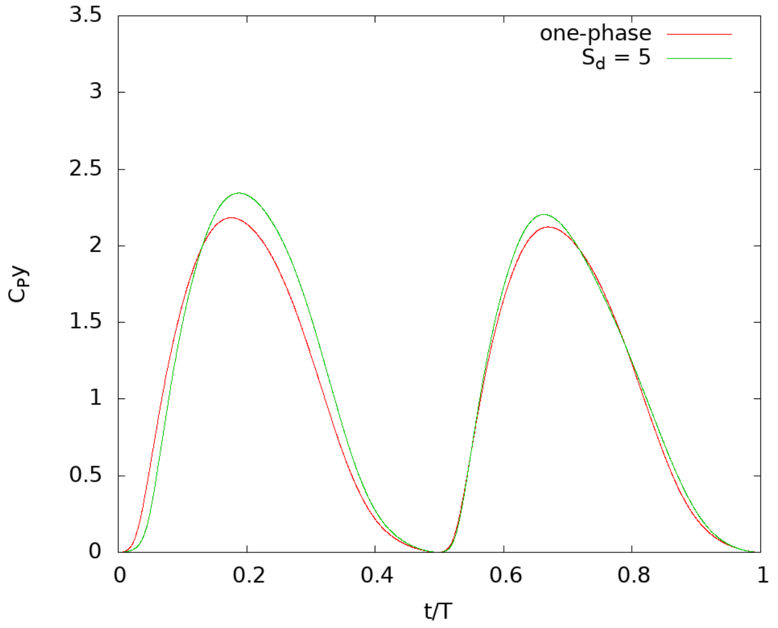

Figure 5.15 $C_{Py}(t^*)$ comparison for $S_d = 5$ and infinite case.

Energy extraction from the pitching motion is much less than that of the heaving motion, and it does not differ significantly between these cases. In Figure 5.16 the pitching Power Coefficient (C_{Pp}) differs only in the uppermost position, where energy extraction is slightly higher for the one-phase case. This is due to the effect of the Leading-Edge Vortex, which aids more in pitching when the foil isn't close to the free surface, as is described later in this section.

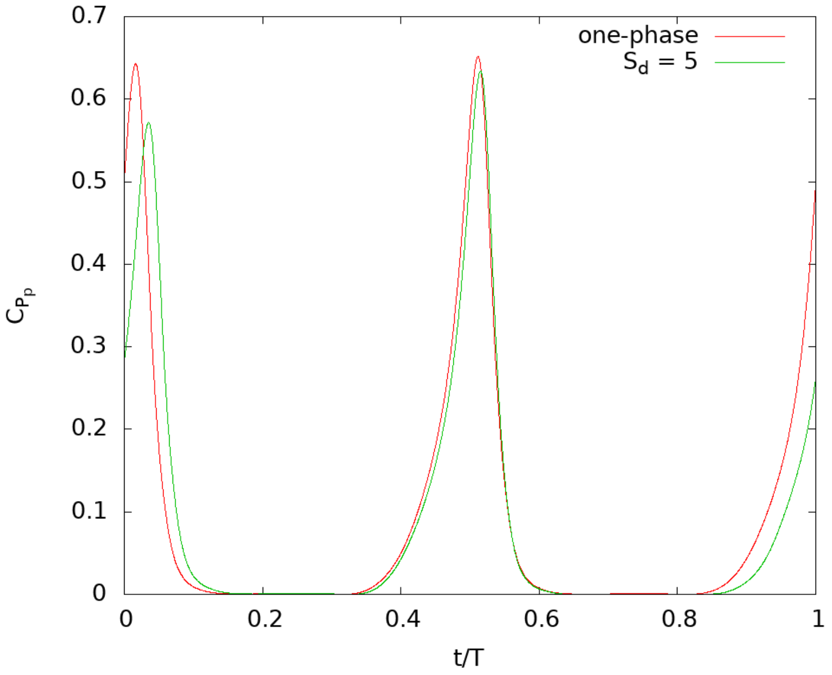

Figure 5.16 $C_{Pp}(t^*)$ comparison for $S_d = 5$ and infinite case

The influence of this Bernoulli effect explains the peak in the performance seen in the efficiency (η) and average power coefficient $(\overline{C_p})$ diagrams in Figure 5.3 and Figure 5.4. Although this effect is even more prevalent in lower depths, the other effects start playing a much more significant role and performance drops rapidly.

Motion Synchronization

Synchronization of the heaving and pitching motion is very important in the search of structural parameters in order to achieve good performance. This device is not active, meaning that the motion is not prescribed, so the motion cannot be explicitly set. In essence, the pitching motion is responsible for the suitable positioning of the foil, so that the maximum amount of power can be harvested by the heaving motion. When the foil is not well synchronized, large amounts of energy can be lost. If, for example, the foil is at the beginning of the downstroke (at its uppermost position), but the foil has not yet pitched forward to reverse its angle with the flow, the Lift force will be opposed to the movement of the foil, and energy will be imparted to the flow from the device.

The pitching motion is heavily affected by the choice of structural parameters. Most importantly, the choice of these parameters affects the formation and shedding of a Leading Edge Vortex (LEV). As described by [33], a large LEV is formed close to the Leading Edge of the foil, as the foil goes through dynamic stall, which is detached when certain conditions are met. The vorticity of the flow during an upstroke for the S_d = 5 case is shown in Figure 5.17. This LEV, which constitutes a low-pressure region, is then convected downstream along the upper surface of the body. Figure 5.18 shows the pressure contour of the flow when the foil is at various positions during the cycle where we can see that the vortex is an area of large pressure drop. This large LEV is formed as the foil goes through dynamic stall. When it gets detached, and reaches the trailing edge, it helps decrease and finally reverse the angle, so that the downstroke begins. This mechanism determines the pitching motion and as such it affects synchronization. Figure 5.18 (b) shows the corresponding Cp plot at T/9, where it is seen that a much lower pressure acts on the foil where the LEV is located, where the vortex is located. Consequently, when the vortex is after the pitching axis and close to the Trailing Edge of the foil, a large torque acts on it, which causes it to pitch forward, switching the foil's angle with the flow.

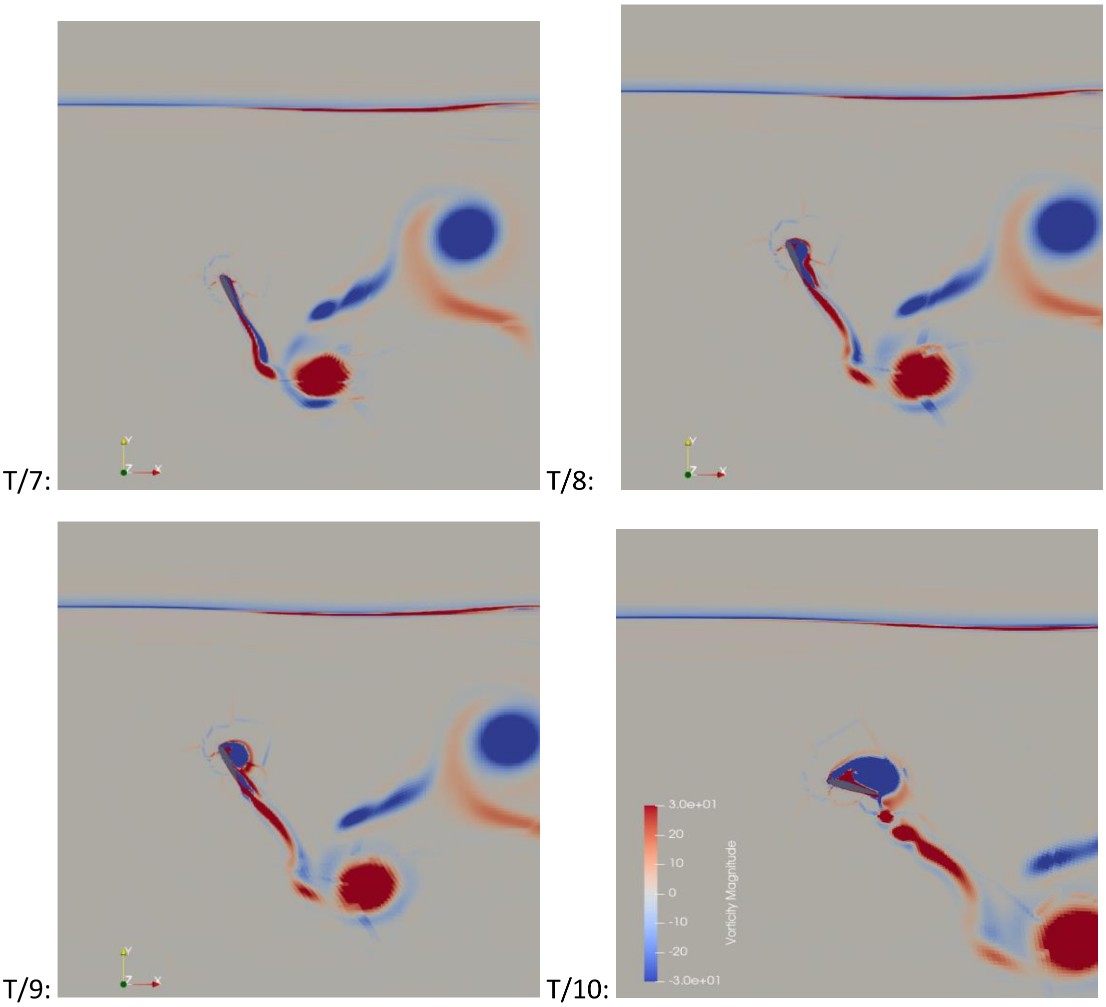

T/7:

T/8:

T/9:

T/10:

Figure 5.17 Vorticity contours for successive positions of the foil during the upstroke.

(a)

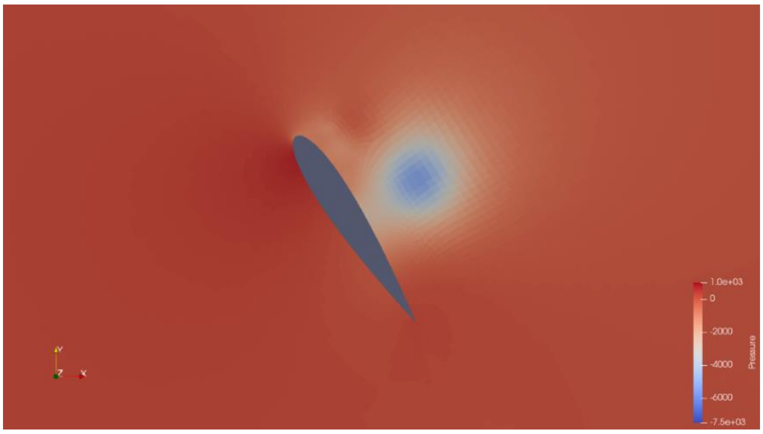

(b)

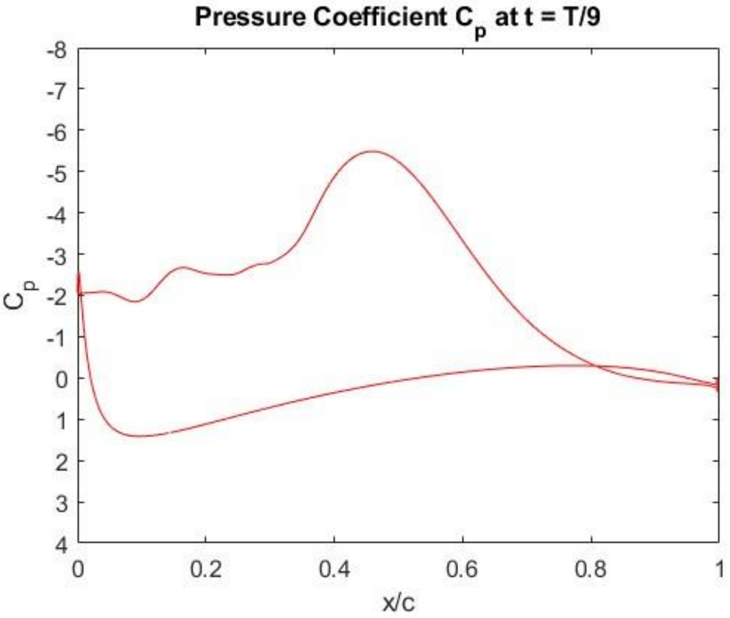

Figure 5.18 Pressure contour at T/9 (a) and the corresponding Cp plot (b)

The structural parameters for the tests in this thesis were chosen from an experimental parametric study by Duarte et al [31], where k_θ and c_θ values were explored. For a given choice of the rest of the parameters, optimal performance was achieved with the same values of k_θ and c_θ as the ones used in this thesis. In order to understand how this optimal performance is affected by the free surface, its influence on the synchronization should be assessed.

As this is a passive foil, and the motion is not sinusoidal, a different way must be found to assess the synchronization of the two motions. Fourier analysis was conducted, for this reason, to the phase difference between the heaving and pitching motions and these we compared that to the “well-synchronized” unbounded case. The heave and pitch position timeseries were analyzed and their corresponding phases were subtracted in order to find their phase difference. This is then subtracted from the 90° phase difference that is common for prescribed motion flapping foils. Results are presented in Table 7 and Figure 5.19.

Table 7 Phase difference between heave and pitch motion.

Sd	infinite	9	7	5	4	3	2
Phase Difference [deg]	104.1°	104.8°	107.1°	104.6°	105.8°	108.5°	117.7°
Difference from prescribed [deg]	14.1°	14.8°	17.1°	14.6°	15.8°	18.5°	27.7°

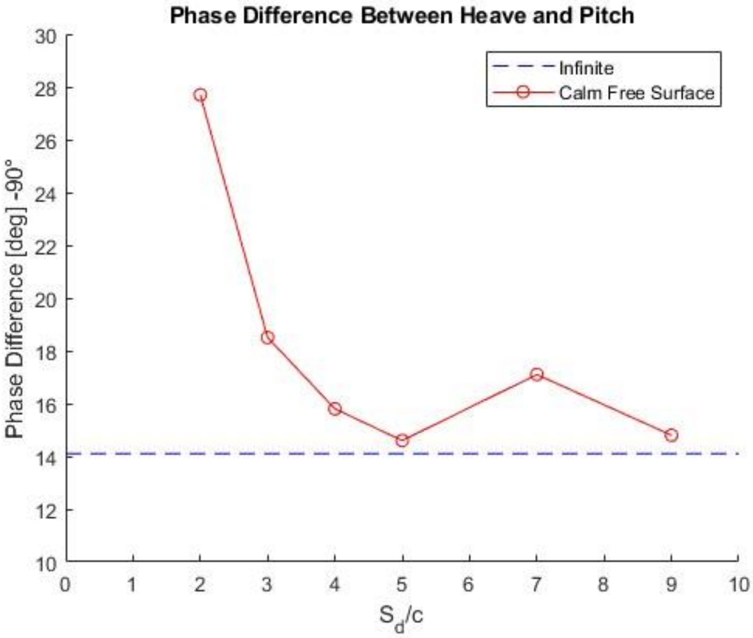

Figure 5.19 Heave and Pitch Phase difference (-90) for various depths (Fr = 1)

These results inversely correlate very well with the results for the performance (η and $\overline{Cp}$) of the foil. For submergence depths where the peak in performance was present (S_d = 4 and 5), phase difference is close to the unbounded case. For S_d = 7 phase difference is larger, and performance drops. For low depths (S_d = 2 and 3) phase difference becomes much larger as performance gets drops rapidly. This shows that when the foil is located very close to the free surface, the synchronization is negatively affected. The numerical results produced, show that the shedding of the LEV lags behind the unbounded case when the foil is under a calm free surface, and as a consequence, pitching is also delayed and performance falls.

The cause of this delay in the shedding of the vortices when the foil is close to the free surface is best described by [34], where the flow past a submerged cylinder located in various depths from the free surface, in low Reynolds number flow is examined numerically. Specifically, the Strouhal number of the vortex shedding phenomenon, f (defined as St = f·u/d, where d is the diameter of the cylinder, and f the shedding frequency) is measured for various Submergence depths and Froude numbers. The diagram in Figure 5.20 was then constructed which shows a similar lag in shedding as the gap ratio (submergence depth) is lowered.

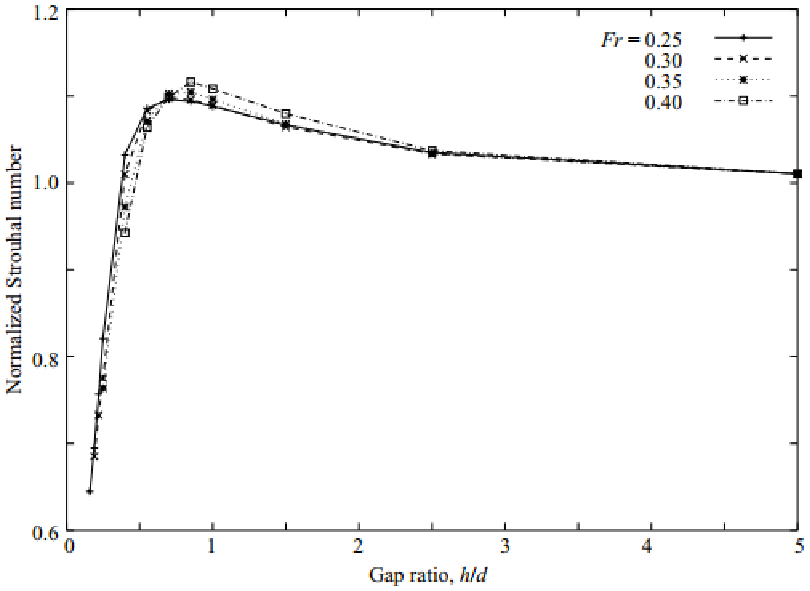

Figure 5.20 Diagram by [34] presenting the drop shedding Strouhal number as Submergence Depth drops.

The Normalized Strouhal number is defined as St/St_0 where St_0 is the Strouhal number in the case of unbounded flow. The Gap ratio is the ratio of the distance of the top of the cylinder from the free surface divided by the diameter of the cylinder.

It is clear that there is a large reduction in the frequency of the vortex shedding when the gap ratio falls below approximately 0.6. As suggested by Green et al [35], the frequency of the vortex shedding is determined by the time taken for sufficient vorticity to accumulate outside a region of high shear stress. [34] suggested that for this case, the supply of fluid is partially constricted by the presence of the free surface, and this increases the time required for fluid to accumulate in the region where the vortex is formed. This hypothesis was also validated by processing the results, where it is shown that the supply of fluid in the region above the cylinder is reduced and follows the same pattern as the Strouhal number.

This can also explain why there is a significant delay in the vortex shedding for the flapping foil, when it is located close to the free surface, causing it to become unsynchronized, and its performance to drop so rapidly. As is the case for submerged cylinders, the reduction in the supply of fluid delays the accumulation of sufficient vorticity, which allows the vortex to stay attached longer. In effect, the torque required for the foil to pitch is forestalled in relation to the optimized initial case.

Resonance

The heaving motion is responsible for the bulk of the energy harvested from the incoming flow. Increasing the amplitude of the heaving motion would increase the performance. As this is an oscillating system, synchronization between the loads applied and the natural frequency of the system would result in increased amplitude. The resonance in the heaving motion is examined below, along with its impact on the foil's performance for each case of submergence depth. A Fourier analysis was done for the heaving velocity timeseries $\dot{y}(t)$, as velocity is directly related to the amount of harvested power and the coefficients η and C_p. The predominant frequency is then compared to the natural frequency of the heave motion. The undamped natural frequency is:

$$\omega_n = \sqrt{\left(\frac{k_y}{m_y}\right)} = 8.85 \text{ rad/s}$$

$$f_n = 1.41\ Hz$$

However, as this is a damped system, the natural frequency is reduced, so the system will oscillate freely with a new damped natural frequency which depends on the damping ratio ζ:

$$\zeta = \frac{c_y}{2\sqrt{m\, k_y}}$$

$$\omega_d = \omega_n\sqrt{1-\zeta^2} = 7.26\ rad/s$$

$$f_d = 1.16\ Hz$$

The frequency – Power Spectral Density (PSD) diagrams of the Fourier Analysis are presented in Figure 5.21.

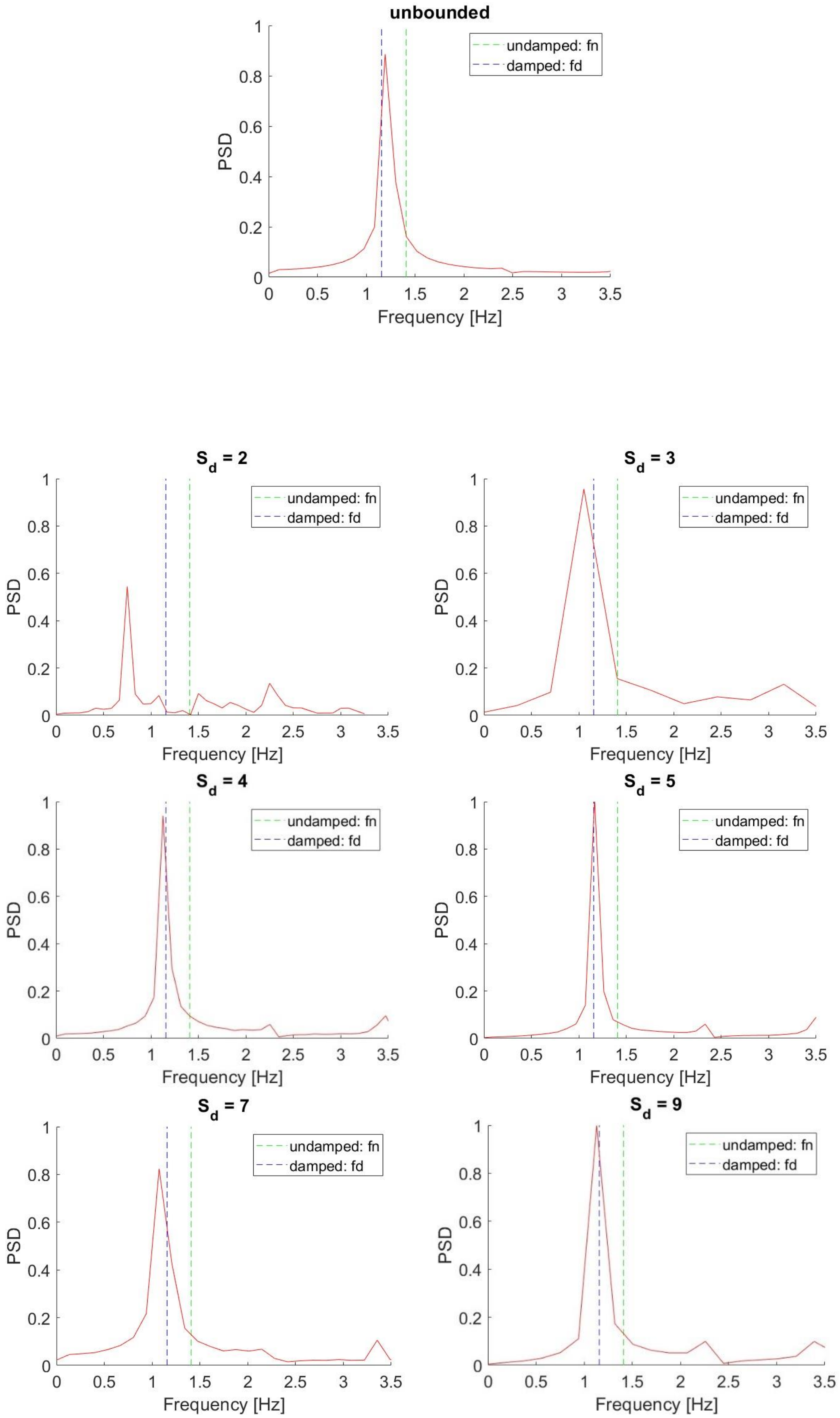

Figure 5.21 Power Spectral Density-f(Hz) diagrams from Fourier analysis of the $\dot{y}$ timeseries for different depths.

The results of the Fourier analysis indicate that good performance is correlated with the frequency of the heaving motion and its proximity to the damped natural frequency. For submergence depths S_d = 4, 5 and 9, where performance is high, the corresponding peaks in the diagrams almost match the natural frequency of the damped system f_d. In contrast, for S_d = 7 there is a slight difference, as performance is also slightly lower. As for the case S_d = 3 and especially for S_d = 2, the frequency drops by a very significant amount due to the reduced loads close to the free surface, so that the absence of resonance causes the large performance drop. It can be deduced that although the device can be well-tuned, so that resonance occurs, close to the free surface this is ruined as the oscillating frequency drops rapidly.

Reduction in LEV strength and Dynamic Stalling

The pressure contours for the unbounded case (left) and the S_d = 2 case are presented in Figure 5.22. Four plots for each case are provided for t = T/7, T/8, T/9 and T, when the foil performs an upstroke, and the production and shedding of the LEV is visible. It is evident that for the S_d = 2 case, the pressure drop on the L.E. of the foil and inside the LEV is reduced substantially. This is explained as the pressure drop created by the foil is wasted in disturbing the free surface and its energy is imparted to the creation of waves.

Despite the flow stalling around the foil in the infinite flowfield case much more than the Sd = 2 case where the angle is much smaller, lift is higher in the former. The pressure coefficient Cp in Figure 5.23 is provided at t = T/7, for each case. It is seen there that despite the flow separation, there exists a small area at the upper surface, close to the L.E. where the pressure drop is very large. This is explained by [4] who performed experiments on foils undergoing dynamic stall. It was observed that due to the upward motion, there exists a small area close to the L.E. of the foil where the flow remains attached even when the angle of attack is much higher than the static stall limit. This explains the very large pressure drop and large increase in lift. Dynamic stalling is, of course, temporary, as the deceleration at the top position causes the flow to detach completely and, therefore, a very severe loss of lift.

The diminished pressure drop, as a consequence, has a large effect to the pitching of the foil, as less torque is applied to it. This explains the large reduction in pitching amplitude for S_d = 2, in the pitch timeseries (Figure 5.7). The reduction in the pitch angle, consequently, reduces the lift force applied on the foil by the surrounding fluid. In cases where the foil is static, larger pitch angles would This in turn reduces the foil's velocity, and thus, the harvested power from the generator. The effect of the LEV is highlighted through this effect in addition to synchronization.

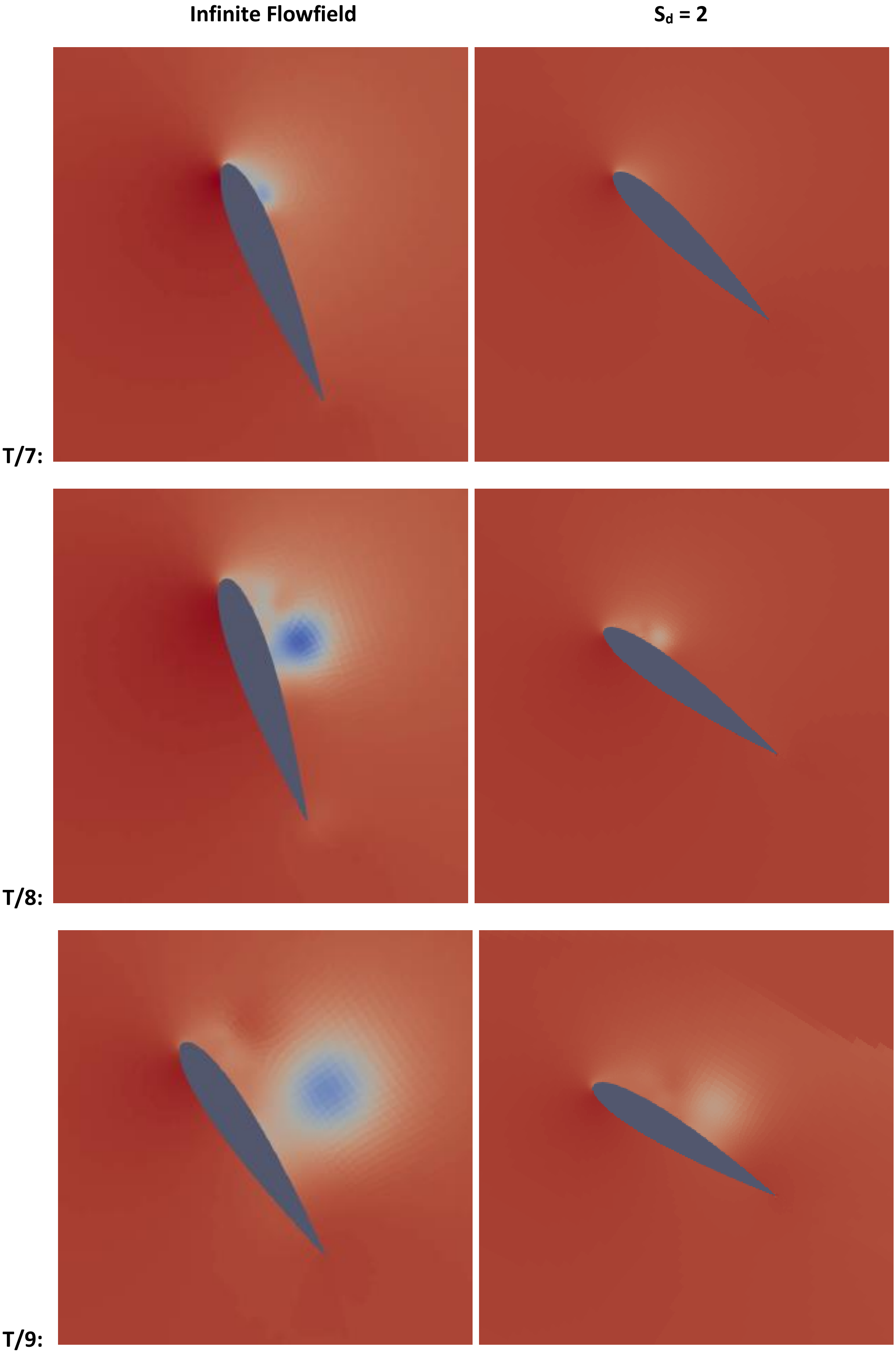
Infinite Flowfield
$S_d = 2$
T/7:
T/8:
T/9:

T/10:

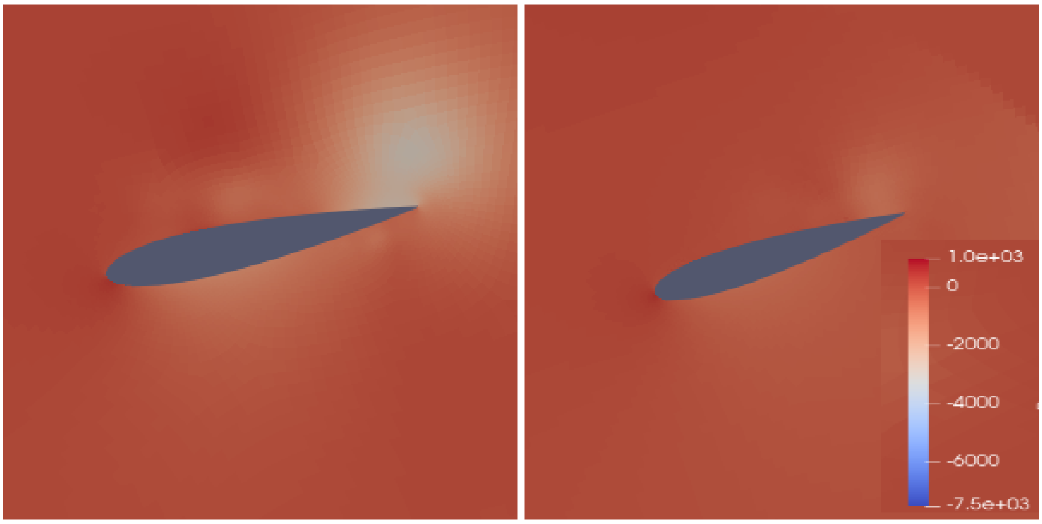

Figure 5.22 Pressure contours for the unbounded case(left), and the S_d = 2 case (right) showcasing the difference in pressure of the LEV between the two cases.

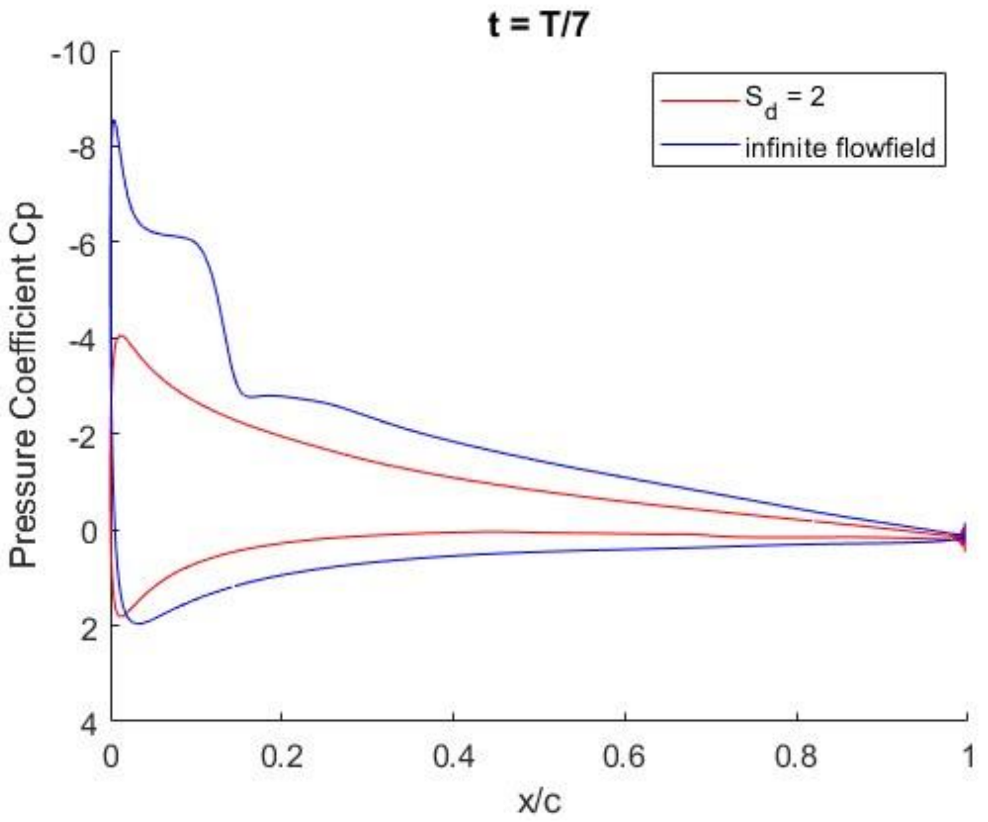

Figure 5.23 Pressure Coefficient (Cp) comparison between S_d = 2 case and Infinite case, showcasing dynamic stall.

6. Effect of Regular Waves

After examining the effects of a calm free surface on the performance of the foil, the next step should be to examine the influence of regular waves. As has already been stated, this device’s application will probably be in relatively shallow waters where the free surface might affect the performance. This free surface, however, is never completely calm, as waves formed in open seas will travel to the location of the device.

These waves are by nature irregular, meaning that waves of different amplitudes, phases and frequencies superimposed and form a final sea state. As a first step here, the effects of regular waves are studied to get a qualitative and quantitative sense for the influence of waves on the performance of the fully passive flapping foil device. In this section, regular waves are generated using CFD solver MaPFlow, which has already been tested for the accurate generation and propagation of regular waves, giving results very close to the experimental ones [32].

In this chapter, a parametric study is carried out to examine the effects of varying wave period and wavelength, on the fully passive foil. ω_e is defined as the encounter frequency between the waves and the foil. The current does not alter the encounter frequency, which remains the same with the frequency of the generated waves ω_w. The wavelength (λ) and wavenumber (k) however are altered because of the underlying current. As the waves propagate on a current, the wavelength is increased. To find the wavelength of the generated waves we need to solve (6.1) for the wavenumber k.

$$\omega_w = \sqrt{gk} \; + U_\infty k \tag{6.1}$$

The influence of waves on the foil is expected to be evident at low depth, as the pressure field they create is relatively small in strength, in comparison to the foil which experience dynamic stalling and consequently very high pressure drops. For this reason, cases for $S_d = 2c$ and $S_d = 3c$ were considered at first. However, the disturbance they cause to the calm free surface is very large, reaching up to 0.6c in amplitude, and thus the cycle-to-cycle variations on the motion and the loads caused by these waves will overshadow that of the incoming waves, making them non discernible. For this reason, the selected submergence depth selected was $S_d = 4c$, where disturbances reach amplitudes of up to 0.3c.

6.1 Waves with frequency equal to, and around the foil’s oscillating frequency.

The first step taken to study the effect of regular waves on the fully passive foil’s performance was to examine the effect of their frequency relative to the frequency of the foil under a calm free surface (ω_f). For the reasons outlined above, the tests were conducted at a submergence depth $S_d = 4c$. Reynolds number was kept the same: $6 \cdot 10^4$ and Fr = 1 was chosen. The device’s structural parameters and the mesh are also kept the same as in tests in chapter 5. The encounter frequency of the waves and the foil, relative to the foil’s frequency $\omega_f = 7.57$ r/s that were studied are:

$$\omega_e/\omega_f = 0.5,\ 0.8,\ 0.9,\ 1,\ 1.1,\ 1.2$$

The wave height H = 2a (a: amplitude) has to be comparable to the disturbance of the free surface caused by the foil. For this reason, it was chosen equal to 0.2c (a = 0.1c) for all cases, which requires the generation of nonlinear waves. The wavelength of the waves is a function of their frequency, according to the dispersion equation, but the underlying current increases this wavelength, by $k \cdot U_\infty$, where k is the wavenumber and U_∞ the current’s speed. Thus, λ is a dependent variable. The tank has a depth of 18c which is large relative to the wavelengths of the different cases. This means that wave propagation happens in deep water conditions. The corresponding wavelengths for each case are the following:

$$\lambda = 77.3c,\ 38.9c,\ 32.4c,\ 26.1c,\ 23.9c,\ 21.0c$$

How the performance is affected when the Submergence Depth of the foil is $S_d = 4$, and linear regular waves of height H = 0.2c are propagating along the free surface is evident in Figure 6.1, Figure 6.2 and Figure 6.3. Results for the main metrics are also gathered in Table 8.In Figure 6.1, it is seen that the presence of waves does not affect efficiency significantly, except for the case of ω_e/ω_f, = 1 where a slight increase of about 0.8% is witnessed. This indicates that resonance of the two motions increases power extraction. Furthermore, the average power coefficient is increased for all cases, by about the same amount, 4.5%. This translates to a power increase due to the presence of waves which is also clear if we consider two other metrics: first, as seen in Table 8, the average heaving motion amplitude, h*, is clearly increased. This is accompanied by a decrease in the period T* as seen in Figure 6.3 . Consequently, the hydrofoil’s average velocity is increased, and thus the numerator in $\overline{C_p}$’s definition is increased while the denominator remains the same. On the contrary, in η’s definition, while the numerator increases, the denominator is also increased as the larger heaving amplitude means that the area swept by the foil is wider. To sum up, waves with frequency close and around the oscillating frequency of the flapping foil result in a substantial increase of extracted , while efficiency does not is not altered, except for the case where the frequencies match. If the effect is beneficial is case dependent, as it depends whether the designer is optimizing for η or $\overline{C_p}$.

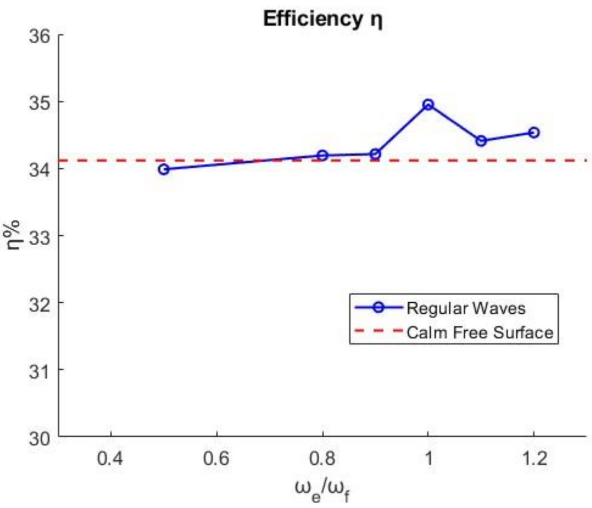

Figure 6.1 Efficiency η – Encounter Frequency/Wave frequency ω_e/ω_f

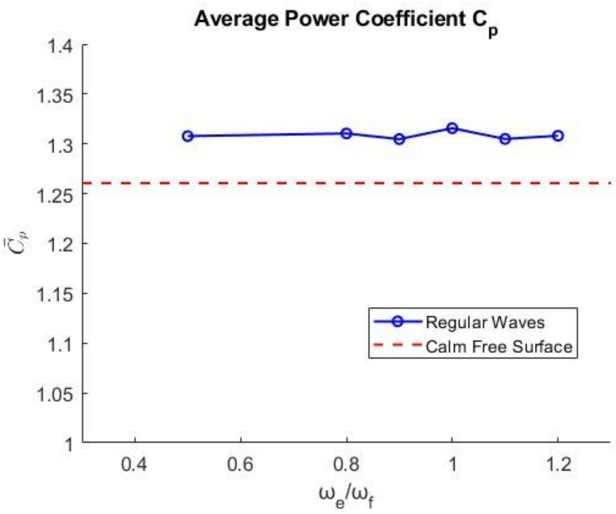

Figure 6.2 Average Power Coefficient C_p – Encounter Frequency/Wave frequency ω_e/ω_f

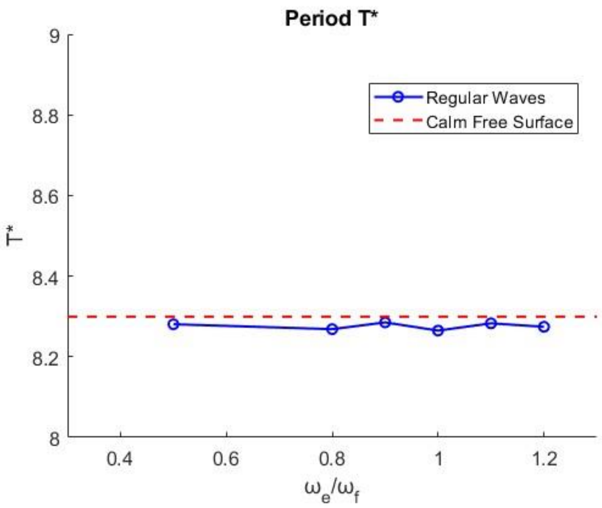

Figure 6.3 Period T – Encounter Frequency/Wave frequency ω_e/ω_f*

Table 8 Main Metrics Comparison between calm and wavey free surface

Case (ω_e/ω_f)	**h^***	**ϑ^***	**η [%]**	**T^***	**$\overline{Cp}$**
Calm	1.44	71.8	34.1	8.30	1.26
0.5	1.46	71.1	34.0	8.28	1.31
0.8	1.50	72.5	34.2	8.27	1.31
0.9	1.44	72.1	34.2	8.29	1.30
1.0	1.48	71.9	35.0	8.26	1.32
1.1	1.48	72.1	34.4	8.28	1.30
1.2	1.48	72.4	34.5	8.27	1.31

Figure 6.4 shows the heave timeseries for the different cases, where the peaks and crests are connected with a curve (envelope), in order to show the periodical variability of the heave amplitude, which differs for each case. This signifies that the relative position of the wave and the hydrofoil has an effect to the motion of the foil and subsequently to its performance, as increased heaving amplitude is tied with increased power extraction. The variability is especially visible in the $\omega_e/\omega_f = 0.5$ case where the wave frequency is half of the foil's frequency. The foil heaving motion is contrasted to the Free Surface Elevation above the foil (at its L.E.) in Figure 6.5. It is seen there that when a wave peak is present above the foil, heaving amplitude is increased, while when a crest is present, it is decreased. This effect is present in other cases also, for example in the $\omega_e/\omega_f = 0.8$ case, a periodical fluctuation of the heave amplitude is seen every 5 periods, as phase difference cycles every 5 periods also.

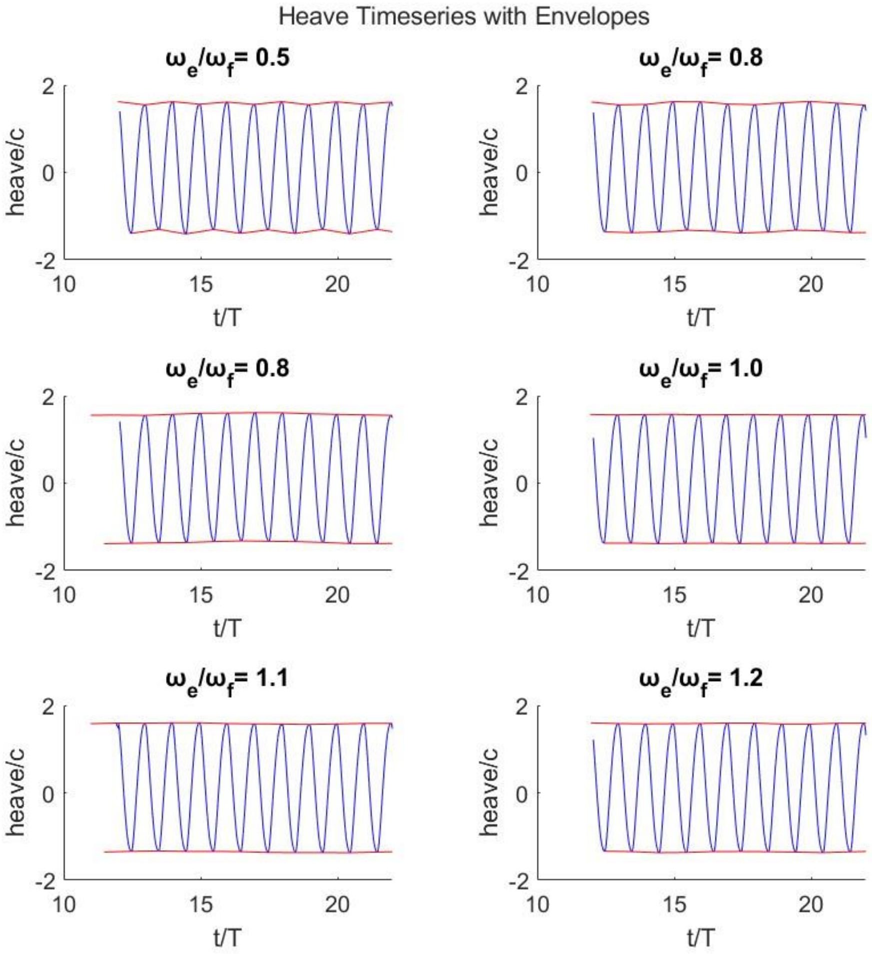

Figure 6.4 Heave timeseries for different cases where the envelopes show the periodical variability in heaving amplitude.

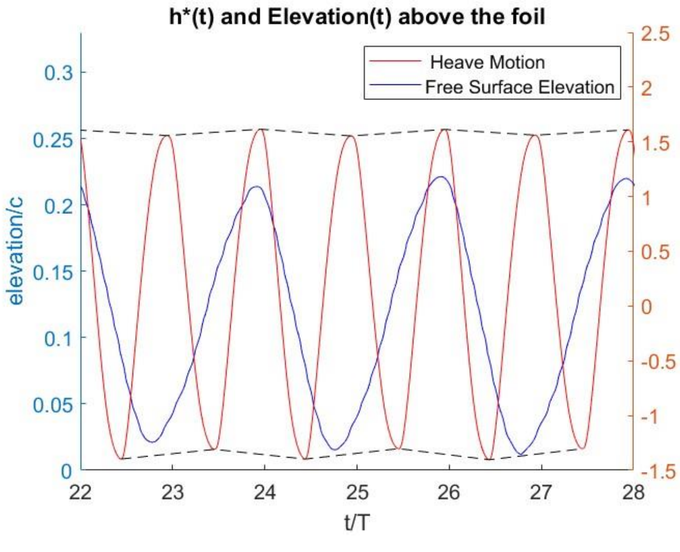

Figure 6.5 Free Surface Elevation above the foil (above the L.E. of the foil) compared to heave motion.

6.2 Varying phase difference with waves synchronized with the foil.

As noted in [36] large amounts of energy can be extracted from waves by a submerged semi-activated flapping foil when its frequency matches the wave's frequency or is double that, and the phase difference is optimal. However, the oscillation frequency and the phase of the fully passive flapping foil cannot be controlled. In section 5, it was stressed that the foil's frequency is very close to the device's heaving natural frequency. Unless this natural frequency can be changed, for example by varying the structural parameters of the device, there is no way the frequency can be controlled to match the encounter frequency of the waves. Neither can the phase difference.

In this section, the case of when the frequency of the foil's motion ω_f coincides with the encounter frequency of the waves, or $\omega_e/\omega_f = 1$, is expanded, as this is a special case because performance can be altered according to phase difference. For the other cases phase difference is not a factor as different phase differences are cycled through periodically, while when $\omega_e/\omega_f = 1$ the phase difference remains constant. For this case, however, phase difference might play a significant role. Except for the initial case (denoted as $\phi = 0$ in this section), two other cases with phase difference $\pi/2$ and π relative to that case are examined. The hydrofoil's and waves' frequency are $f^* = 0.76$.

For active flapping foils in waves, with $\omega_e/\omega_f = 1$, there exists a specific optimal phase difference that can be achieved as the motion can be enforced. Power extraction is maximum when the phase difference is such that the angle of attack is maximum [36]. However, for fully passive flapping foils this was not the case. As seen in Figure 6.6, efficiency is slightly increased for about 0.5% when phase difference is equal to zero, but generally, no significant performance increase was noticed with regards to phase difference. $\overline{C_p}$ is not affected significantly as seen in Figure 6.7.

The foil, however, is passive, meaning that the initially defined phase difference might not be held through the oscillations, as the relative position of the foil and the wave might converge to a final state. In Figure 6.8 it is shown that this is indeed the case, for the case of $\phi = 0$. The heave motion and the surface elevation right above the foil are contrasted for an early time at period N = 5 and a later time at N = 23. It is seen in this figure that the foil's motion is slowly altered in order to match the phase of the incoming waves. Although the foil does synchronize with the waves, no significant increase in performance (η or $\overline{C_p}$) was noticed, through the periods, as the phase difference approaches its final value. This is depicted in Figure 6.9. For the other two cases this effect does also occur, but no final state was reached for the number of periods simulated, as convergence was slower.

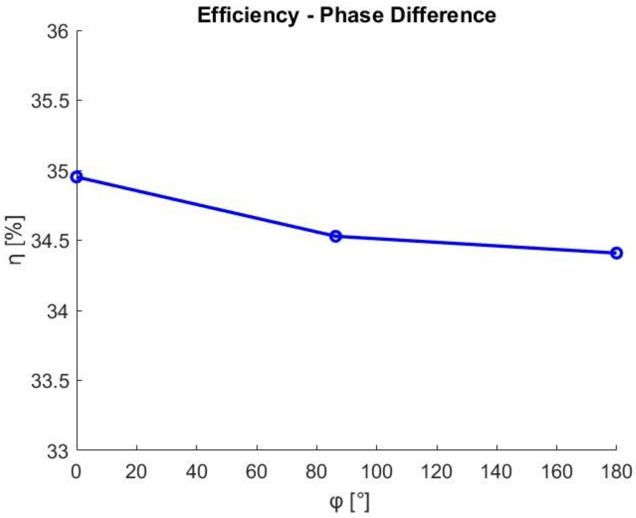

Figure 6.6 Impact of wave phase on efficiency when $\omega_e/\omega_f = 1$.

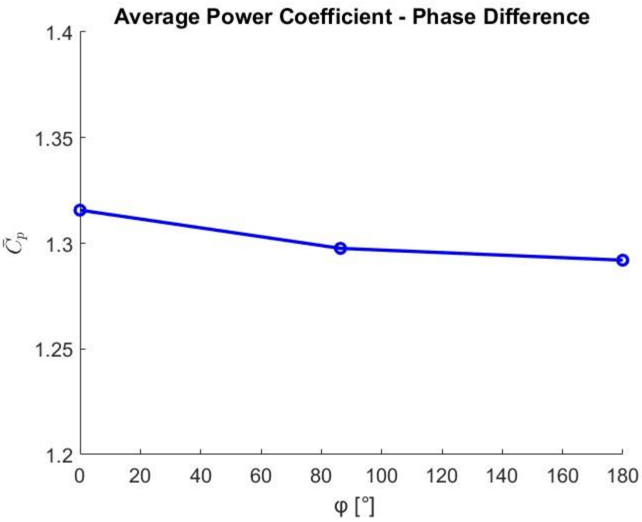

Figure 6.7 Impact of wave phase on Average Power Coefficient $\overline{C_p}$ when $\omega_e/\omega_f = 1$.

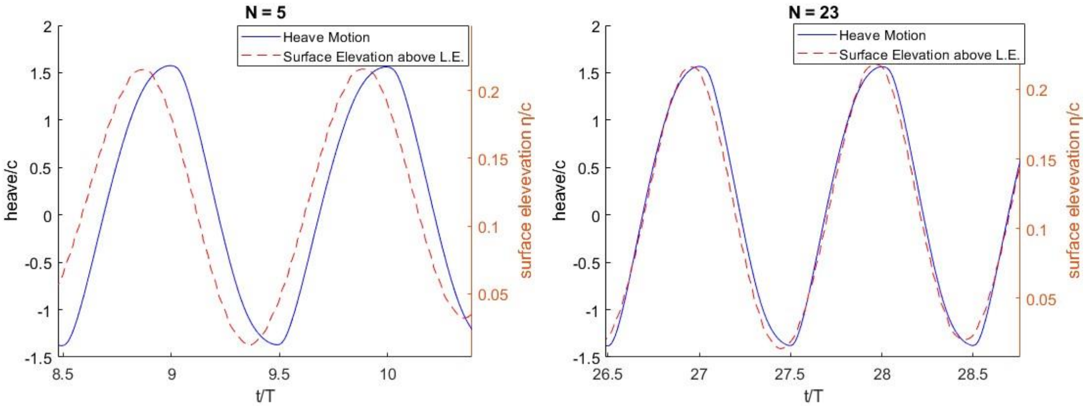

Figure 6.8 Wave Elevation compared to Heave motion for periods N = 5 and N = 23. The phase sift between them is seen.

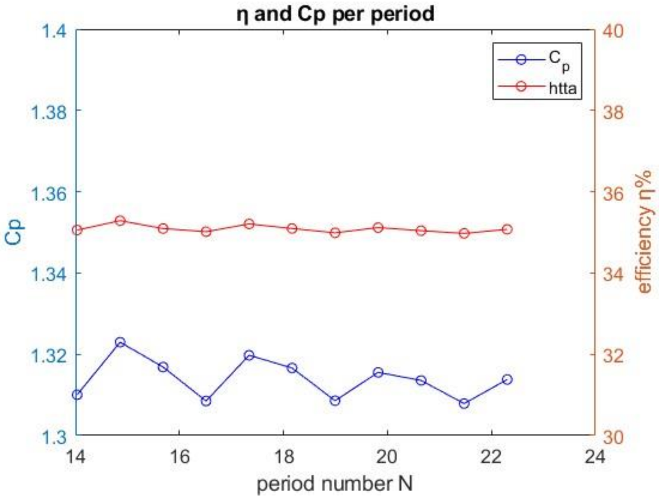

Figure 6.9 Average Power Coefficient C_p and efficiency η trough the periods for φ = 0

6.3 Waves with wavelength comparable to the hydrofoil's chord length.

In this section, high frequency-small wavelength waves are created on the Free Surface above the fully passive flapping foil, submerged, again, in depth $S_d = 4c$. As for wave frequencies close to that of the flapping foil, examined in section 6.2, corresponding wavelengths are large, 20 times the chord length of the foil or greater. Two cases of waves with wavelength comparable to the chord length of the foil are tested here. The wavelengths of the two cases and their corresponding frequencies are:

$$\lambda = 3c \text{ and } 5c$$

with $f^* = 0.56$ and 0.38 accordingly, or $\omega_e/\omega_f = 0.21$ and 0.32,

where $f^* = \frac{f \cdot c}{U_\infty}$.

Results are presented in Figure 6.10 and Figure 6.11 with red markings. The blue markings correspond to the cases examined in section 6.1 and are added for comparison. First a slight decrease in efficiency of about 0.6% is evident for small wavelengths, while the gain in Power Coefficient $\overline{C_p}$ is lost and power extraction is the same as in the calm free surface case. This loss in power extraction is evident as the motion's period is increased, as seen in Table 9 and Figure 6.12, while its amplitude remains the same, resulting in decreased foil velocities. Finally, in contrast to section 6.1, no significant variability in heave motion amplitude is noticed with high frequency waves, as seen in Figure 6.13.

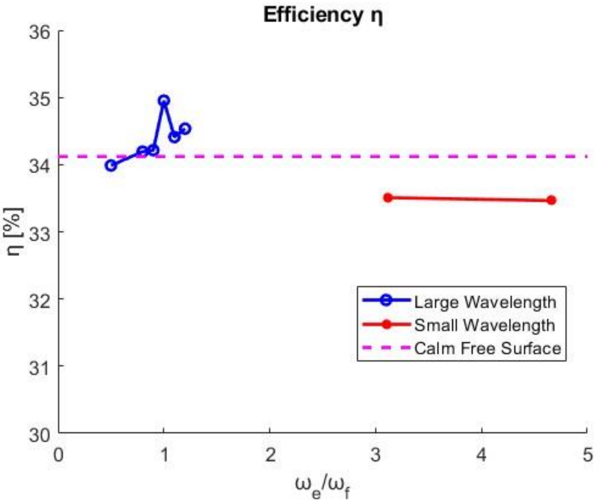

Figure 6.10 Efficiency comparison for small wavelength (high frequency) waves.

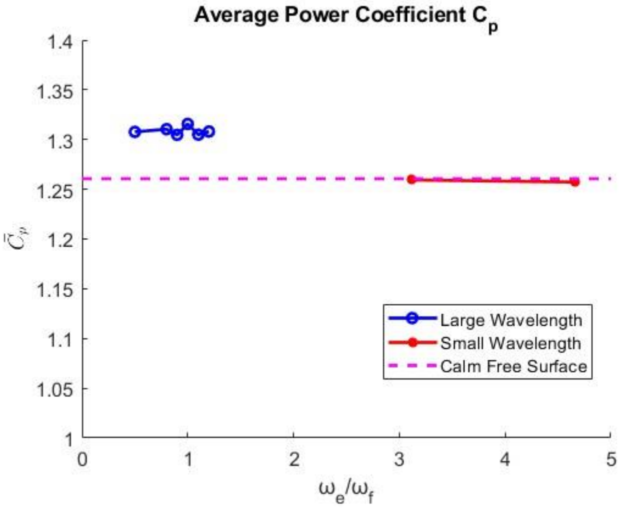

Figure 6.11 Average Power Coefficient comparison for small wavelength (high frequency) waves.

Table 9 Main Metrics for the case of small wavelength λ in comparison to the case $\omega_e/\omega_f = 1$.

$\omega_\varepsilon/\omega_f$	h*	θ*	η	T*	$\overline{C_p}$
0.18	1.47	70.2	33.5	8.45	1.26
0.27	1.48	70.4	33.5	8.46	1.26
1.00	1.48	71.9	35.0	8.26	1.32

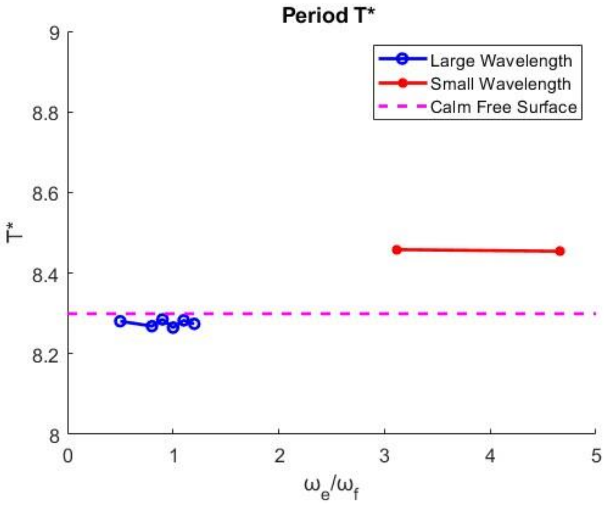

Figure 6.12 Motion Period T for small wavelength relative to large wavelengths.*

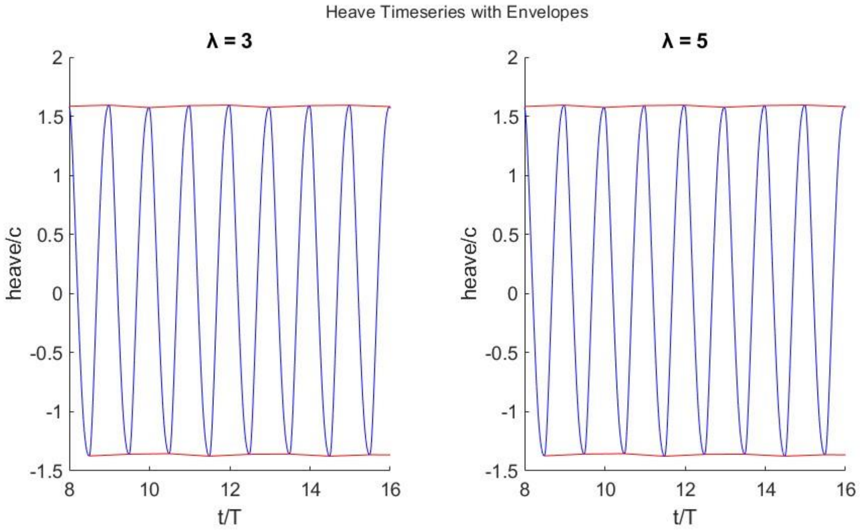

Figure 6.13 Envelopes on the heave motion showing the variability in amplitude.

Conclusions and Recommendations for future research.

The purpose of this thesis was to examine whether the fully passive flapping foil device, which presents a viable option as a tidal energy or river energy harvesting device, in more realistic conditions with the addition of the free surface. The parametric analysis was conducted for a selected set of parameters, that were held constant for all cases, which were locally optimized by [31], by varying the rotational spring and rotational dumper coefficients. As the motion of the foil is dependent on the flowfield and vice versa, the fluid problem and the dynamics problem were solved sequentially for each timestep. This required the strong (in order to avoid the added mass instability problem) coupling of the in-house CFD solver MaPFlow, with the Rigid Body Dynamics solver. The movement of the mesh around the body was implemented with the Radial Basis Functions method. The numerical setup was, first, evaluated against experimental results, in an infinite flowfield, where the error in the prediction of the performance was very small.

The influence of the calm free surface was investigated first, for various Submergence Depths and Froude numbers. It is important to state first that, especially for the particular structural parameters, the pitching motion of the device is mainly determined by a large Leading-Edge vortex that is formed as the foil undergoes Deep Dynamic Stall. This vortex, however, did not have sufficient strength for low water currents and thus the motion of the foil was impaired. For this reason, Fr numbers above 0.8 were studied. The Froude number mainly influences the ability to disturb the free surface, as for low Fr number, the free surface is disturbed less, and vice versa. The general trends for the various Fr numbers, however, were the same and no trend was found, so emphasis was given for the representative case of Fr = 1 and many Submergence Depths were explored for this.

As for the various Submergence Depths (S_d), a vast parametric space was explored, beginning with S_d = 2 chord lengths (c), which was limiting because the amplitude of the motion was 1.5c, up to S_d = 9c where performance was very close to the infinite flowfield case. For very low S_d, below 3c, performance drops rapidly as great amounts of energy from the foil are imparted to the free surface, for the generation of waves, and the synchronization of the pitching and heaving motion is negatively affected. Increasing the S_d however a bit further performance peaks and is even higher than that of the infinite flowfield case. This optimal performance S_d is created due to the constriction between the foil and the free surface, which partly acts as a rigid body. The Bernoulli effect, consequently, makes pressure drop and lift on the foil to increase. Further increase in S_d reduces performance, slightly below the infinite case and then the infinite case is approached for even higher S_ds. Thus, this optimal S_d is recommended for applications, and low S_ds, below 3c, are to be avoided.

The effect of regular waves that was examined in chapter 6 was deemed positive for power extraction ($\overline{C_p}$) when their frequency is close to that of the flapping foil while efficiency remains unchanged. For short wavelength – high frequency waves however efficiency tends to drop below the calm free surface case and power extraction remains unchanged.

Future research on fully passive energy harvesting flapping foils should focus on more realistic conditions for nearshore deployment of the device, like the combination of shear with the free surface, variable bathymetry, and the effect of vorticity on the incoming flow. The effect of waves when the foil is closer to the free surface should also be studied. It has also been shown that the three-dimensional effects cannot be ignored as performance drops rapidly for small span wings, due to high tip loses. On the other hand, latest research by [37] has discovered structural parameters for the device that offer a much higher performance than the ones studied here, (some parameters offer efficiency up to 53.8%, and others Power Coefficient $\overline{C_p}$ up to 1.9) and shown that for optimal performance the hydrofoil does not undergo deep Dynamic Stall, while the pitching motion happens through power transfer from the heaving to the pitching motion. This proves that the fully passive flapping foil device can have performance that is comparable to active foils while it remains mechanically much simpler and cost effective. The author recommends that future research should expand upon this breakthrough, examining it under more realistic conditions.

Bibliography

[1] Y. Dai, Z. Ren, K. Wang , W. Li, Z. Li and W. Yan, "Optimal sizing and arrangement," *IEEE Trans. Sustain. Energy,* vol. 9, pp. 168-177, 2018.

[2] J. Domenech, T. Eveleigh and B. Tanju, "Marine Hydrokinetic (MHK) systems: using systems thinking in resource characterization and estimating costs for the practical harvest of electricity from tidal currents,," *Renew. Sustain. Energy,* vol. 81, p. 723e730, 2018.

[3] M. Nachtane, M. Tarfaoui, I. Goda and M. Rouway, "A review on the technologies, design considerations and numerical models of tidal current turbines," *Renewable Energy,* 2020.

[4] J. Kiefer, C. E. Brunner, M. Hultmark and M. O. L. Hansen, "Dynamic Stall at high Reynolds number due to variant types of airfoil motion," *Journal of Physics: Conference series,* 2020.

[5] J. Young, C. J. Lai and M. F. Platzer, "A review of progress and challenges in flapping foil power generation," *Progress in Aerospace Sciences,* 2014.

[6] D. M. Lane, M. Sfakiotakis and B. C. Davies, "Review of Fish Swimming Modes for Aquatic Locomotion," *IEEE Journal of Oceanic Engineering,* 1998.

[7] L. Schouveiler, F. Hover and M. Triantafyllou, "Performance of flapping foil propulsion," *Journal of Fluids and Structures,* vol. 20, 2005.

[8] A. Andersen, T. Bohr, T. Schnipper and J. H. Walther, "Wake structure and thrust generation of a flapping foil in two-dimensional flow," *Journal of Fluid Mechanics,* 2016.

[9] W. McKinney and J. DeLaurier, "The Wingmill: An Oscillating-Wing Windmill," *AIAA,* vol. 5, 1984.

[10] Q. Zhu, M. Haase and C. H. Wu, "Modeling the capacity of a novel flow-energy harvester," *Applied Mathematical Modelling,* 2009.

[11] Z. Peng and Q. Zhu, "Energy harvesting through flow-induced oscillations of a foil," *PHYSICS OF FLUIDS,* vol. 21, 2009.

[12] M. Boudreau, M. Picard-Deland and G. Dumas, "A parametric study and optimization of the fully-passive flapping-foil," *Renewable Energy,* 2019.

[13] J. Deng, S. Wang, P. Kandel and L. Teng, "Effects of free surface on a flapping-foil based ocean current energy," *Renewable Energy,* vol. 181, 2021.

[14] B. Zhu, W. Cheng and J. Geng, "Energy-harvesting characteristics of flapping wings with the free-surface effect," *Journal of Renewable and Sustainable Energy,* vol. 14, 2022.

[15] K. Theodorakis, D. Ntouras and G. Papadakis, "Investigation of a submerged fully passive energy-extracting flapping foil operating in sheared inflow," *Journal of Fluids and Structures,* vol. 113, 2022.

[16] H. Isshiki, "A Theyory of Wave Devouring Propulsion," *Journal of the Society of Naval Architects of Japan,* pp. 54-64, 1982.

[17] L. Peng, L. Yebao, H. Shuling, Z. Jianfeng and S. Yumin, "Effects of Regular Waves on Propulsion Performance of Flexible Flapping Foil," *Journal of Applied Sciences,* 2018.

[18] G. D. Xu, W. Y. Duan and B. Z. Zhou, "Propulsion of an active flapping foil in heading waves of deep water," *Engineering Analysis with Boundary Elements,* 2017.

[19] E. S. Filippas, T. P. Gerostathis and K. A. Belibassakis, "Semi-activated oscillating hydrofoil as a nearshore biomimetic energy system in waves and currents," *Ocean Engineering ,* 2018.

[20] R. F. Kunz, "A preconditioned Navier-Stokes method for two-phase flows with application to cavitation prediction," *Computers and Fluids,* 2000.

[21] P. L. Roe, "Approximate Riemann solvers, parameter vectors, and difference schemes," *Journal of Computational Physics,* pp. 357-372, 1981.

[22] P. Quentey and M. Visonneau, "An interface capturing method for free-surface hydrodynamic flows," *Computers and Fluids,* pp. 1481 - 1510, 2007.

[23] B. P. Leonard, "Simple high-accuracy resolution program for convective modelling of discontinuities," *International Journal for Numerical Methods in Fluids,* pp. 1291-1318, 1998.

[24] O. Ubbink, "Numerical Prediction of Two Fluid Systems With Sharp Interfaces," *Journal of Computational Physics,* pp. 277-298, 1987.

[25] S. Muzaferija and M. Peric, "Computation of free-surface flows using interface-tracking and interface-capturing methods in Nonlinear Water Waves Interaction," *WIT Press: Southampton, UK,* pp. 59-100, 1999.

[26] J. Wackers, "Free-Surface Viscous Flow solution Methods for Ship Hydrodynamics," *Archives of Computational Methods in Engineering,* pp. 1-41, 2011.

[27] M. Darwish and F. Moulkaled, "Convective Schemes for Capturing Interfaces of Free-Surface Flows on Unstructured Grids.," *Numerical Heat Transfer,* pp. 19-42, 2006.

[28] B. e. a. Devolder, "Application of boyancy-modified k-omega SST turbulence model to simulate wave run-up around a monopile subjected to regular waves using OpenFoam," *Coastal Engineering,* pp. 81-94, 2017.

[29] P. Causin, J. Gerbeau and F. Nobile, "Added-mass effect in the design of partitioned algorithms for fluid–structure problems," *Computer Methods in Applied Mechanics and Engineering,* vol. 194, no. 42-44, 2005.

[30] J. Deng, C. P. Caulfield and X. Shao, "Effect of aspect ratio on the energy extraction efficiency of three-dimensional flapping foils," *Physics of Fluids,* 2014.

[31] L. Duarte, N. Dellinger, G. Dellinger, A. Ghenaim and A. Terfous, "Experimental optimization of the pitching structural parameters of a fully passive flapping foil turbine," *Renewable Energy,* vol. 171, pp. 1436-1444, 2021.

[32] D. Ntouras and G. Papadakis, "A Coupled Artificial Compressibility Method for Free Surface Flows," *Journal of Marine Science and Engineering,* 2020.

[33] J. M. Birch, W. B. Dickson and M. H. Dickinson, "Force production and flow structure of the leading edge vortex on flapping wings at high Reynolds numbers," *The Journal of Experimental Biology,* vol. 207, 2003.

[34] P. REICHL, K. HOURIGAN and M. C. THOMPSON, "Flow past a cylinder close to a free surface," *Journal of Fluid Mechanics,* vol. 533, pp. 269-296, 2005.

[35] R. B. Green and J. H. Gerrard, "Vorticity measurements in the near wake of a circular cylinder at low Reynolds number," *Journal of Fluid Mechanics,* vol. 246, pp. 675-691, 1993.

[36] E. S. Filippas, T. P. Gerostathis and K. A. Belibassakis, "Semi-activated oscillating hydrofoil as a nearshore biomimetic energy system in waves and currents," *Ocean Engineering,* 2018.

[37] M. Boudreau, M. Picard-Deland and G. Dumas, "A parametric study and optimization of the fully-passive flapping-foil turbine at high Reynolds number.," *Renewable Energy,* 2020.

[38] M. M. Macias, I. F. Souza, A. C. Brasil Junior and T. F. Oliveira, "Three-dimensional viscous wake flow in fish swimming - A CFD study," *Mechanics Research Communications,* 2020.